Final Technical Report (FTR)

Cover Page

a. *Federal Agency*	Department of Energy
b. *Award Number*	DE-EE0009378
c. *Project Title*	Innovative Method for Welding in Generation 3 CSP to Enable Reliable Manufacturing of Solar Receivers to withstand Daily Cycling at Temperatures Above 700°C
d. *Recipient Organization*	Electric Power Research Institute
e. *Project Period*	*Start*: 03/01/2021 *End*: 08/31/2022
f. *Principal Investigator (PI)*	John Shingledecker Principal Technical Executive jshingledecker@epri.com 704-595-2619
g. *Business Contact (BC)*	Cindy Colwell Government Contract Administrator ccolwell@epri.com 865-218-8109
h. *Certifying Official (if different from the PI or BC)*	

11/21/2022

Signature of Certifying Official *Date*

By signing this report, I certify to the best of my knowledge and belief that the report is true, complete, and accurate. I am aware that any false, fictitious, or fraudulent information, misrepresentations, half-truths, or the omission of any material fact, may subject me to criminal, civil or administrative penalties for fraud, false statements, false claims or otherwise. (U.S. Code Title 18, Section 1001, Section 287 and Title 31, Sections 3729-3730). I further understand and agree that the information contained in this report are material to Federal agency's funding decisions and I have any ongoing responsibility to promptly update the report within the time frames stated in the terms and conditions of the above referenced Award, to ensure that my responses remain accurate and complete.

Acknowledgement: "This material is based upon work supported by the U.S. Department of Energy's Office of Energy Efficiency and Renewable Energy (EERE) under the DE-FOA-0002243 [Solar Energy Technologies Office Fiscal Year 2020 Funding Program, Small Innovative Projects in Solar (SIPS)] Award Number: DE-EE0009378.

Executive Summary:

Inconel® Alloy 740H® (alloy 740H) was the first age-hardenable nickel-based alloy approved by the ASME Boiler & Pressure Vessel Code for use in pressure-boundary applications. Over the past ~20 years the alloy has been optimized for weldability and high-temperature stability, approved for use in different applications. Development of a supply chain combined with the advantageous properties of the alloy (high-temperature creep strength, oxidation and corrosion resistance, etc.) have resulted in the alloy being applied to new high-temperature power cycle demonstration projects, and of particular interest are applications to concentrating solar power (CSP) to enable higher-efficiency Generation 3 CSP systems and the corresponding supercritical CO_2 (sCO_2) power cycle components (heat exchangers, piping, etc.). The high allowable stresses of alloy 740H also make it a desirable material for current Generation 2 CSP solar power receivers to improve cyclic capability and/or reduce receiver height.

Recent experiences in demonstration projects utilizing alloy 740H identified cracking issues during welding and fabrication. In this project, a detailed study was done to confirm and clarify the Stress Relaxation Cracking (SRxC) mechanism, also known as stress relief cracking or strain-age cracking (SAC), during post-weld heat-treatment (PWHT). This involved detailed microscopy and advanced characterization to understand the root cause(s) of three failures obtained from industry. Based in-part on these findings, a targeted laboratory based SRxC test method was utilized to evaluate variables such as heat-to-heat variations, strain level, PWHT temperature, and starting material condition on three heats of alloy 740H. Industrial shop welding of cold-worked plates was also conducted. The research showed the following:

- SRxC was confirmed as the cracking mechanism for all field failures
- Stress state (from residual stresses, constraint, deformation, and local stress concentrations) was playing a significant role in field failures and laboratory testing confirmed increasing susceptibility for all heats with increasing strain levels. High levels of microstructural strain were identified at crack initiation locations, in some cases leading to local recrystallization.
- Precipitate free zones (PFZs) at grain boundaries were found at relaxation cracks and crack initiation locations uniquely associated with SRxC in alloy 740H. Laboratory testing reproduced this microstructural feature which had only previously been reported in long-term creep testing of weldments. Advanced nano-scale characterization confirmed the presence of a moving boundary leading to coarsening of precipitates and PFZs where damage accumulated.
- The research suggested heat-to-heat variations due to local chemistry and processing may influence SRxC susceptibility, but more work is needed to fully clarify these effects.

To disseminate the key learnings from this research to the scientific and engineering communities and alloy 740H end users, multiple technical publications and presentations were made, an industrial alloy 740H users meeting was held, and a new industry guideline specification document which can be directly implemented by end-users of alloy 740H was produced.

Table of Contents:

1. Background:

Inconel® Alloy 740H® (UNS N07740), here-in referred to as alloy 740H (nominal composition in Table 1), was the first age-hardenable nickel-based alloy approved by the ASME Boiler & Pressure Vessel Code for use in pressure-boundary applications. It was originally developed as a coal-fired boiler tubing alloy for advanced ultrasupercritical (A-USC) steam applications. Over the past ~20 years the alloy has been optimized for weldability and high-temperature stability, approved for use in different applications, and the number of product forms and manufacturing processes demonstrated now includes all the required product forms needed for a variety of high-temperature applications including thin-wall tubing, heavy wall piping, cold-formed and induction bends, seam welded piping, fittings, forging, sheet, etc. [1].

Table 1. Alloy 740H Nominal Composition (wt%)

C	Ni	Fe	Cr	Mn	Si	Mo	Co	Al	Ti	B	Nb+Ta
0.06	Bal.	0.7	24.5	0.3	0.15	0.1	20	1.35	1.35	0.001	1.5

The development of a supply chain combined with the advantageous properties of the alloy (high-temperature creep strength, oxidation and corrosion resistance, etc.) have resulted in the alloy being applied to new high-temperature power cycle demonstration projects as shown in Table 2. Of particular interest to the concentrating solar power (CSP) community have been the recent development of lower cost alloy 740H product forms to enable Generation 3 CSP systems and the corresponding supercritical CO_2 (sCO_2) power cycle (heat exchangers, piping, etc.) [2,3]. The high allowable stresses of alloy 740H also make it a desirable material for current Generation 2 CSP solar power receivers to improve cyclic capability and/or reduce receiver height [4, 5].

Nickel-based alloys may be susceptible to a number of weldability challenges [6,7]. A 2018 review of the weldability and performance of high-strength nickel-based alloys to enable advanced power systems proposed that alloy 740H was generally not susceptible to fusion zone solidification cracking, had minimal risk of liquation cracking if proper alloy chemistry control and welding practices were used, but the risk for stress relaxation cracking (SRxC) during post-weld heat-treatment (PWHT) or high-temperature service also known as strain age cracking (SAC) was a potential concern which required further evaluation [8]. The complexities of the SRxC damage mechanism require a specific combination of a susceptible microstructure, the presence of a stress (typically a residual stress from welding), and high-temperature exposure in a specific temperature range and time to cause relaxation of the imposed stress by cracking. The result is SRxC is highly component design, fabrication practice, and application specific [9]. In 2018 when the review was written, SRxC had not been observed in 740H, but at that time, most of the practical welding experience on the alloy was restricted to laboratory studies, industrial qualification activities, and relatively limited demonstrations conducting 10's of welds. Today, the applications listing in Table 2 alone represent tons of 740H products including kms of tubing and piping which have now been produced and welded as part of several completed and ongoing large-scale demonstrations. It is documented that 1000's of welds have now been successfully executed in shop and field fabrication for alloy 740H.

Table 2. Demonstrations Utilizing 740H

Years	Name	Description	Product forms	Application Notes
2011-15	Plant Barry Steam Loop	760°C+ Steam +2yr operation	Tubing (~50mm diameter)	First 'live-fire' A-USC demo.
2014-16	Sunshot Turbine Test	700°C+ microtube HX and connecting piping	Small dia. Tubing, piping	First sCO2 heat-exchanger [Funded EERE-SETO]
2017-current	NET Power Demonstration	700°C direct-fired sCO_2 test facility	Piping	First commercial-scale piping installation
2018-current	STEP Heater	50 MWth natural gas fired sCO_2 heater	Tubing, piping, forgings	~25,000kg overall ~6,100m of tubing
	STEP Piping	715°C, 250bar sCO_2 piping system	Heavy wall piping (200-250mm dia.), bends & elbows	~150m piping 26 bends/elbows

The overall experience with welding alloy 740H, when properly executed, is very good, but it requires careful attention to all details in the welding process, as weld process and qualification development, welder training, and oversight is critical to success [10]. At the inception of this 18 month project (circa 2020), a recent review of field and shop experience with alloy 740H experience (in addition to a review of some of the key factors for in-service cracking of 347H stainless steel and other nickel-based alloys including alloy 617) had identified a few instances of cracking during the post-weld heat-treatment (PWHT) cycle of 740H [11]. Further investigations confirmed SRxC as the operative mechanism in ~3% of tubing welds in the STEP sCO_2 fired heater coil [12]. Based on the industry experience and the growing use of alloy 740H in the engineering community and in particular the CSP developers, designers, and fabricators exploring the use of alloy 740H for Generation 2 and 3 designs (solar receivers, sCO2 heat exchangers, sCO2 power cycle components), there is a need to provide improved guidance beyond the current codes & standards and general nickel alloy weldability literature specifically for alloy 740H to reduce the propensity for SRxC damage.

2. Project Objectives:

This project seeks to rapidly develop an innovative and agile approach to improved material, welding, and design specification guidance for Inconel® Alloy 740H® (alloy 740H) to avoid Stress Relaxation Cracking (SRxC), also known as stress relief cracking or strain-age cracking (SAC) during post-weld heat-treatment (PWHT), in Generation 3 (Gen 3) Concentrated Solar Power (CSP) receivers and other pressure retaining components of use in advanced thermal power cycles such as piping. The project objectives are to understand the root cause(s) of cracking based on recent industrial experience, develop a laboratory test method to identify the variables which are leading to SRxC, and utilize the combination of experience and laboratory work to provide improved welding and fabrication guidance. The end goal of the project is to disseminate this information to the scientific and engineering communities through technical publications and presentations and produce a new industry specification which can be directly implemented by end-users of alloy 740H.

The impact of this guideline, which incorporates the lessons learned from multiple projects across DOE and Industry, is aimed to help build end-user confidence for applications with these nickel-based alloys and ultimately allow for larger scale demonstrations and commercial systems to be reliably constructed and operated.

The project workplan was constructed with the following technical approach. The project will first perform a detailed root cause analysis (RCA) failure investigation of multiple cracked tubes from a recent fired-heater project and samples collected from other industry experience to determine if SRxC is the operative mechanism. The RCA will include metallurgical failure investigations and take advantage of macro to micro to nano materials characterization. Additionally, fabrication and welding records will be reviewed and analyzed including review with team member and external experts. Using this information, past research, and literature, experiments will be designed using a thermo-mechanical simulator (Gleeble™) supported by advanced electron microscopy to re-create the field cracking in the laboratory. The combination of field observations and the experimental methods will then be applied to evaluate the key variables determined to be affecting cracking as well as the many instances where SRxC has not occurred in different welding geometries and methods. With the key variables identified, improved welding process controls will be specified and tested to demonstrate the applicability of the new guidance. With this 'partial validation', all the information will be summarized and developed into a new industry specification for welding of 740H.

The collaborative team involved in this effort is made up of EPRI (Task 1), JND Metallurgical Consulting at Lehigh University (Task 2), and Special Metals Corp. (Task 3) and organized into the following tasks and subtasks:

Task 1.0: *Project Management, Failure Analysis, Industry Interaction, and Specification Development*

Subtask 1.1: *Project Management and Integration*

Subtask 1.2: *Initial failure analysis and materials characterization*

Subtask 1.3: *Characterization of laboratory heat and tested welds*

- ***Subtask 1.4:*** *Specification writing, data integration, and tech-to-market engagement*

- ***Task 2.0:*** *Laboratory Stress Relaxation Testing and Advanced Characterization*
  - ***Subtask 2.1:*** *Advanced Microscopy of Failures*
  - ***Subtask 2.2:*** *SRxC Testing and Analysis*
- ***Task 3.0:*** *Industrial guidance and implementation*
  - ***Subtask 3.1:*** *Supply of failures, industry experience, and technical guidance*
  - ***Subtask 3.2:*** *Supply of additional materials and weldments for study*
  - ***Subtask 3.3:*** *Welding guideline testing*

In this 18 month rapid effort, the milestones were as follows:

- ***Milestone 1:*** *Root cause analysis (RCA) of field cracking in 740H*
- ***Milestone 2:*** *Successful demonstration of a SRxC laboratory test method*
- ***Milestone 3:*** *Tech-to-market: draft journal or conference proceedings paper*
- ***Milestone 4:*** *Welding guideline testing and evaluation*
- ***EOP-A:*** *Final specification document*
- ***EOP-B:*** *Tech-to-market: peer reviewed paper and industry presentation*

3. Project Results and Discussion

3.1 Task 1: Project Management, Failure Analysis, Industry Interaction, and Specification Development

For the successful completion of Milestone 1, *Root cause analysis (RCA) of field cracking in 740H*, the team collected samples from industry and conducted detailed failure investigations from three relevant failures. Using the knowledge gained from these failures and a review of literature and prior research on alloy 740H, an expert group was convened to rank the various factors influencing the cracking as a means to focus the laboratory testing in Task 2. Additional advanced characterization activities to clarify mechanisms were also conducted.

To meet and exceed the objectives of Milestone 3 and EOP-B, *Tech-to-market*, the project team completed the following (the actual references can be found in Section 6 (Products)):

- Participation and formal presentation to a DOE sCO_2 cross-cutting team (FE, NE, EERE) on the energy industry experience with relaxation cracking phenomenon in the fabrication and operation of power plants
- A ½ day 740H user group meeting to share fabrication and welding experiences in the application of 740H with a focused group of users, fabricators, welding experts, manufacturers, and select research organizations involved with demonstration projects.
- Two presentations to disseminate the project results at the American Welding Society (AWS) International Conference on Advanced in Welding and Additive Manufacturing Research (AWAMR).
- A reviewed and accepted for publication conference proceeding paper on the industry experience and summarizing the project results for the Superalloys 718 and Derivatives 2023 Conference (to be held in Pittsburgh, PA in May of 2023).

The EOP-A deliverable was an industry first-of-a-kind specification guidance document for the procurement and fabrication of alloy 740H. The document has been drafted and is going through the EPRI publication process with delivery to the public by 12/31/22 as EPRI Report 3002025494 (Technical Requirements of Procurement of Components Fabricated from INCONEL ® Alloy 740H ®).

The following sections provide the details of the characterization of stress relaxation cracking (SRxC) failures in 740H weld fabrications (3.1.1) and a summary of the technology-to-market activities (3.1.2).

3.1.1: Characterization of Stress Relaxation Cracking Failures in 740H Weld Fabrications

Introduction

Inconel® 740H® (740H) alloy (UNS N07740) is widely being considered as the material of choice for the high temperature and pressure retaining sections of new and emerging power generation technology such as Generation 3 Concentrated Solar Power (CSP) receivers and systems with advanced thermal power cycles. Recent experiences in multiple technology demonstration projects, however, have brought forward an issue that is observed on occasion during the fabrication of 740H components. That is, some shop welds on 740H components have reportedly exhibited stress relaxation cracking (SRxC) after the weld fabrication stages. Although the phenomenon of stress relaxation cracking (SRxC) (also known as stress relief cracking or strain age cracking) has been well documented in austenitic stainless steel and some nickel-based alloys, observations highlighting its manifestation in alloy 740H is a relatively recent occurrence. To determine the underlying cause for such failures in this alloy, in-depth failure investigations of failed components is necessary. In Task 1 of this project, multiple examples of failures observed at the welds during the fabrication of various 740H components were collated, documented, and characterized. In this investigation, metallographic examinations were performed to study the characteristics of the microstructure at the SRxC locations in these failures. Details of these investigations are provided below.

Description of collected components with SRxC

SRxC failures observed during the fabrication stages of three separate demonstration projects were collected for the investigative parts of this project. These gathered set of samples were some of the most diverse component sizes and joint geometries, and largely represent the body of applications where alloy 740H is being employed in pressure retaining parts of advanced thermal power systems. Table 3 provides an overview of the components collected from the three demonstration projects.

Table 3: Table showing the highlights of the samples obtained from three demonstration projects for metallurgical evaluation of

Source	**Component Type**	**Application**	**Typical Dimensions in. (mm)**		**Number of samples**
			OD	**ID**	
Project 1	Tube-to-tube butt welds	Heat exchanger tubes	1.5 (38)	0.125(3.2) to 0.250 (6.4)	5
Project 3	Instrumentation tee	Site for instrumentation			1
Project 2	Pipe-to-pipe butt welds	Turbine exhaust piping	6.15 (0.242) to 7.77 (0.306)	304.8 (12)	4

Sample preparation steps for metallography and characterization (sectioning, polishing etching)

For metallurgical characterization, select welds from the gathered group of component samples were prepared for metallographic analysis. Typical preparation process involved controlled sectioning of the welds at locations that best show the characteristics of crack progression followed by standard metallurgical sample preparation steps. Sectioning of the samples was performed using electro discharge machine and the sectioned samples were mounted in a conductive phenolic resin to prepare for the polishing steps. Metallographic preparation involved grinding of the mounted specimens using successively finer silicon carbide sanding papers followed by polishing with suspensions containing fine diamond particles. For the final stage of sample preparation, the mounted specimens were polished using a vibratory polisher to a 0.05 μm surface finish.

After sample preparation, the polished samples were first imaged at a macro-scale using an optical microscope in the as-polished condition followed by etching. The samples were etched electrolytically using 2% Nital solution at an applied voltage of 6V for a duration of 5 to 8 seconds. This etching step highlights the grain boundaries in the 740H samples in an optical microscope. The sample cross sections were again imaged post-etching to highlight the underlaying grain structure in the microstructure of the samples. In the following sections, details of samples and characterization results obtained from each of the three projects are discussed in detail.

Characterization studies on 740H weld samples from Demonstration Project #1

Background

Demonstration project #1 involved the construction of a 10MW pilot test facility which uses sCO_2 power cycles to generate power from the recovery of heat originating from a gas fired primary heater [12]. To capture this heat, a high-temperature heater coil module was designed to heat the sCO_2 to desired operating conditions. Due to higher operating conditions than any current state-of-the-art heat recovery steam generator, the heat exchanger tubes for the heater coil were constructed from 740H alloy. The design of the heater coil required over 1,600 welds of varying configuration. Some examples of the different weld configurations included tube to tube bends, tube to tube butt welds, tube-to-header welds, pipe-to-flange girth welds, welds that the header end caps and some dissimilar metal welds. Figure 1a shows the assembled heater coil module and Figure 1b shows welding operations being performed at the return ends of the heat coil.

These shop welds on the heater were made with manual gas tungsten arc welding process and were performed as per ASME B&PV Code Case 2702-3 [13], which required a post weld heat treatment (PWHT). The PWHT operation was performed on the entire assembly by placing it in a heat-treatment furnace and the assembly achieved a uniform temperature between the range 1,400 to 1,500°F (760 to 815°C). The duration of PWHT at this temperature was five hours. Hydrostatic pressure test performed after the PWHT operation indicated 12 leaks in the tube-to-tube welds of the assembly. Figure 2 shows typical appearance of these leaked tubes after OD dye penetrant testing. Five of these twelve leaks were collected for metallographic investigations. Subsequent full volumetric inspection identified additional welds with cracks which did not result in pressure test leakage representing ~3% of the total tube-to-tube butt weld population.

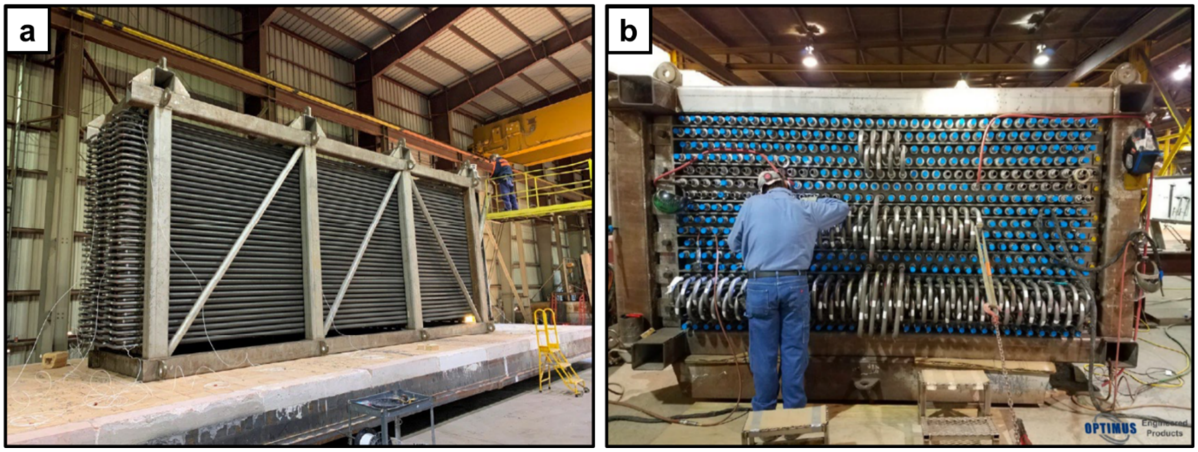

Figure 1: a) Image showing the assembled heater coil module and b) image of welding operating being performed at the return end of the heater coil**.**

Figure 2: Images showing the locations and appearance of the tube leak sites at the tube-to-tube welds after PWHT and hydrostatic testing.

Description of samples received

The five samples that were received from demonstration project #1 are shown in Figure 3. The obtained samples mainly consisted of sections with a tube-to-tube weld in the middle and small amounts of the tube parent materials on either side of the weld. The sample designation and the dimensions of the welded tubes of the 5 samples are provided in Table 4. Among the five samples, only the welded tube section ‘Row 3 Weld 3’ had a nominal wall thickness of 0.25 inches. Location within the boiler was provided but orientation relative to the tube bends was not indicated.

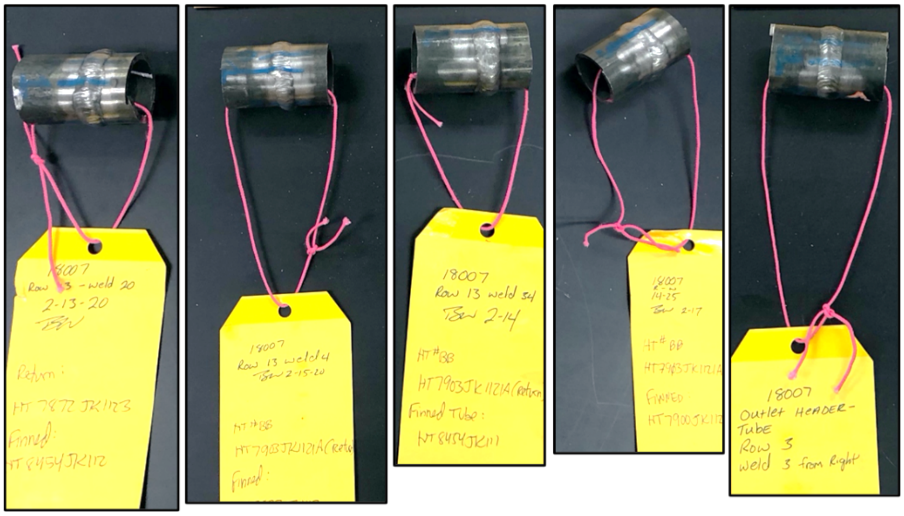

Figure 3: Images of the five as-received sections of the tube-to-tube welds where through wall leaks were identified. These sections were obtained for metallographic investigations

Table 4: Sample ID and the nominal tube dimensions of the five samples obtained from demonstration project #1.

Tube/ Pipe ID	Nominal Dimensions in. (mm)	
	OD	WT
Row 3 Weld 3	1.5 (38)	**0.250 (6.4)**
Row 13 Weld 4	1.5 (38)	0.125 (3.2)
Row 13 Weld 20	1.5 (38)	0.125 (3.2)
Row 13 Weld 34	1.5 (38)	0.125 (3.2)
Row 14 Weld 25	1.5 (38)	0.125 (3.2)

Experimental procedure & results for failure investigation

NDE and Sectioning for metallography

Failure investigation on these cracked samples was initiated by first performing an NDE evaluation. The tubes were first split along the tube length with precautions to avoid cutting into any of the marked locations with cracking as shown in Figure 4a. Liquid dye penetrant testing (LPT) was then done on both the ID and OD surfaces of the split tubes to determine the location and extent of cracking in these tubes. Figure 4b shows the through-wall crack in a split section of the tube in one of the samples as seen after LPT at the OD and ID surfaces and Table 5 summarizes the observations from the LPT testing of the five tubes.

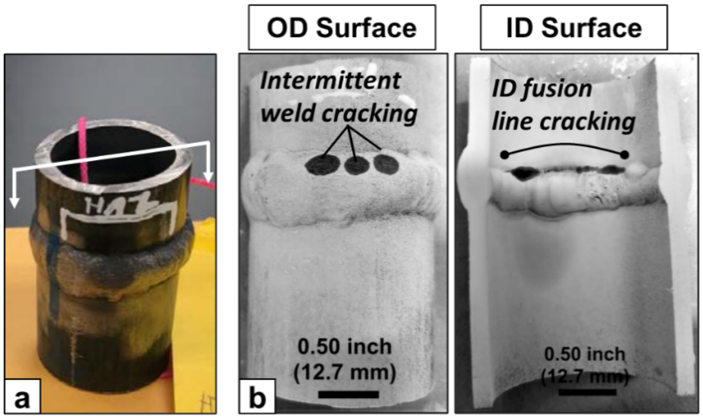

Figure 4: Images outlining a) how the obtained tube welds were sectioned axially and b) one example of OD and ID surface appearance indicating a through-wall crack after LPT.

Table 5: Summary of observations from LPT testing on the five tubes.

Identification	Observations from LPT Testing		
	Observations	Crack Location	Weld profile
Row 3 - Weld 3	A crack running halfway between the weld toe and centerline is present at OD surface	Weld metal OD, weld toe on ID	Significant pushthrough
Row 13 - Weld 4	A crack running along the ID weld HAZ	Weld toes at both OD and ID	Moderate pushthrough
Row 13 - Weld 20	A crack running along the ID toe of the weld.	Weld toe at ID surface. No indication at OD	Significant pushthrough
Row 13 - Weld 34	A crack running along the ID in the weld HAZ	Weld metal OD, weld toe on ID	Small pushthrough but very tall OD weld profile
Row 14 - Weld 25	A crack running along the weld toe/HAZ then transitioning into the base metal	Weld metal to base metal on OD, FL to base metal on ID	Apparent misalignment of tubes, moderate pushthrough, non-uniform weld profile

Following LPT testing, the tubes were marked for sectioning for sample preparation and metallographic examination. Multiple axial (lengthwise) sections were taken from each of the five tubes at the locations of the cracks to capture the initiation and propagation of the cracks. Figure 5 shows the locations where the tube sections were marked for sectioning. These sections were mounted and polished and examined in both etched and unetched conditions.

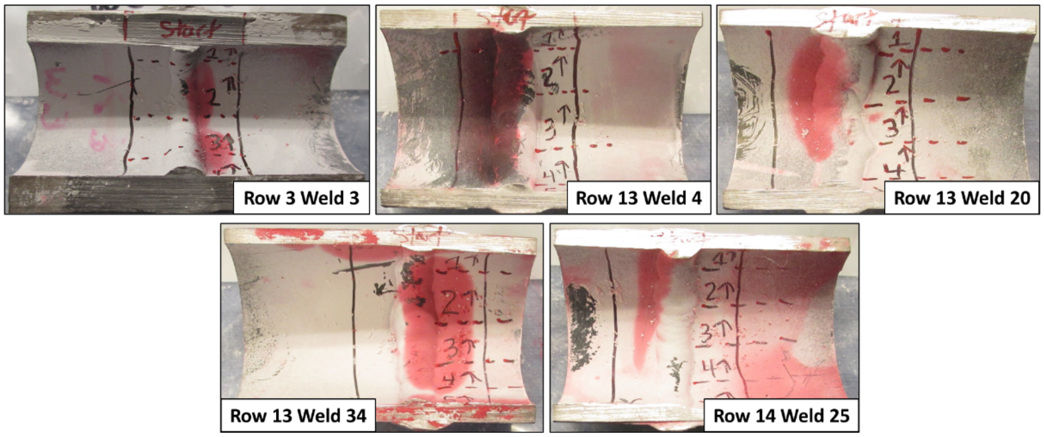

Figure 5: The sectioning locations for the five tubes near the sites with cracks.

Analysis of tube compositions:

The complete composition of tubes that exhibited cracking in the five tube-to-tube welds were first analyzed to determine whether the cracked tubes conformed with the compositional requirements for the material UNS N07740. This investigation also included analysis of trace elements such as As, Sb, Sn. Inductively coupled plasma (ICP) mass spectroscopy (MS), ICP-Optical Emission Spectroscopy (OES), Combustion technique and Inert Gas Fusion (IGF) methods were employed to determine the complete composition of the tubes, as any one analysis method is insufficient for the determination of the metal composition. Table 6 shows the composition of the five tubes with cracks in the five 740H tube-to-tube welds. Also shown in the table is the allowable composition ranges (minimum to maximum) for certain elements in 740H in the row *'UNS N07740'.* From the results of this analysis, the cracked tubes met the compositional requirements of UNS N07740 material.

Table 6: Complete composition of the cracked tubes:

Element	Cr	Co	Al	Ti	Nb + Ta	Fe	C	Mn	Mo
UNS N07740	*23.5 - 25.5*	*15.0-22.0*	*1.35-2.00*	*0.5-2.5*	*0.5 - 2.5*	*0-3.0*	*0.005-0.008*	*0 - 1.0*	*0 - 2.0*
R13W4	24.605	19.814	1.548	1.494	1.498	0.30	0.033	0.28	0.51
R3W3	24.437	20.682	1.535	1.466	1.474	0.10	0.035	0.27	0.49
R13W20	24.204	19.642	1.517	1.466	1.479	0.29	0.034	0.27	0.5
R14W25	24.821	20.942	1.513	1.497	1.497	0.09	0.033	0.28	0.5
R13W34	24.396	20.846	1.477	1.476	1.479	0.09	0.033	0.28	0.5
Element	**Si**	**Cu**	**P**	**S**	**B**	**Ca**	**La**	**Ta**	**V**
UNS N07740	*0 - 1.0*	*0-0.5*	*0-0.03*	*0-0.03*	*0.0006 - 0.006*	-	-	-	-
R13W4	0.197	<0.002	<0.002	<0.0005	0.0013	<0.0005	<0.002	<0.002	0.006
R3W3	0.202	<0.002	<0.002	<0.0005	0.0011	<0.0005	<0.002	<0.002	0.007
R13W20	0.187	0.004	<0.002	<0.0005	0.0013	<0.0005	<0.002	<0.002	0.006
R14W25	0.199	<0.002	<0.002	<0.0005	0.0007	<0.0005	<0.002	<0.002	0.007
R13W34	0.204	<0.002	<0.002	<0.0005	0.0012	<0.0005	<0.002	<0.002	0.006

Table 6 (cont.): Complete composition of the cracked tubes:

Element	**W**	**Zr**	**As**	**Bi**	**Pb**	**Sb**	**Sn**	**O**	**N**
UNS N07740	-	-	-	-	-	-	-	-	-
R13W4	<0.002	0.025	<0.001	<0.0001	0.00002	<0.0001	<0.001	0.0002	0.0066
R3W3	<0.002	0.023	<0.001	<0.0001	0.00003	<0.0001	<0.001	0.0003	0.004
R13W20	<0.002	0.023	0.001	<0.0001	0.00002	<0.0001	<0.001	0.0002	0.0073
R14W25	<0.002	0.025	0.001	<0.0001	0.00003	<0.0001	<0.001	0.0002	0.0035
R13W34	<0.002	0.025	0.001	<0.0001	0.00002	<0.0001	<0.001	<0.0001	0.0038

Macro-scale Imaging and Characterization

Figure 6 shows a series of five cross-sectional images (marked #1 to #5) obtained after polishing of the machined sections from the sample 'Row 3 Weld 3'. These images show that the sections marked #1 and #2 did not have any indications of cracks. But the sections #3, #4 and #5 all show cracks and the successive images provide an indication of the path of crack growth. In this sample, cracking appears to have initiated at or near the toe of the weld (the initiation point lies at a location between the sections #2 and #3). The growth of the crack appears to be within the HAZ initially, which then transitions into the weld. Similar images showing the progression of cracks in the remaining tube samples are shown in *Appendix A*.

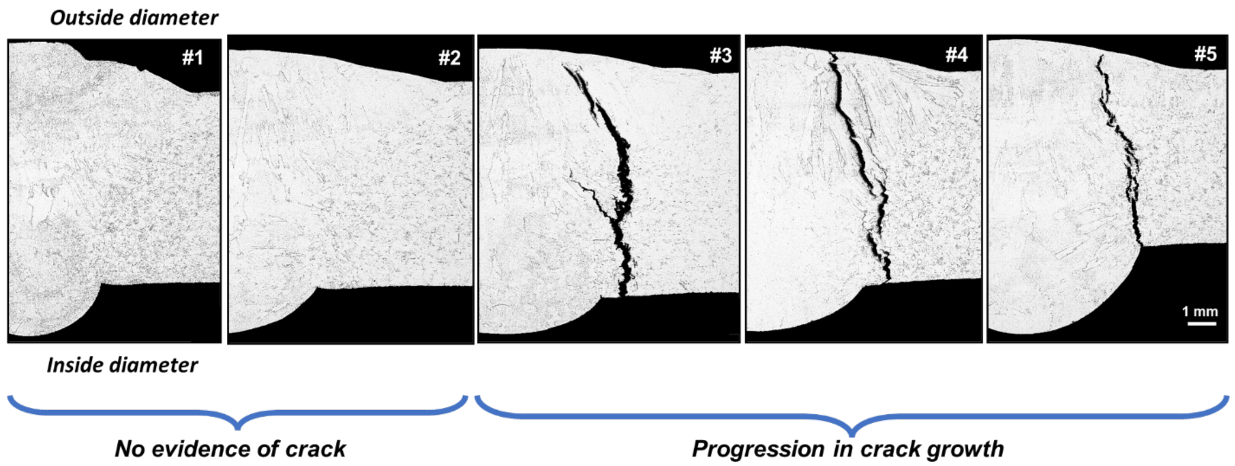

Figure 6: Metallographic images of the polished sections of sample Row 3 Weld 3 showing the progression of cracking around the tube circumference

These images in Figure 6 also show that the main crack appears to have very little branching and there were no clear indications of secondary cracks surrounding the main crack. Initiation of the crack at or near the toe of the weld may further suggest that geometrical factors that increase local stress concentration, may play a part in the formation of these cracks. Figure 7 shows one representative weld cross section each from the five welded tubes. All these images show cracks originating at the toes of the welds. The images also show that all the welds had marked weld pushthrough at regions near cracking, sometimes even greater than the wall thickness for the tubes, which could result in a significant build-up of residual stresses at the toes of the welds. These findings also highlight the variability in quality of workmanship in making these weld. Additionally, it is also interesting to note that cracks were present at only one of the weld toes at the ID in each of the five samples. Another important observation from cross sectional images was that there is no clear association of crack formation with the wall thickness of the tubes and, in multiple instances, cracking in the weld was on the tube with higher wall thickness. This suggests a local stress concentration because if strain was uniformly distributed across the weldment, the thinner sections would be expected to have higher stresses and the thicker sections lower stresses, resulting in failure on the thinner tube.

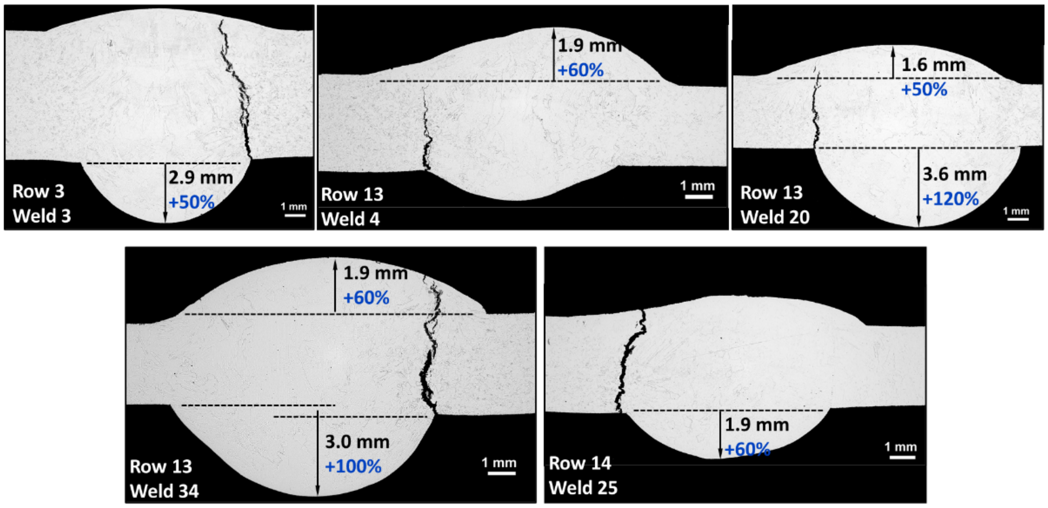

Figure 7: Images outlining the sectioning locations for the five tubes near the sites with cracks.

The grain structure of the tubes was revealed by etching the polished surfaces and Figure 8 shows a representative etched cross section as imaged using a light optical microscope. The etched microstructure of the welds primarily shows an equiaxed grain structure in both the base materials and a typical columnar and equiaxed dendritic microstructure within the weld.

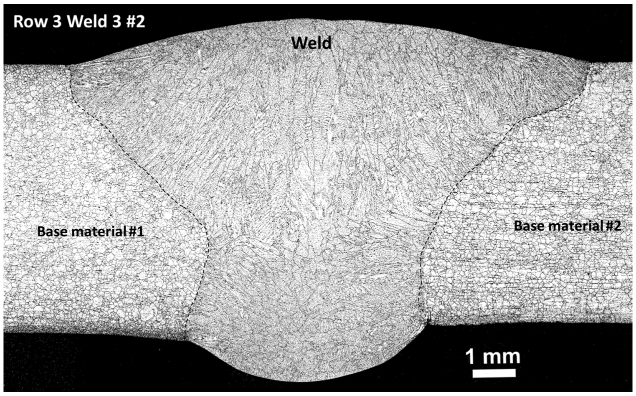

Figure 8: Typical etched microstructure of the welded tubes when observed using a light optical microscope.

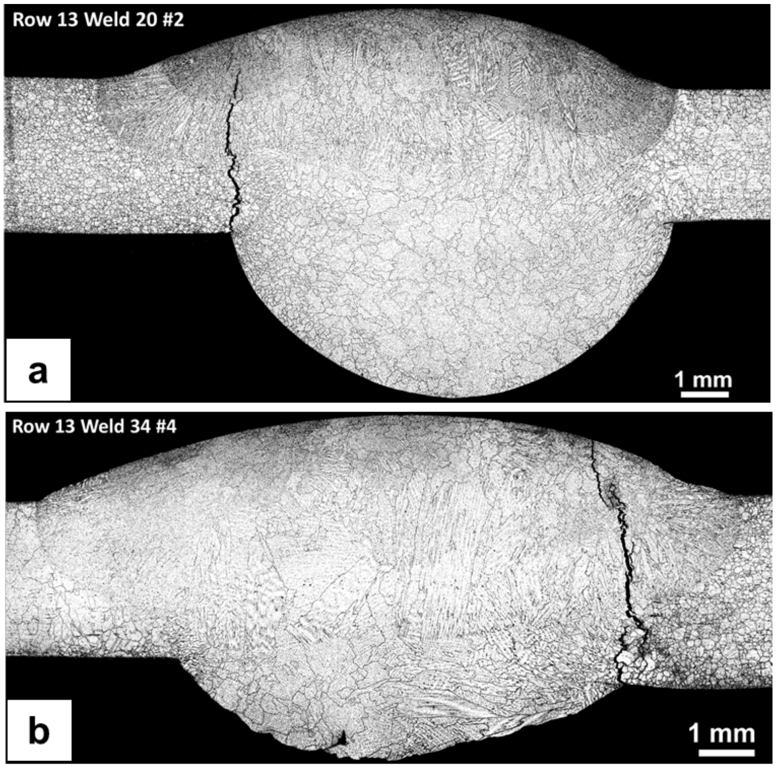

Figure 9: Etched weld microstructures of one of the cross sections taken from a) sample Row 13 Weld 20 and b) Row 13 Weld 34.

Figure 9a and Figure 9b each show similarly etched macro images of the one of the weld cross sections from samples ‘Row 13 Weld 20’ and ‘Row 13 Weld 34’. These images again confirm that cracks were originating from or near the toes of the welds in these samples. Another important observation made from these etched samples was that the cracks had formed on the side of the weld where the base material has finer grains. For example, in sample Row 13 Weld 20, the grain size of the base material that had cracked ranged between ~80 to 250 µm, whereas the grain size of the tube with no evident crack formation was in the range of ~100 to 650 µm. In this example, the base material that did not show any cracks had prominently large grains distributed within the matrix.

An additional observation that highlights the characteristics of this cracking mechanism was that these cracks were intergranular in appearance. This observation was consistent in all the successive sections across the cracks taken from each of the five cracked samples. Figure 10a and Figure 10b shows two sections across the crack in the sample ‘Row 13 Weld 20’ which clearly show that the growth of the crack in the HAZ and in the weld were intergranular in appearance. The intergranular nature of cracking and the origination of cracks at the toes of the welds suggest that studying: 1) the grain boundary characteristics at the regions with and ahead of the crack and, 2) the environment at the toes of the welds on the side with cracks, would be important in understanding the underlying contributing factors to the formation of such cracks. To perform this analysis, the use of advanced characterization tools that can interrogate the material in the micro and nano-scale, are required.

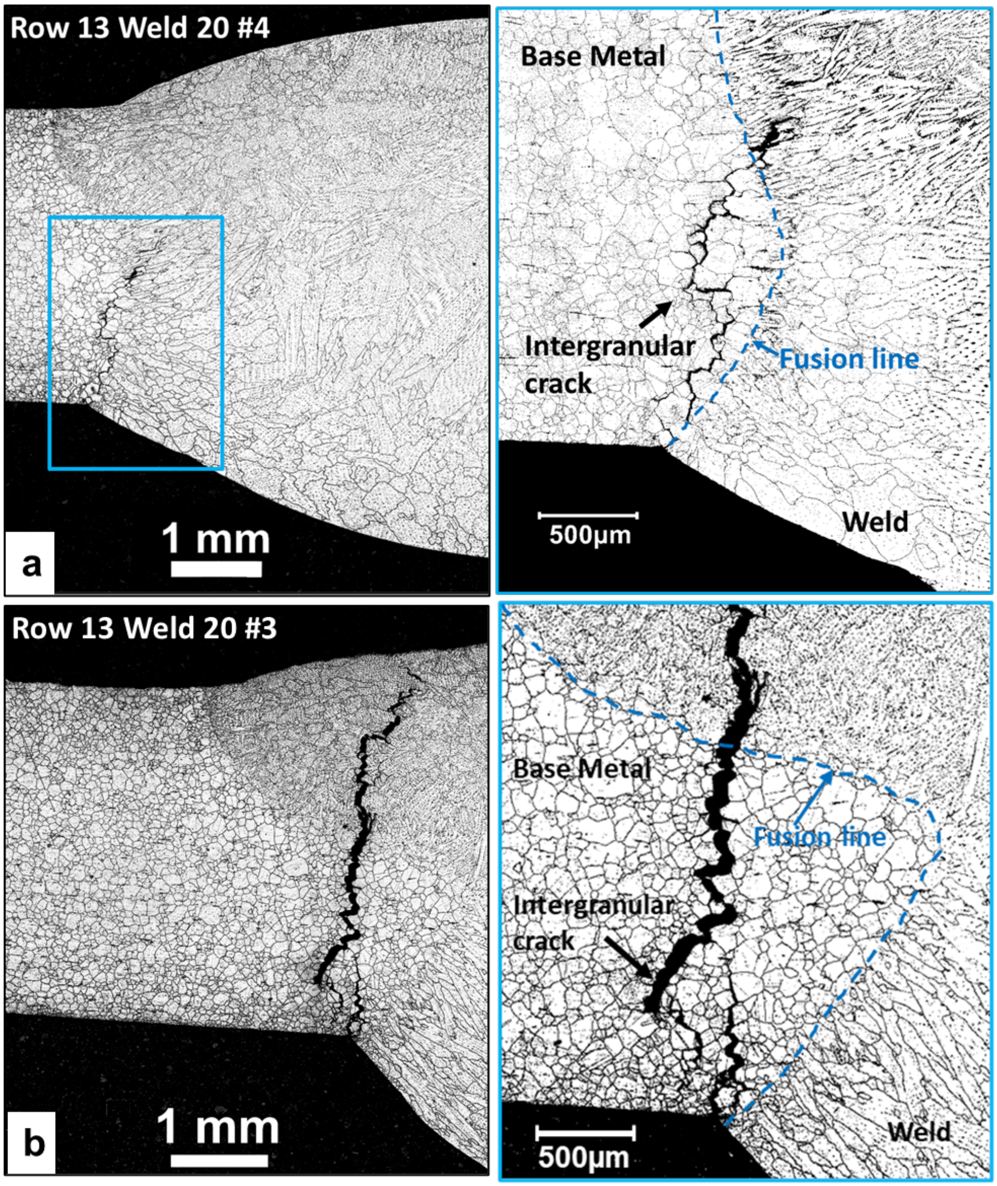

Figure 10: Lower and higher magnification images of the cracks in sections a) Row 13 Weld 20 #4 and b) Row 13 Weld 20 #4 showing that the growth of the crack formed is intergranular.

Since the observed cracks appear to be originating from the toes of the welds, microhardness testing was performed to determine whether there was any local hardening occurring at these sites and if there was any clear association of hardness and crack formation. Microhardness testing was done by applying a grid of microhardness indents on the cross section of a sample and generating a microhardness distribution map from the results of the hardness indents. Figure 11 is a hardness distribution map generated from the results of over 2,300 microhardness indents made over the sample cross-section ‘Row 13 Weld 34 #3’. A 500g load was used for hardness testing. The hardness distribution map shows that the range of hardness within the weld metal was ~320 to ~380 HV, whereas the hardness at both base metals was in the ~360 to 380 HV range. From the map, there were regions of local hardening at the ID weld toes, where the hardness values were ~380 HV. However, this increase was evident on both weld toes and did not in itself explain the formation of a crack on one side of the weld.

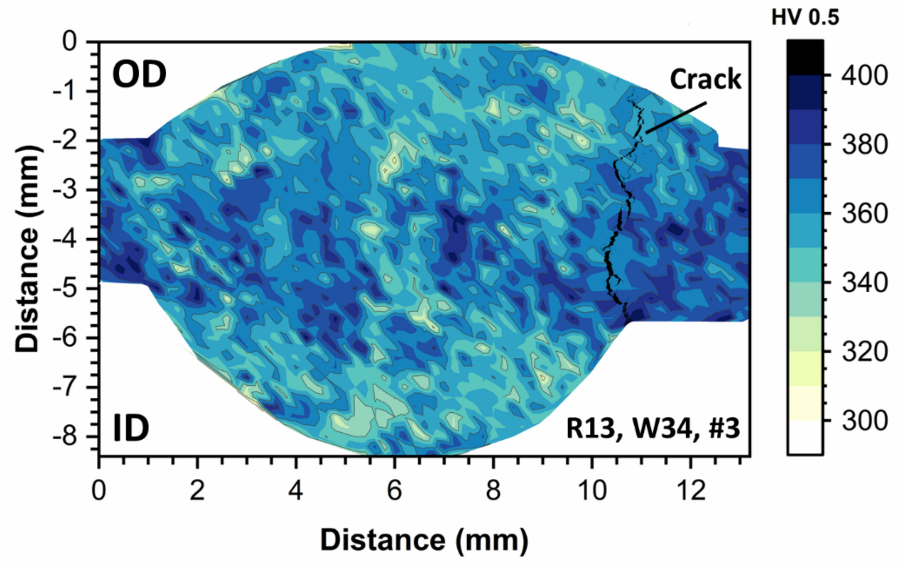

Figure 11: Microhardness distribution map on the cross-section Row 13 Weld 34 #3.

Micro-scale Imaging and Characterization

For micro-scale characterization of the regions surrounding the sites with cracking, cross-section samples from the five tube-to-tube welds were studied using a scanning electron microscope (SEM). A combination of secondary electron (SE) and backscattered electron (BSE) imaging modes were used to capture images of the microstructure near these cracks. Figure 12 shows backscattered images of the unetched cross sections of metallographic samples from two different tubes (Row 13 Weld 4, Row 13 Weld 20). Both images confirm that the cracks appear to be originating from the weld toe and that the cracks are intergranular in nature.

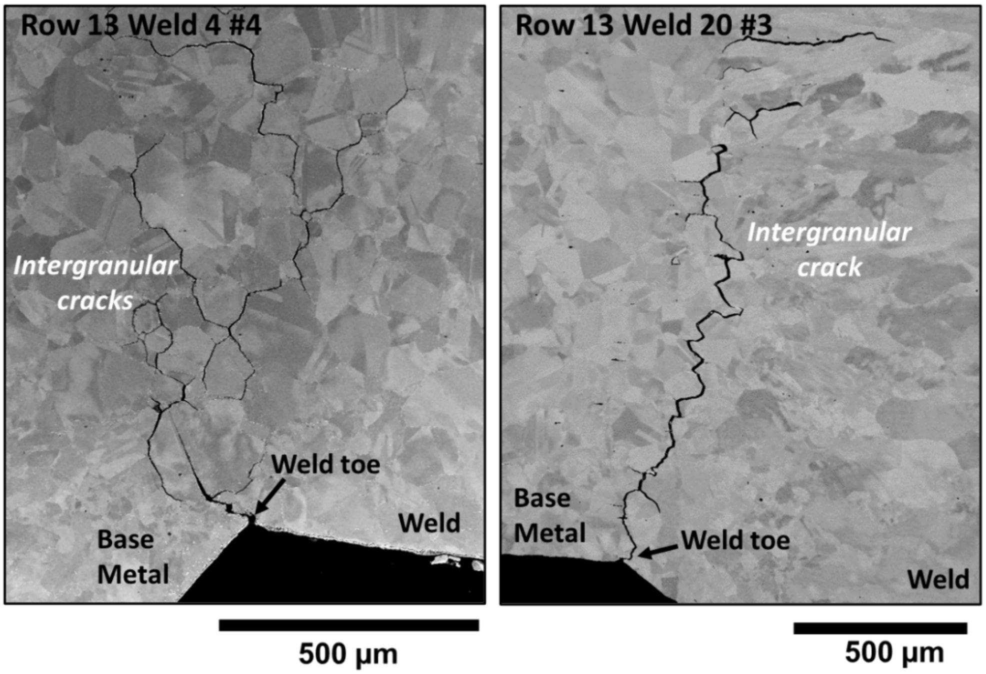

Figure 12: BSE images from the weld toes of cross sections from two samples a) sample Row 13 Weld 4 #4 and b) Row 13 Weld 20 #3, showing that the cracks formed are intergranular.

When analyzing the microstructure of a sample in unetched condition using the BSE imaging mode of an SEM, the grain structure of the metal can be distinctly visualized by increasing the contrast of an image. In such an imaging method, individual grains in the material will be evident even in unetched condition and, typically, each grain will have a unique greyscale contrast compared to its surrounding grains. This greyscale value is based on the amount of backscattered electron signal reaching the detector from that grain and is dependent on the orientation of that grain. Adjacent grains can hence be differentiated based on differences in their greyscale values due to differences in their relative orientations. As an example, Figure 13a shows a BSE image of the microstructure from an unetched austenitic stainless steel. In this image, the grain structure of the steel is clearly evident because of the differences in the greyscale contrast between adjacent grains. This method of imaging is known as imaging using electron channeling contrast. Similar images were taken from cross sections of one of the cracked tube-to-tube weld samples. Figure 13c and Figure 13d show BSE SEM images from the OD and ID regions of the weld cross section Row 3 Weld 3 #2 and Figure 13b shows the locations where these images were obtained from in a macro image. From these images, the grain structure near the tube OD shows equiaxed grains with twins. However, Figure 13d obtained from the region near the weld ID toe, the microstructure shows significant non-uniform distribution of greyscale coloration and the distinction between the grains cannot be made clearly. This non-uniform greyscale color distribution is typically seen in microstructure of material systems with strain within the matrices.

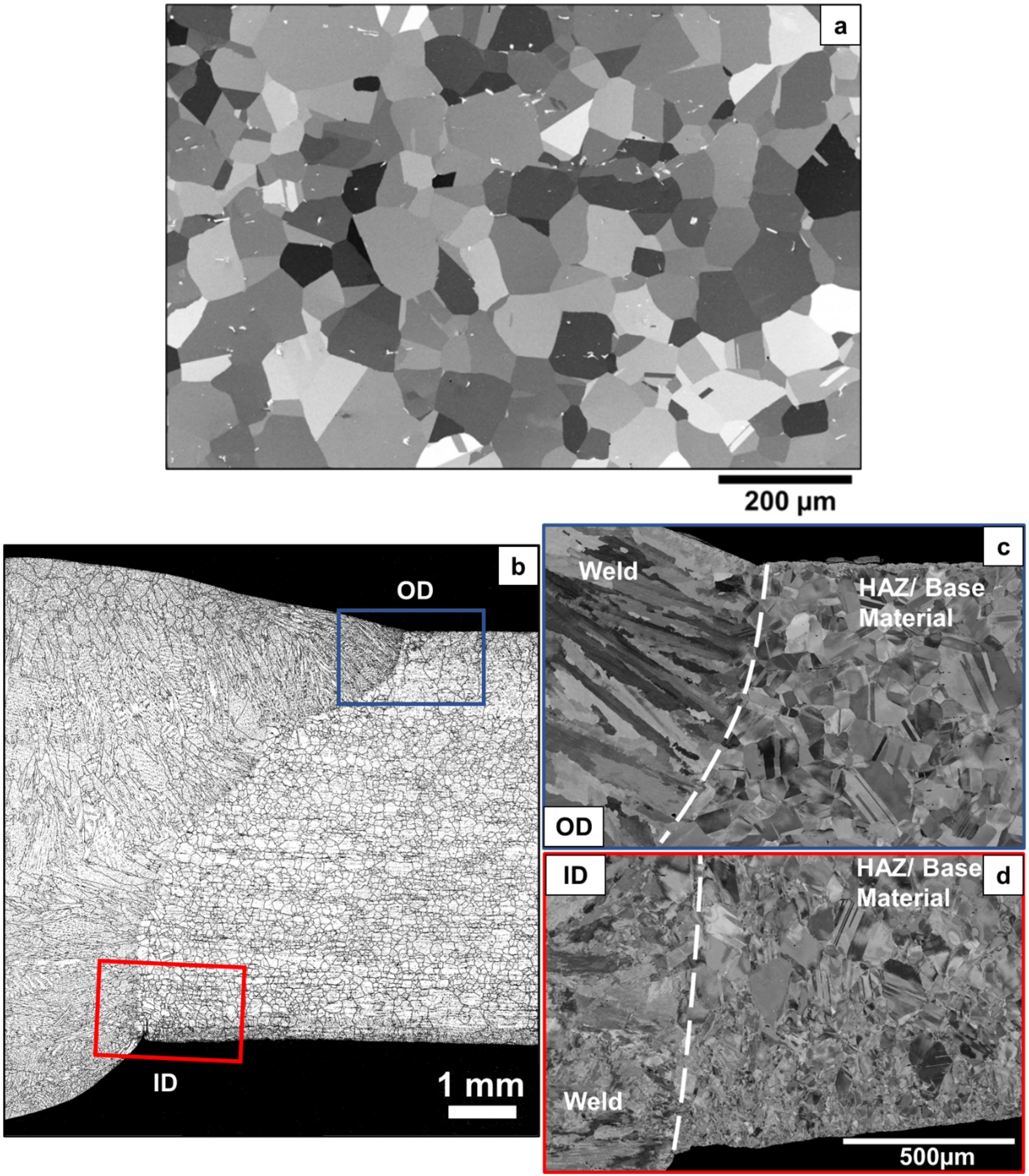

Figure 13: (a) unetched ‘strain-free’ austenitic stainless steel and (b-d) representative BSE images from the OD and ID regions of a weld cross section sample Row 3 Weld 3 #2.

This phenomenon is further emphasized in Figure 14, which is a higher magnification image of the microstructure at the ID region of one cross section from weld Row 3 Weld 3. In this image the non-uniform greyscale coloration both within the grains and at the grain boundaries is evident and is more pronounced at the grain boundaries. These observations suggest concentration of strain at the grain boundaries of the microstructure at the ID regions of the tube sections.

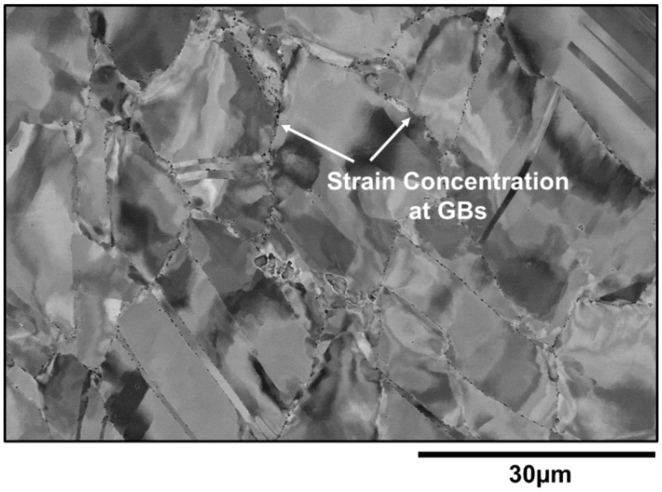

Figure 14: Higher magnification BSE images from the ID region of a weld cross section from sample Row 3 Weld 3 #2.

The microstructure near the toes of the weld with cracking also showed indication of strain in the matrix as is evident in Figure 15a taken from sample Row 3 Weld 3 #1. Furthermore, when the microstructure was analyzed at higher magnification, there was evidence of formation of fine grains (<10μm) right at the weld toe within a region marked in Figure 15b. These grains also have a relatively more uniform greyscale coloration compared to the surrounding matrix, which suggested that the grains had relatively lower strain than the matrix surrounding it. This combination of smaller grain sizes along with lower strain within this zone of fine grain indicated that these were recrystallized grains that have formed at the weld toe. These observations further suggest that the weld toes were regions with signification stress concentration resulting in local strain accumulation at the matrix to the extent that recrystallization phenomenon may also occur at these regions.

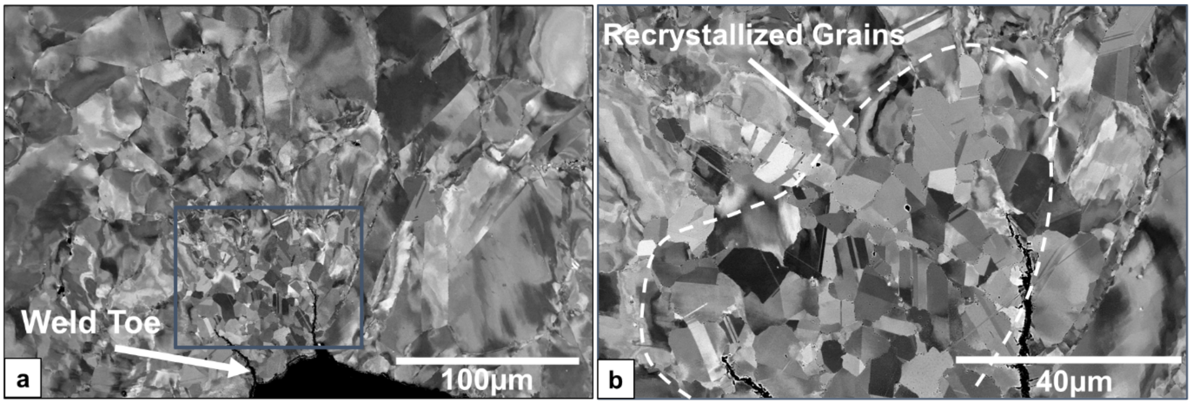

Figure 15: BSE a) low magnification and b) higher magnification of grains near the ID weld toe of a weld cross section from sample Row 3 Weld 3 #1.

Similarly, the etched microstructure at the ID weld toe of the weld cross section Row 3 Weld 3 #2 is shown in the Figure 16. The etching process mutes the electron channeling response resulting in a BSE image that does not have the vibrant variation in contrast seen in unetched images. In Figure 16b, the presence of fine recrystallized grains at the toe of the weld is evident, an observation that remained consistent with that from the sample from adjacent section (Row 3 Weld 3 #1). The etching process reveals precipitate features within the matrix (Figure 17a) and grain boundary features (Figure 17b) that were not very evident in an unetched microstructure. From the images of etched microstructures, it is clear that the interiors of the grains contain a uniform distribution of very fine precipitates. From the physical metallurgy of alloy 740H [1], these matrix precipitates are expected to be the finely dispersed γ' precipitate ($Ni_3(Al,Ti,Nb)$ precipitates) which are the primary contributor to the high temperature strength of this alloy. However, the grain boundaries at these regions with recrystallized grains show interesting features.

The boundaries showed different precipitate structures, which include large and blocky precipitates that appear bright in BSE images and thin, elongated precipitates that appear to be growing away from the grain boundaries and into the matrix of the grain, as highlighted in Figure 18a. Such formations of elongated precipitates are also called *discontinuous coarsening* or *discontinuous precipitation* due to the spaces between the elongated precipitates. Additionally, at these grain boundaries, there were clear regions where there were no precipitates (either large or fine). Such locations that are free from precipitates are termed *denuded zones* or *precipitate free zones* (PFZ) and have been known to form in the weld metal of 740H welds [14, 15]. However, this is first known study where their formation in the base material has been observed during fabrication of a component.

Additionally, it was also observed that the formation of such PFZs was limited to the recrystallized regions at the HAZ and farther away from this region, the grain boundaries did not show formations of such precipitate denuded regions. For example, Figure 19 shows lower and higher magnification images of grain boundaries situated < 5 mm away from the fusion boundary and near the tube ID, where the boundaries also show bright appearing blocky precipitates and finer grey precipitates, but the elongated shaped precipitates or discontinuous precipitation seen in Figure 18 are missing at these boundaries. Also missing are the PFZs that were present at the boundaries near the recrystallized grains and these grain boundaries appear to have complete coverage with different precipitates. Boundaries shown in Figure 19 and similar boundaries away from the toe of the weld had intragranular precipitates in the matrix forming right up to the boundary.

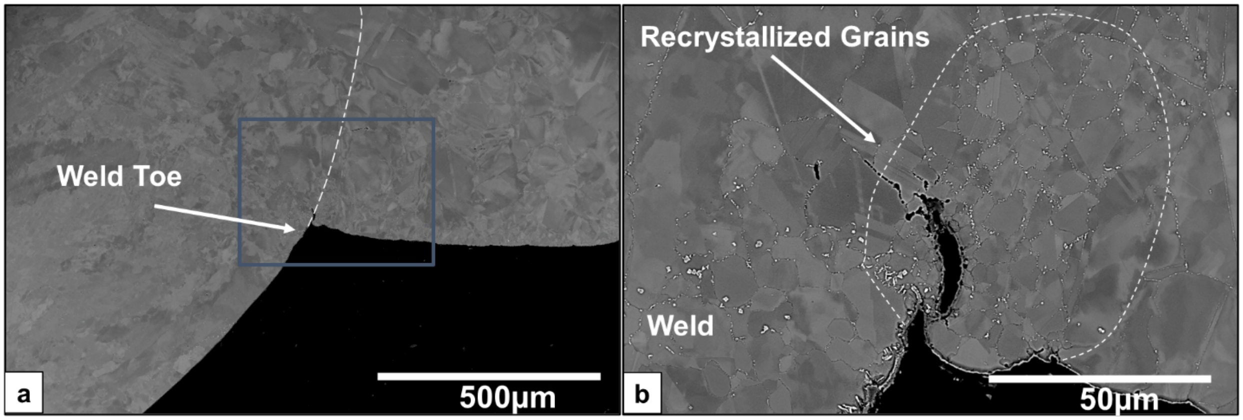

Figure 16: BSE a) low magnification and b) higher magnification images of etched grains near the ID weld toe of a weld cross section from sample Row 3 Weld 3 #2.

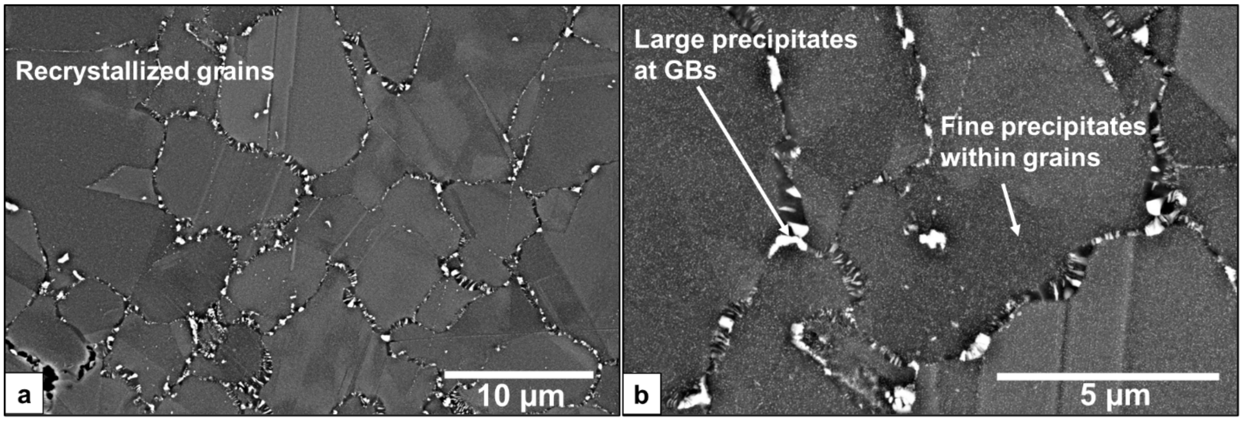

Figure 17: BSE a) lower magnification and b) higher magnification images of etched grains near the ID weld toe of a weld cross section from sample Row 3 Weld 3 #2 showing various precipitate features.

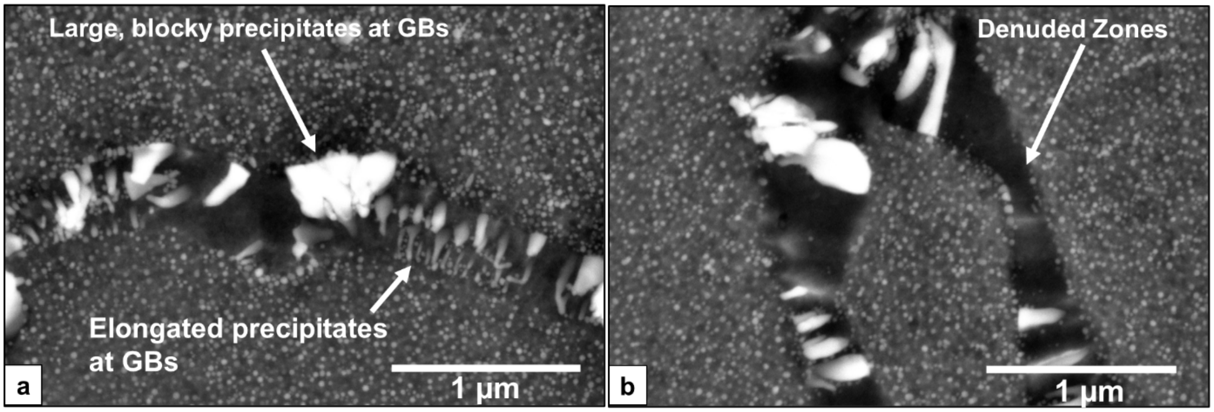

Figure 18: BSE images of etched grains near the ID weld toe of a weld cross section from sample Row 3 Weld 3 #2 showing various precipitate features at the boundary and formation of precipitate free zones.

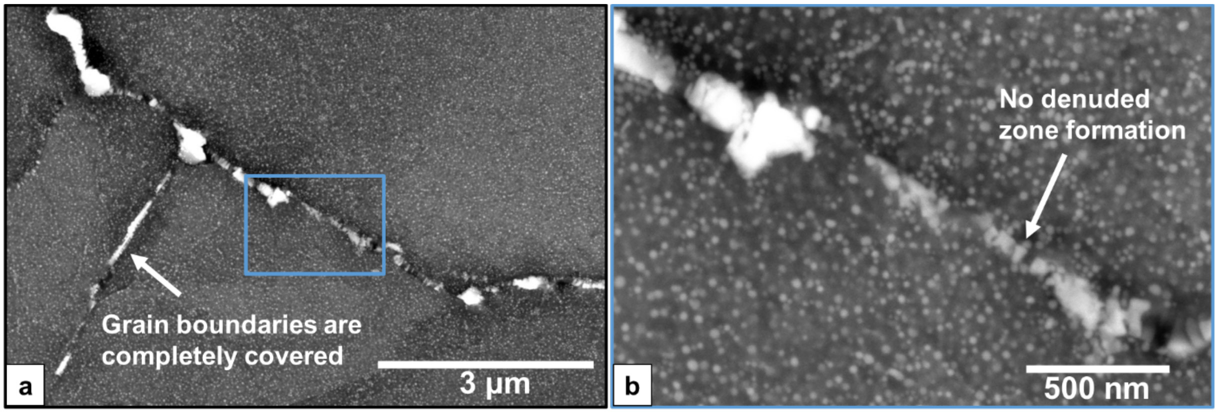

Figure 19: BSE images of etched grains from regions away from the ID weld toe of a weld cross section from sample Row 3 Weld 3 #2, showing various precipitate features at the boundary and no precipitate free zone formation.

All the above findings were from cross-sections #1 and #2 of the weld Row 3 Weld 3. In these cross-sections, there was no evidence of a crack at the weld toe, although from images Figure 15a and Figure 16b, the weld toes of these sections do seem to have some discontinuities which may have further contributed to increase in local stress concentration. From these analyses, there is clear evidence to suggest that just ahead of the crack initiation site, there is significant build-up of residual stress at the weld toes and, in some instances, the resulting strain on the matrix after welding is sufficiently high to result in recrystallization phenomenon occurring at the weld toe during PWHT. Furthermore, such transformations result in rearrangement/ annihilation of dislocations and grain boundary motion, which could result in the formation of PFZs at these sites.

When looking at the etched microstructure of cross-sections taken across cracks, the grain boundary characteristics at regions near and ahead of the crack are of interest for understanding crack growth characteristics. Figure 20 shows images from the weld toe regions of the sample cross section Row 14 Weld 25 #1. A crack originating from regions near the weld toe is evident in this cross section. The main body of the crack traversed through a portion of the HAZ and transitioned into the weld. This crack was similarly intergranular and had very limited branching or formation of secondary cracking.

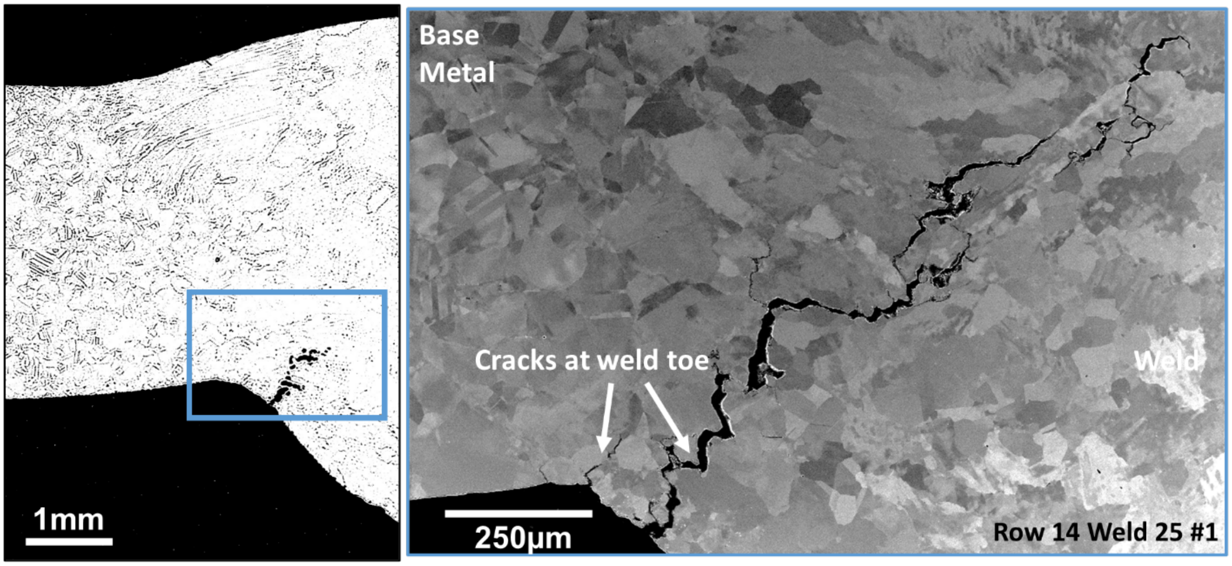

Figure 20: Image showing presence of an intergranular crack originating neat the ID weld toe in the cross section Row 14 Weld 25 #1.

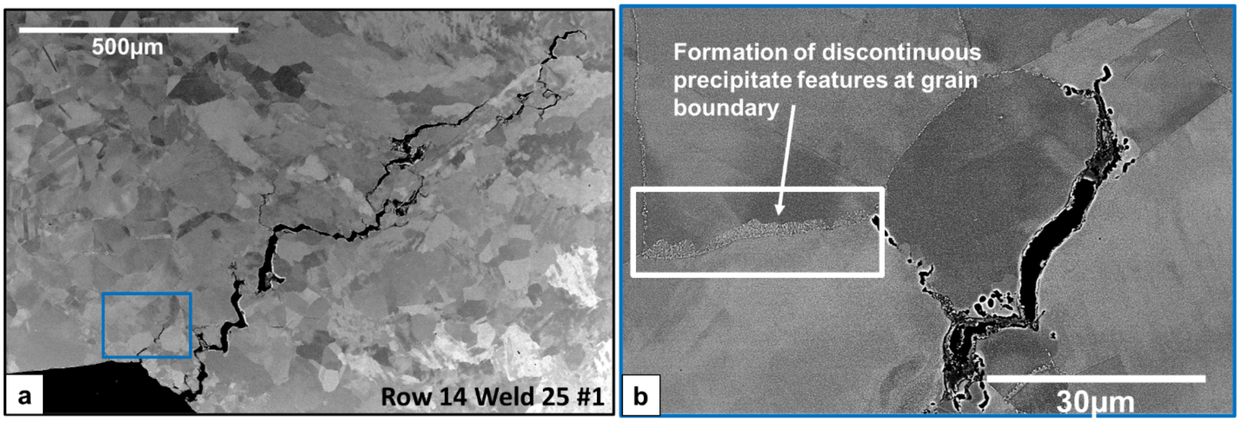

Figure 21: a) BSE images of the crack in Figure 20 showing the location of higher magnification image Figure 21b. b) BSE image showing the formation of discontinuous coarsening at grain boundary ahead of the crack tip.

Two such areas with secondary cracks are highlighted in Figure 21 and Figure 22. In Figure 21, the grain boundary region ahead of the crack showed a large formation of discontinuous precipitate structure highlighted by the white rectangular region in Figure 21a. Figure 22b shows the tip of a secondary crack and the grain boundary structure ahead of the crack. The precipitate structure at the grain boundary consisted of discontinuous blocky precipitates, unlike the elongated discontinuous precipitate structures seen in sample Row 3 Weld 3. In addition, the grain boundary region had <1 µm wide PFZ at the grain boundary, which is further highlighted in the magnified image of the grain boundary in Figure 22b. Furthermore, in isolated locations near the main crack, there was evidence of cavitation damage occurring at grain boundary regions which were denuded of precipitates. For example, Figure 24 shows two instances with locations that showed evidence of cavitation damage at precipitate denuded zones.

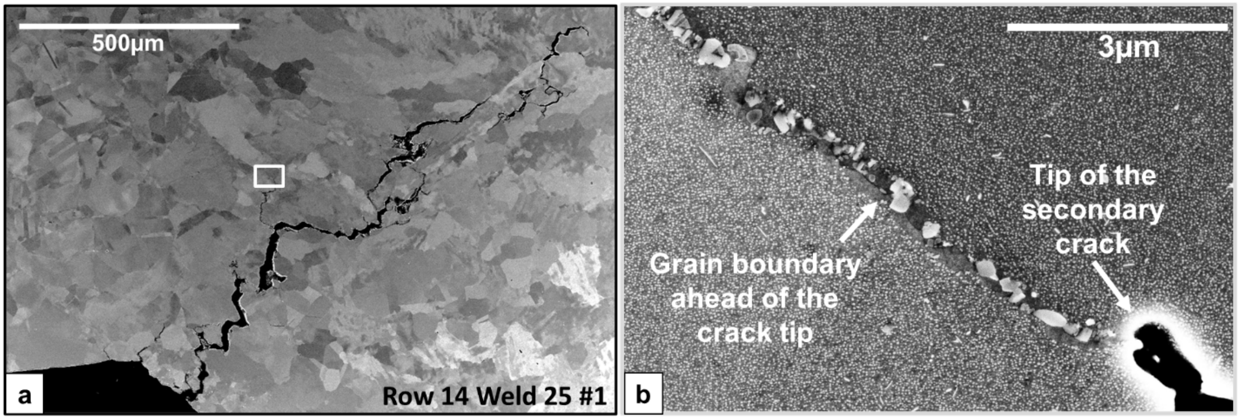

Figure 22: a) BSE images of the crack in Figure 20 showing the location of higher magnification image Figure 22b. b) BSE image showing the formation of discontinuous coarsening and grain boundary denuded zones at grain boundary ahead of the crack tip.

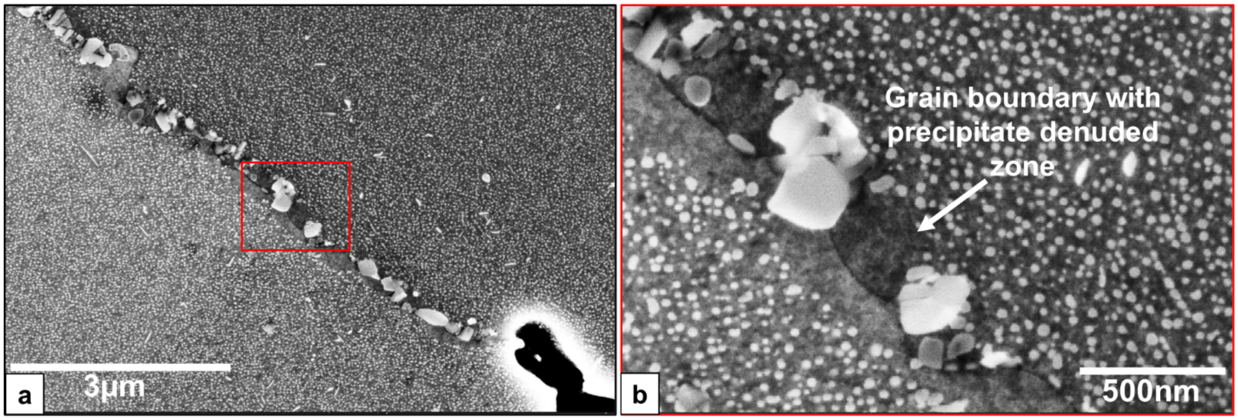

Figure 23: a) BSE images of the crack in Figure 22 showing the location of higher magnification image Figure 22b. b) BSE image showing the formation of discontinuous coarsening and grain boundary denuded zones at grain boundary ahead of the crack tip.

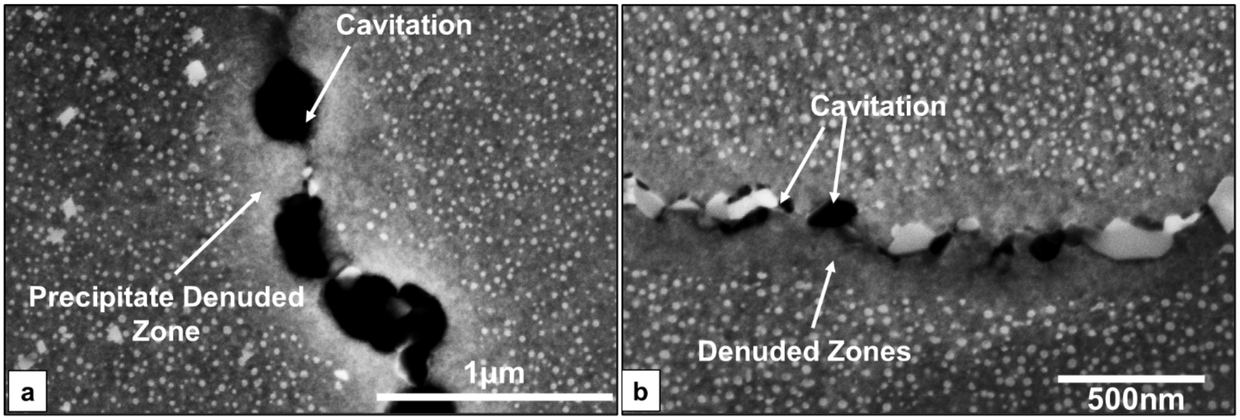

Figure 24: BSE images of grain boundary regions showing regions of cavitation damage at sites with grain boundary denuded zones.

Similar microstructural features were observed in other weld samples and there were clear instances where formation of cavities was also observed ahead of crack tips. Some examples of such occurrences are shown in Figure 24 from two of the five welds Row 13 Weld 4 (Figure 25a) and Row 13 Row 20 (Figure 25b). Such formations of cavities ahead of the crack tip is one well-establish indicator that the cracking mechanism is driven by the relaxation of stresses by accelerated formation of creep cavities and hence termed as a stress relaxation crack (SRxC).

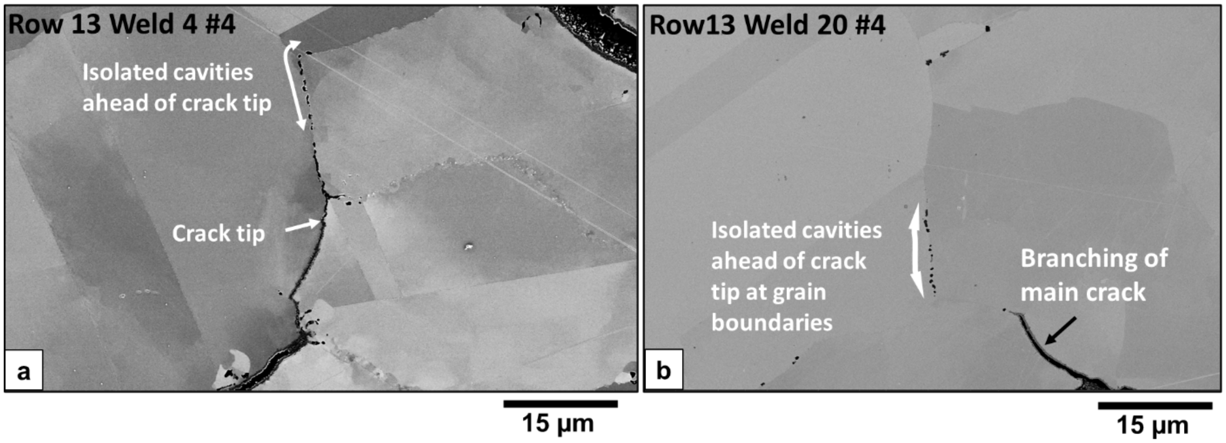

Figure 24: BSE images of grain boundary regions showing regions of cavitation damage ahead of crack tips.

Additionally, the cracks formed on all the five welds contained a surface oxide scale within the crack openings. This finding is highlighted in Figure 25 as one example. Formation of such a scale suggests that cracking must have occurred immediately after the start of PWHT stage of fabrication as NDE evaluation of the welds after the welding operation did not indicate presence of any cracks.

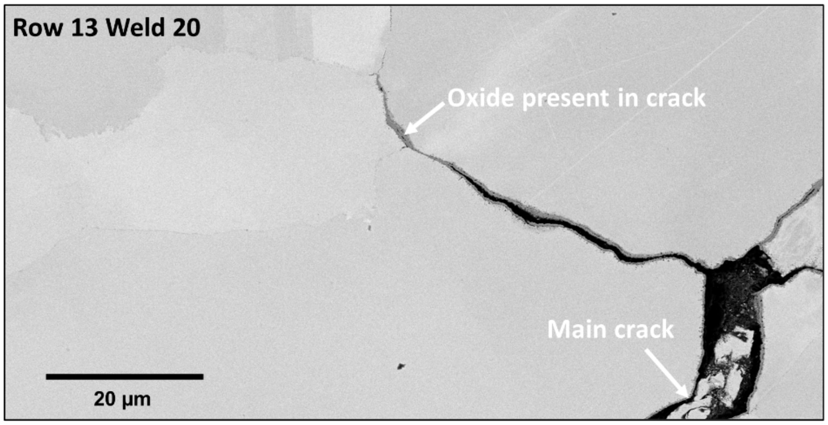

Figure 25: BSE images of grain boundary regions highlighting the presence of oxide scales in grain boundaries

From the above set of observations made from the analysis of multiple sections of the five tube-to-tube welds, cracking in the material appears to initiate at or near regions of the weld toe and grow along grain boundaries by the mechanism that is typically seen in SRxC. One important factor that could be governing the formation and the growth of this crack may be related to the formation of grain boundary denuded zones. These denuded zones are typically accompanied by coarser grain boundary precipitates and these precipitates may either be as discontinuous blocky precipitates at the grain boundary or as elongated discontinuous precipitates. To further understand the characteristics of the grain boundary denuded zone and the accompanying precipitate features, nano-scale characterization studies were performed.

Nano-scale Imaging and Characterization

The grain boundary sites that showed discontinuous precipitate structure formation along with denuded grain boundary regions were studied with the help of a transmission electron microscope (TEM). The sample cross-section Row 14 Weld 2 #1 shown in Figure 20 was chosen as the sample for TEM studies. To primarily establish the precipitate structures formed in a normal grain boundary that did not show any discontinuous precipitation or grain boundary denuded zone formation, a TEM sample was first obtained from a grain boundary present in the non-cracked tube in the weld. Such a representative grain boundary region for baseline TEM analysis was identified and typical appearance of such boundaries are shown in Figure 26 where the grain boundaries have complete grain boundary coverage by precipitates.

One such grain boundary was chosen and is shown in Figure 27a and marked in this image with a white rectangle is the location from which a TEM sample was extracted from this boundary. Sample extraction was performed using a focused ion beam (FIB) milling operation where the surrounding material is first milled away by a trenching operation as shown in Figure 27b. This sample is then lifted out of the substrate material and attached to a TEM sample holder as shown in Figure 27c. In this TEM sample, the grain boundary that was targeted for analysis was found to be extending down into the extracted sample. This sample was further milled to make it thinner and electron transparent and was introduced into a TEM for analysis.

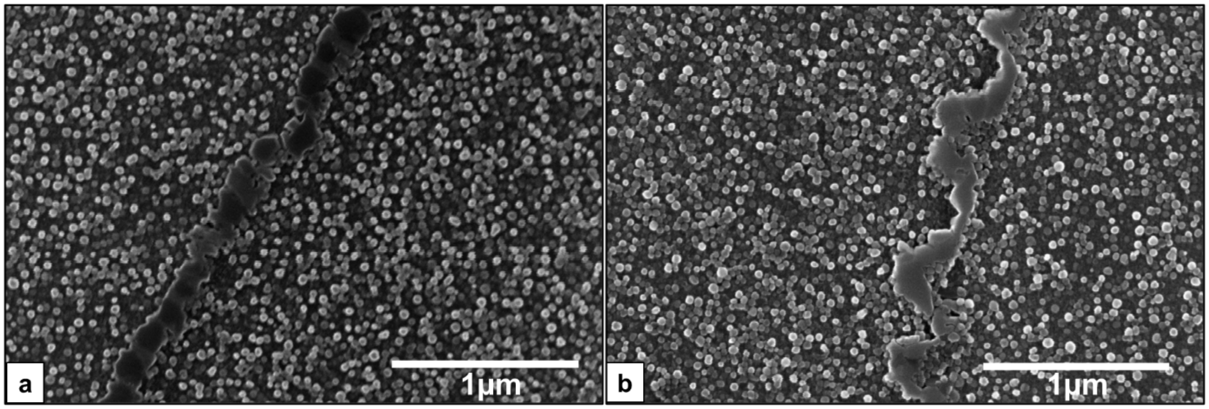

Figure 26: BSE images of grain boundary regions on the non-cracked tube of the weld Row 14 Weld 25 #1 showing complete grain boundary coverage by precipitate structures

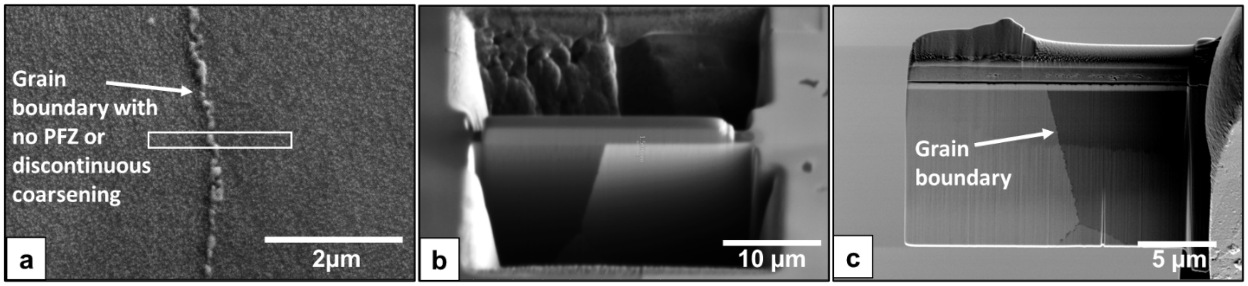

Figure 27: a) BSE images of grain boundary region where TEM sample was extracted, b) FIB trenching operation around area of interest during TEM sample preparation and c) the final TEM sample obtained after sample lift-off from the substrate and attaching to TEM sample holder.

Figure 28 shows a low-magnification bright field (BF) and high angled annular dark field (HAADF) images of the extracted TEM sample. The grain boundary precipitates are visible as dark features along the grain boundary (dotted line) in Figure 28b. From these images, it is evident that the boundary shown in Figure 27a continues to show complete grain boundary coverage even within the sample. To identify the precipitates, present along the grain boundary, energy dispersive spectroscopy (EDS) analysis was performed in the scanning operation mode called scanning TEM mode or STEM mode.

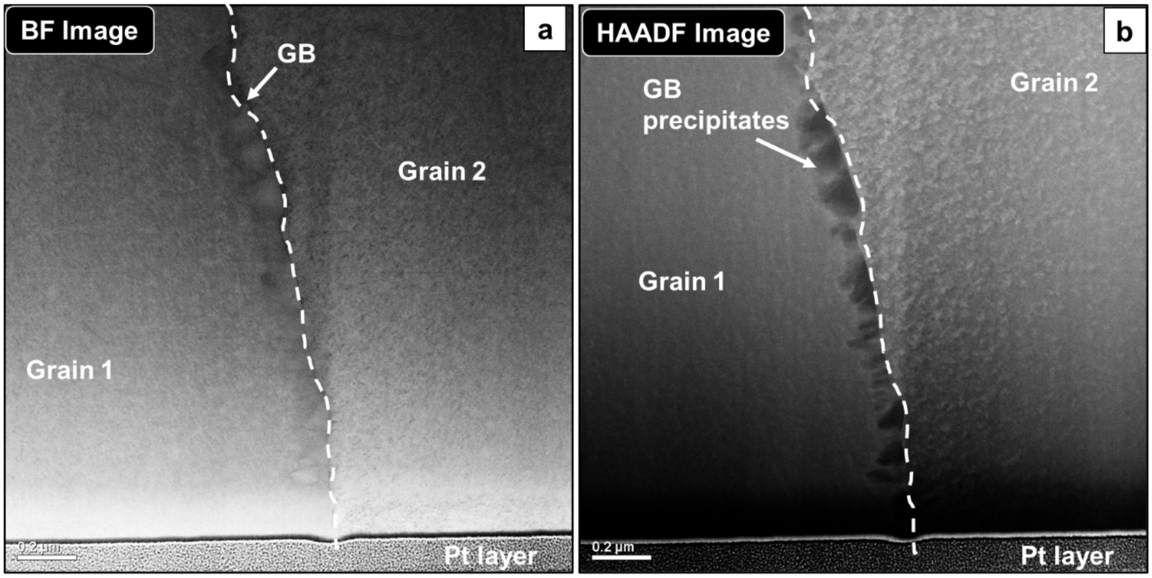

Figure 28: a) Bright field (BF) and b) high angle annular dark field (HAADF) image of the TEM sample cross section showing grain boundary and precipitate features in the middle of the sample.

Multiple line and area EDS scans were performed across the boundary. In EDS analysis, the X-ray signal from the sample is collected as the beam rasters over the sample and the data obtained from each position on the sample is plotted as line intensity maps (for a line scan) or area intensity maps (for area scans) of different elements. Figure 29 and Figure 30 show area EDS results from two different grain boundary regions that show precipitates (the first image in each set of images). In these results, the elemental peak intensity of various elements was plotted over the scanned surface and several important inferences can be made from these results:

1. The matrix surrounding the grain boundary consists of many Al, Ti and Ni rich circular regions which correspond to the fine γ' precipitates in the matrix.
2. The Cr and C distribution map suggests that the grain boundary primarily consists of regions of Cr and C enrichment, which most likely are $M_{23}C_6$ carbides.
3. There is small region in the middle of the scanned area which is enriched in C, Ti, Nb, Mo and V. This element enrichment profile suggests that this feature is a MX type precipitate.

Results from EDS analysis of the second grain boundary region (Figure 30) suggests shows that, in this area, the grain boundary shows two distinct precipitate types. The first is enriched in Al, Ti, Nb and Ni, suggesting that the boundary has a continuous coverage of γ' precipitates. The second set of precipitates show enrichment in Cr and C, indicating $M_{23}C_6$ type precipitates. Results from additional analyses consisting of line EDS scans are shown in the Appendix. From these results, a typical grain boundary in 740H alloy should primarily consist of $M_{23}C_6$ carbides, MX-type carbides and γ' precipitates.

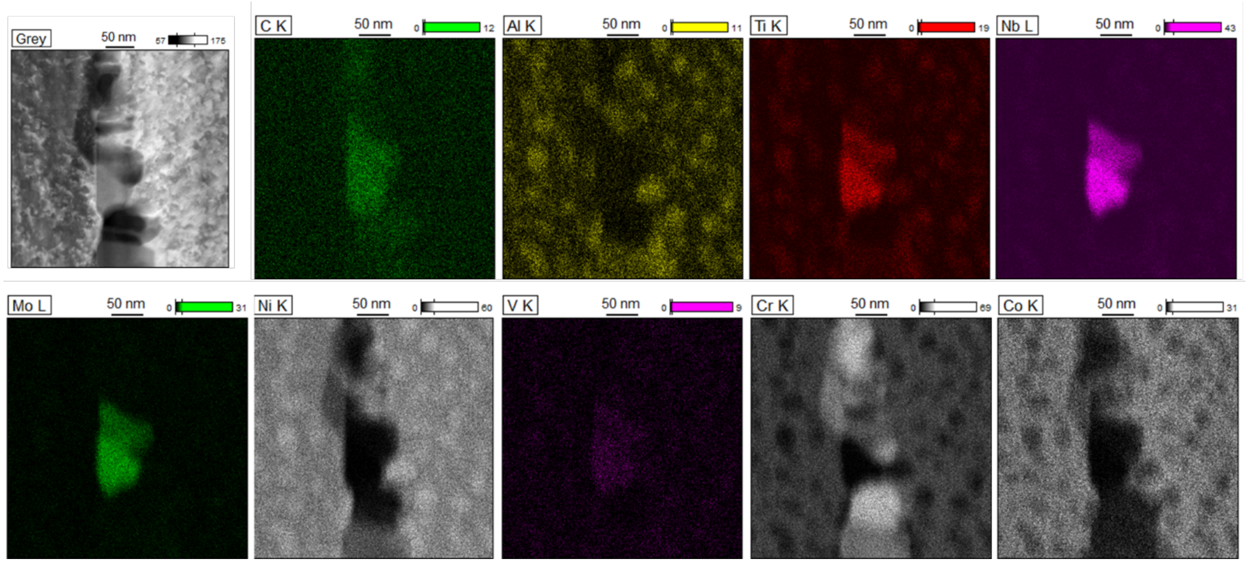

Figure 29: SEM-EDS results showing the intensity maps of different elements at a grain boundary area

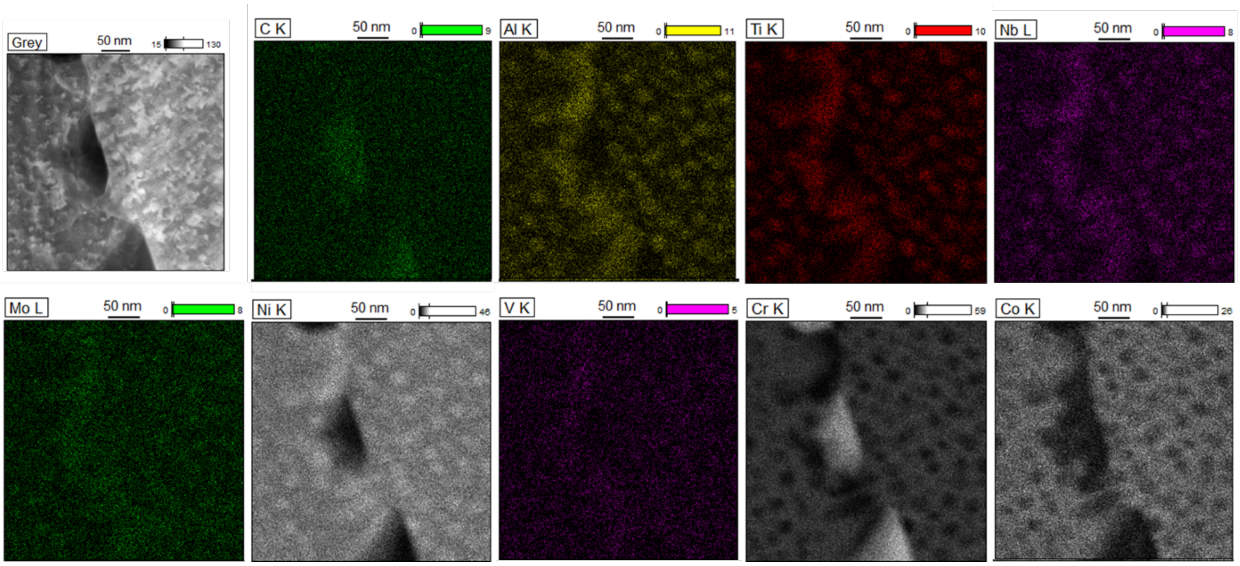

Figure 30: SEM-EDS results showing the intensity maps of different elements at a grain boundary area.

After establishing the baseline characteristics of grain boundary precipitates at boundary regions without PFZs or discontinuous coarsening, a TEM sample was next extracted from the boundary regions of the tube that had exhibited cracking. A region of the grain boundary was identified and is shown in Figure 31a. This site also shown in Figure 31b consisted of a region showing discontinuous coarsening located just ahead of a crack tip. This boundary exhibited coarse and elongated precipitates along with PFZ. Figure 31b shows the trenching operation being conducted using FIB to separate the region of interest from the surrounding matrix and Figure 32 shows SE and BSE SEM images of the extracted TEM sample after the final FIB thinning process. In these images it can be observed that the FIB milled grain boundary starts at the middle of the top portion of the sample but the boundary curves and ends on the side of the sample. In the Figure 32b, regions with cavitation damage at the grain boundary region also be seen.

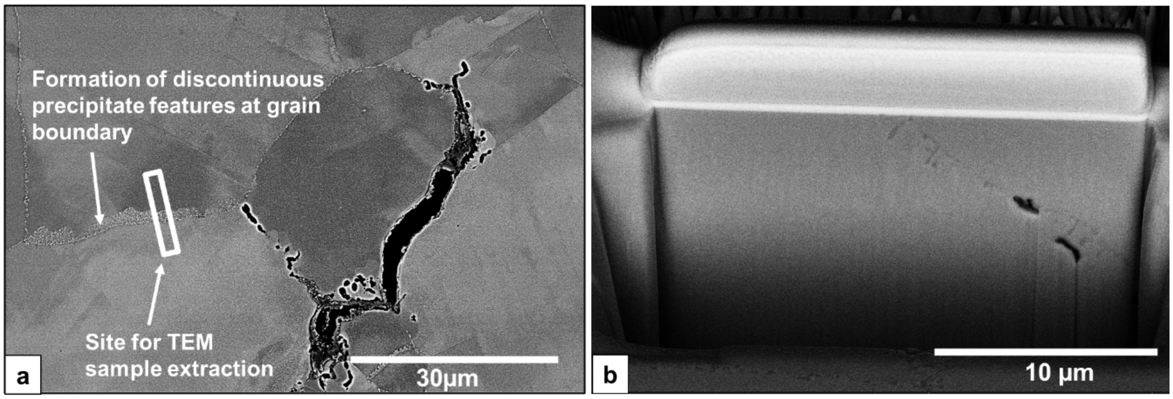

Figure 31: a) BSE image showing the region where the TEM sample was removed and b) trenching operation being performed before the extraction of TEM sample.

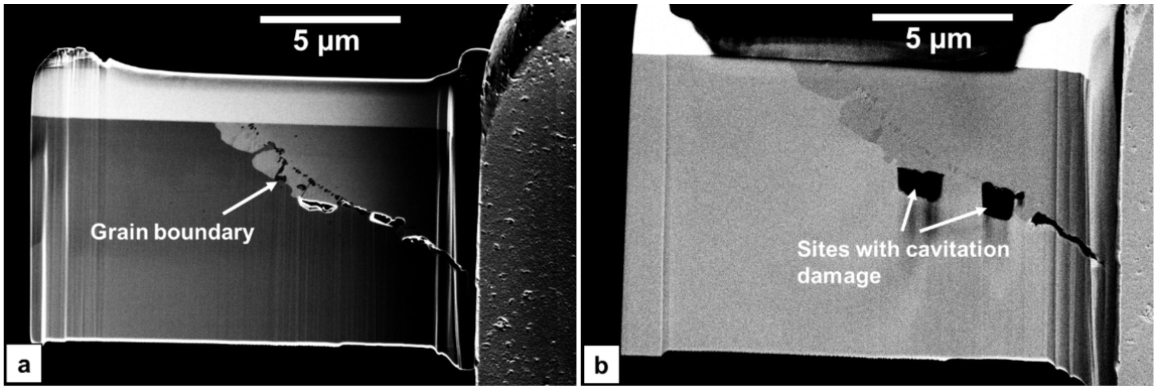

Figure 32: SE and BSE image of the final TEM sample showing grain boundary features and cavitation damage.

Figure 33a shows a BSE image of the extracted sample at a higher magnification and Figure 33b is a schematic created to show the various features of interest in this sample. In the BSE image, there are two main regions which differing grey scale contrast. These two regions are two adjacent grains (labeled Grain 1 and Grain 2) and their color difference is because of the difference electron channeling contrast between the two grains. In the schematic, the two grains in the TEM sample are divided by a solid blue line in the schematic, which is the original grain boundary. The blocky blue features on this boundary are the grain boundary precipitates and the cavitation damage sites are highlighted as black regions. From the grain boundary and growing into Grain 1 are regions that have the same contrast as Grain 2 in Figure 33a. These are PFZs which may also have some elongated precipitates associated with discontinuous coarsening. To establish the characteristics of the grain boundary, multiple EDS line scans were performed to determine the distribution of various alloying elements.

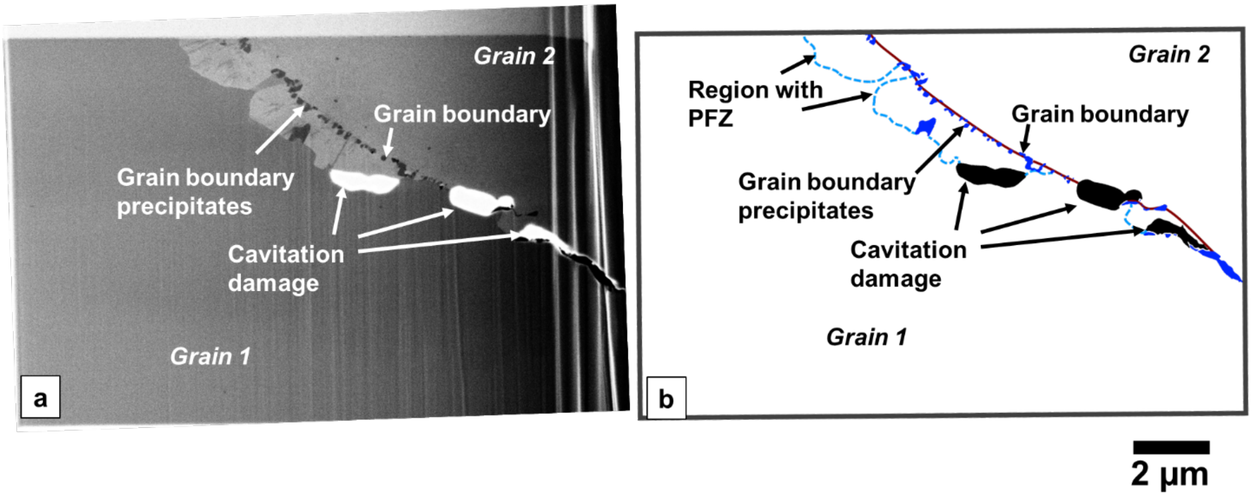

Figure 33: a) BSE image of TEM sample and b) schematic of various features in TEM sample.

Figure 34a shows the region (red rectangle) of the TEM sample that was selected for EDS line scan and the magnified image of this region is shown in Figure 34b. An EDS line scan performed in this area has been highlighted by a yellow line and the line scan starts from inside a region in Grain 1, transitions through a region that is believed to be a PFZ, goes over the precipitates at the original grain boundary and ends at a region inside Grain 2. The variation in the intensity of various alloying elements along this live were plotted in the graphs shown in Figure 34c. At the beginning portion of the scan, where the X-rays signals are being generated from Grain 1 (between the regions 0 to 0.25 µm in the x-axis of graphs), there is variation in the Ni, Al, Ti and Nb. These variations represent the fine γ' precipitates present in the matrix of Grain 1. The region between ~0.25 to ~1.5 µm in the graph corresponds to the region which is believed to the PFZ and in this region there is no change in the relative peak intensities of various alloying elements suggesting that this area is indeed free from any detectable precipitates. As the line scan reaches the grain boundary region (at ~1.5 µm), there is a sharp increase in the intensity of elements Ni, Ti, Al, which corresponds well with a grain boundary γ' precipitate. Upon careful observation of the line scan signal data, there is a further increase in Nb and Mo intensities right adjacent to the γ' particle, perhaps corresponding with a small MX particle present right next to the γ' precipitates. From the region ~1.6 µm to 2.75 µm in the x-axis of the graph, there is a regular increase in peak intensities of elements Ni, Al, Ti and Nb, which is associated with the fine γ' precipitates within the matrix of Grain 2. This analysis confirms that area that is believed to the PZF is indeed free from precipitates and hence a denuded zone. This zone is ~1.25 µm thick at the region of the scan.

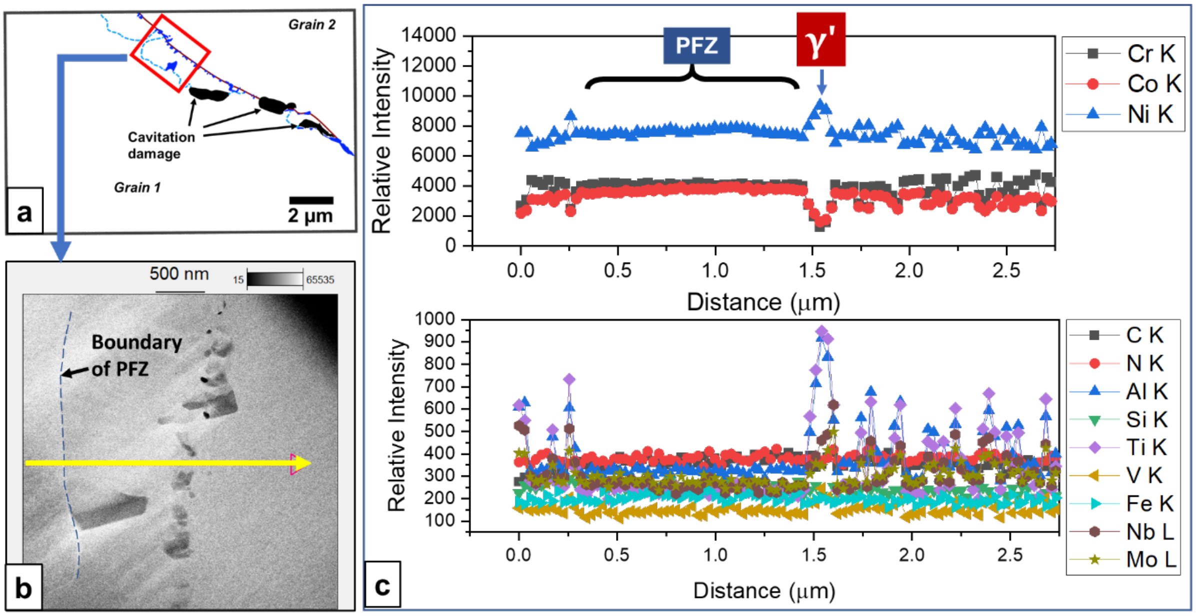

Figure 34: a) Location of line EDS analysis in schematic, b) the region where line EDS was performed and graphs showing distribution of peak intensity of various elements along the line scan.

Similar analysis was performed a second grain boundary region as marked on Figure 35a and the magnified image from this area is shown in Figure 35b. A line scan was performed at this site as indicated in the image Figure 35b, with an intent to understand grain boundary precipitate structure. At the beginning of the scan, there is no relative change in the peak intensities of the different elements as shown in Figure 35c. suggesting that the scan was initiated at a PFZ region. When the electron beam is traversing over the grain boundary precipitates, the obtained elemental intensities are present between ~0.25 µm to ~1.25 µm region of the x-axis. In this region, there appears to be an alternate arrangement of Ni, Ti, Al and Cr, C regions. This suggests that at this grain boundary site has alternate arrangement of γ’ and $M_{23}C_6$ carbides, similar to the precipitate structure seen in the TEM sample from the non-cracked tube of the weld discussed in Figure 30. Results from addition line scans are provided in the Appendix.

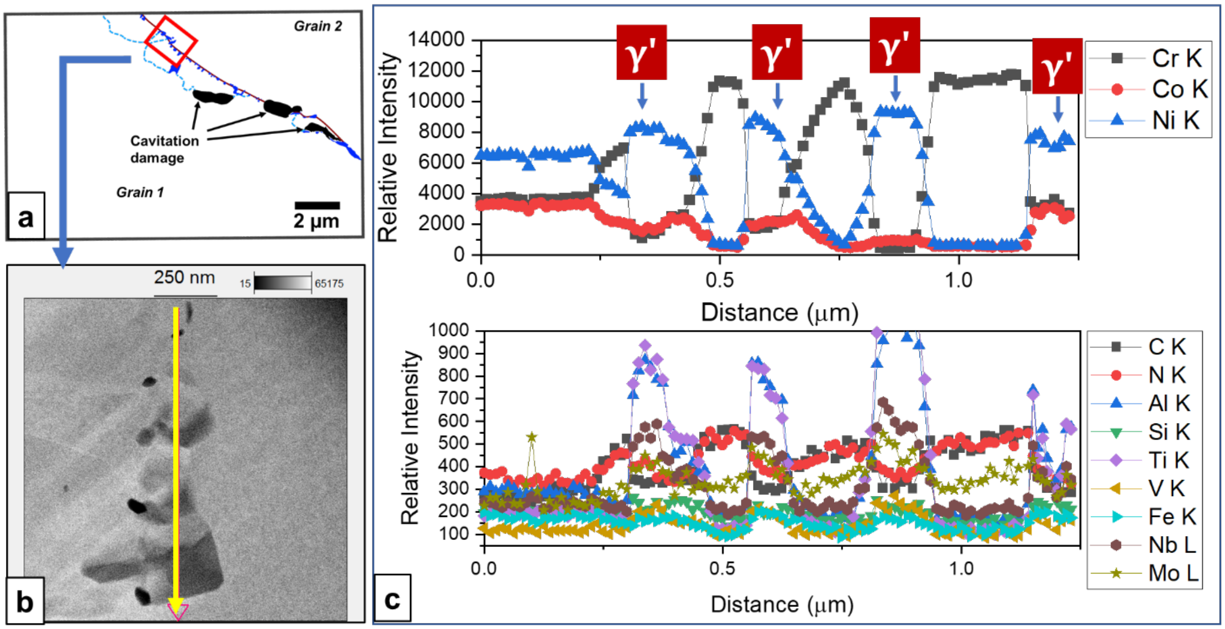

Figure 35: a) Location of line EDS analysis in schematic, b) the region where line EDS was performed and graphs showing distribution of peak intensity of various elements along the line scan.

The TEM EDS discussed above confirmed that the grain boundary regions ahead of the crack tip from the sample Row 14 Weld 25 #1 contains precipitate free zones and discontinuous blocky precipitates consisting of γ' and $M_{23}C_6$ carbides. However, it was not clear whether the zone with discontinuous precipitation is a newly formed region by phenomenon such as recrystallization or whether this is formed by the growth of an existing grain. To determine this, orientation analysis of crystals within these regions were performed using selected area electron diffraction (SAED) technique. Diffraction patterns were obtained from the matrix of different regions of TEM sample and compared. If the area with discontinuous precipitation were to be a new grain, the diffraction pattern obtained along a zone axis from this area would not match the pattern from adjacent grains due to differences in the orientations of the lattice structures of these regions. However, if this zone is formed from the growth of a grain, it would retain the orientation of the parent grain the diffraction pattern from this zone would match the pattern from the parent grain.

Figure 36a shows the schematic of the three regions of interest: Grain 1, Grain 2 and PFZ. These three regions are highlighted in a HAADF image in Figure 36b and diffraction patterns were obtained from four locations of this image: Grain 1, Grain 2, PFZ 1 and PFZ 2. These patterns taken along the [112] zone axis are shown in Figure 37. From this image the diffraction pattern from the matrix of Grain 2 matches the patterns from PFZ1 and PFZ2. This analysis suggested that the zone with the discontinuous precipitates was a region that formed from the growth of Grain 2 and is not a newly formed grain.

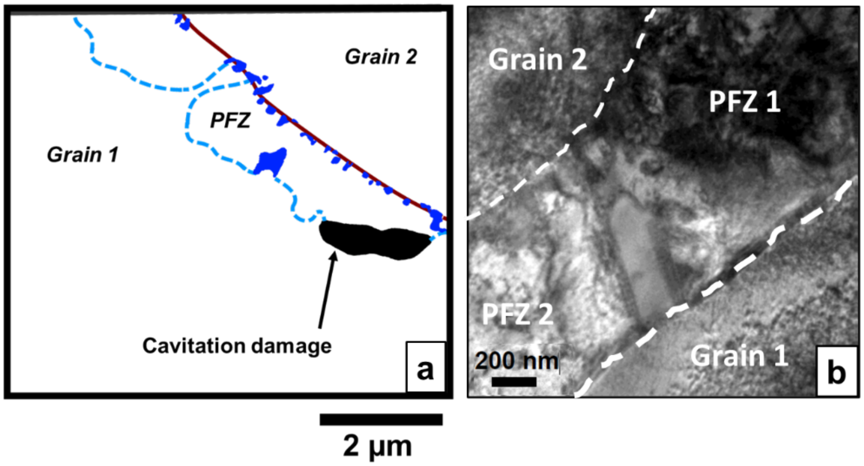

Figure 36: a) Schematic showing different regions in TEM sample and b) high magnification HAADF image showing three regions from where SAED patterns were obtained.

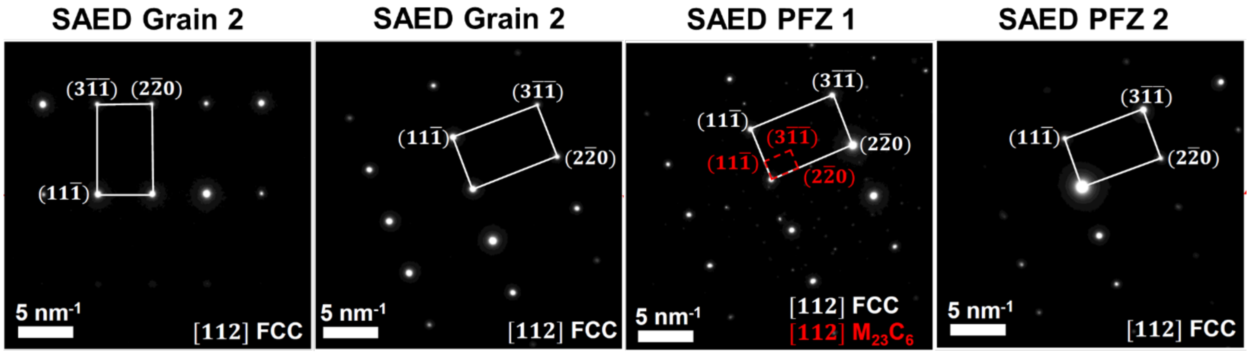
SAED Grain 2

SAED Grain 2

SAED PFZ 1

SAED PFZ 2

Figure 37: SAED patterns obtained from different regions of the TEM sample shown in Figure 36.

Summary of finding from analysis of 740H tube-to-tube weld samples from Demonstration Project #1

- Among the many different welds between 740H components in Demonstration Project #1, cracking issues were observed only in tube-to-tube girth welds and that too in only a small percentage (~3%) of these welds [12].
- All dispositioned welds were found to have variable workmanship with excessive ID push-through and/ or OD reinforcement.
- Cracking in the studied tubes was consistently observed ~1/3 of the circumference on the tube IDs and intermittently on the ODs.
- All the studied cracks initiated at the ID and primarily at or near the weld toes, but had variable propagation characteristics, with some cracks propagating along HAZ and transitioning into weld metal and, in some cases, spiraling away from weld into base material.

- In all the thin-wall tube-to-tube welds, cracking was found to be on the thicker side of the weldment.
- There was no clear association of cracking behavior with differences in grain size.
- Isolated cavitation damage was observed on boundaries ahead of crack and adjacent to the main crack.
- Oxide scale formation was noted in the crack and near the crack tips.
- Formation of small equiaxed grain at the weld toes suggest grain recrystallization, suggesting presence of a strained matrix near weld toe.
- Formation of coarse precipitates accompanied grain boundary denuded zones and these coarse precipitates were either elongated and growing into a grain or blocky in morphology. In both instances the precipitates formation was discontinuous on the grain boundary.
- At regions away from the site with crack propagation, the grain boundaries had continuous coverage consisting of $M_{23}C_6$ carbides and γ' precipitates.
- STEM-EDS analysis of grain boundaries confirms complete coverage of grain boundaries with precipitates and no PFZ zone formation.
- TEM analysis also confirms PFZ formation at regions ahead of crack tips at grain boundaries with discontinuous precipitation.
- These PFZ regions were found to have been formed from the growth of one grain into a neighboring grain.

Characterization studies on 740H weld samples from Demonstration Project #2

Background

Demonstration Project #2 is a pilot thermochemical energy storage (TCES) reactor that integrates with a closed sCO_2 Brayton power cycles for heat recovery. The assembly of this plant includes a high temperature heater that are interconnected to TCES reactor using a spool fabricated from a 740H alloy tubing. This spool was designed to have an instrumentation tee that would enable measurements of temperature and pressure between the high temperature heater and the TCES reactor. Figure 38a shows a schematic of the interconnecting tube and instrumentation tee and an image of this tee in the pilot test facility is shown in Figure 38b. The tee was fabricated with a rectangular body from a larger 740H forging. Channels were machined into this body and connected to 740H tubing using socket welds. In total there was three socket welds made on this component. These welds passed NDE inspections after the welding process and were subsequently subjected to PWHT and were installed in the system.

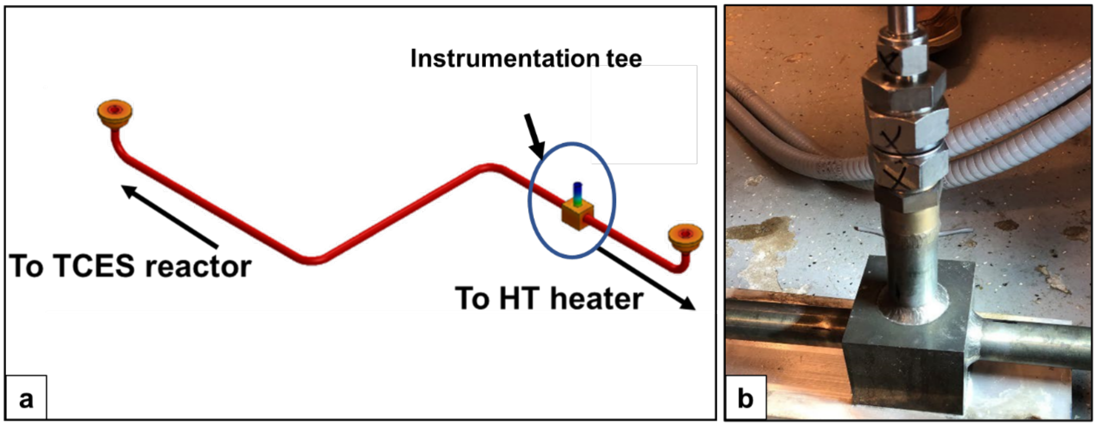

Figure 38: a) Schematic of the 740H interconnect spool showing the location of an instrumentation tee and b) an image of the instrumentation tee at the test facility.

During the operation of the system at a pressure of ~200 psi, multiple audible leaks were noted from this instrumented tee block. In-situ LP testing revealed external surface breaking cracks in all the three socket welds. Figure 39 shows the appearance of these welds after in-situ LPT testing at the test facility. This leaked tee was provided to EPRI for analysis of the weld cracks and was included in the field failure analysis program of this project.

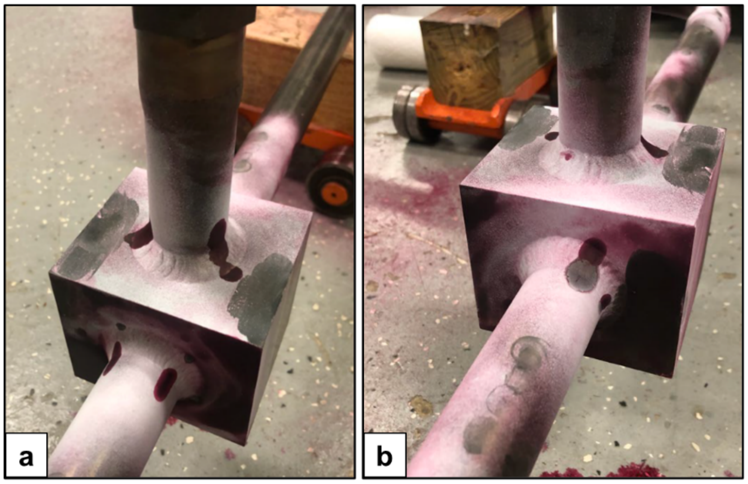

Figure 39: Images showing the 740H instrumentation tee block after in-situ LP testing at test facility.

Experimental procedure & results for failure investigation

NDE and Sectioning for metallography

The provided component had three nozzles with portions of 740H tubes still attached to the 740H forged block. Figure 40 shows an as-received images of the component. The sides of the component were labeled as ‘Front’ and ‘Rear’ as shown in the image and the three nozzles were designated as ‘Nozzle A’, ‘Nozzle B’ and ‘Nozzle C’ as marked in the figure.

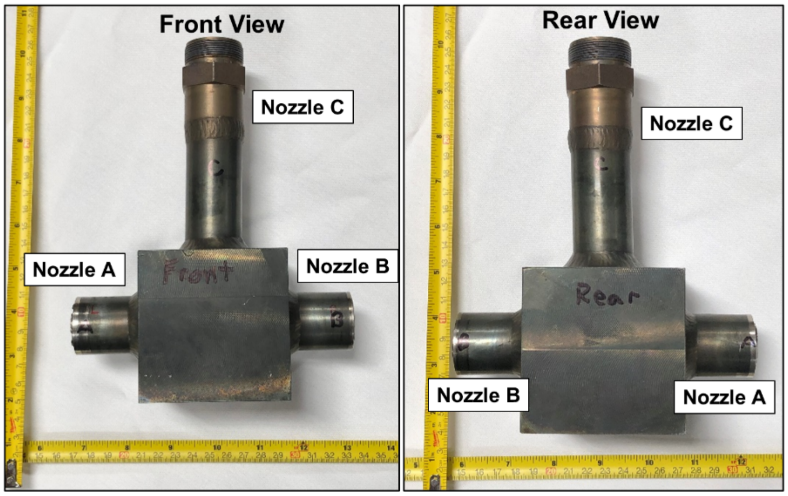

Figure 40: Images showing the 740H instrumentation tee block in the as-received state.

Visual inspection of the provided welds showed clear surface breaking cracks and the observed cracks were documented in a schematic shown in Figure 41. The weld on Nozzle A is found to have 7 through-wall cracks, one on Nozzle B had 5 cracks and the one on Nozzle C had 3 cracks.

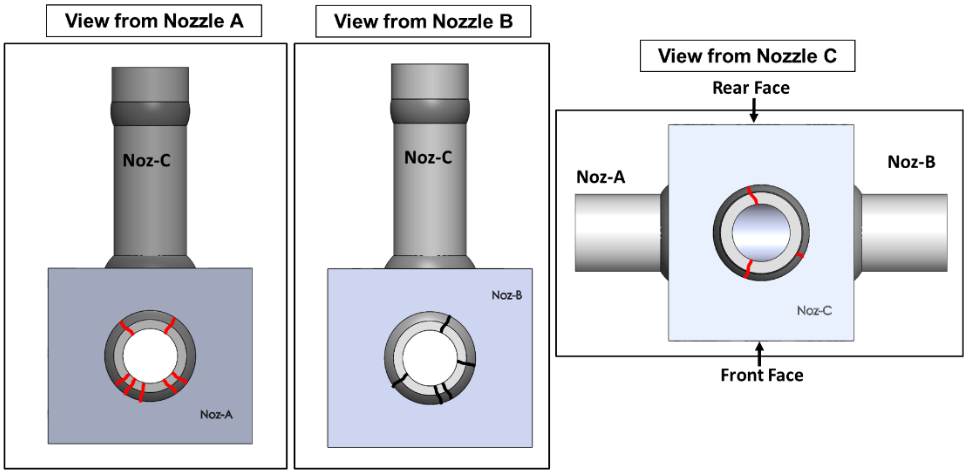

Figure 41: Schematic showing the number and locations of various cracks detected in the instrumented tee.

The instrumentation tee block was then sectioned through a plane running through the centers of the three nozzles as shown in Figure 42a and the interiors of the two obtained sections are shown in Figure 42b and Figure 42c. LP testing of the interior surfaces showed multiple interior cracks. Subsequent to LP testing the blocks were machined for metallographic preparation and small sections of the nozzles and the 740H forged block were cut for complete composition analysis.

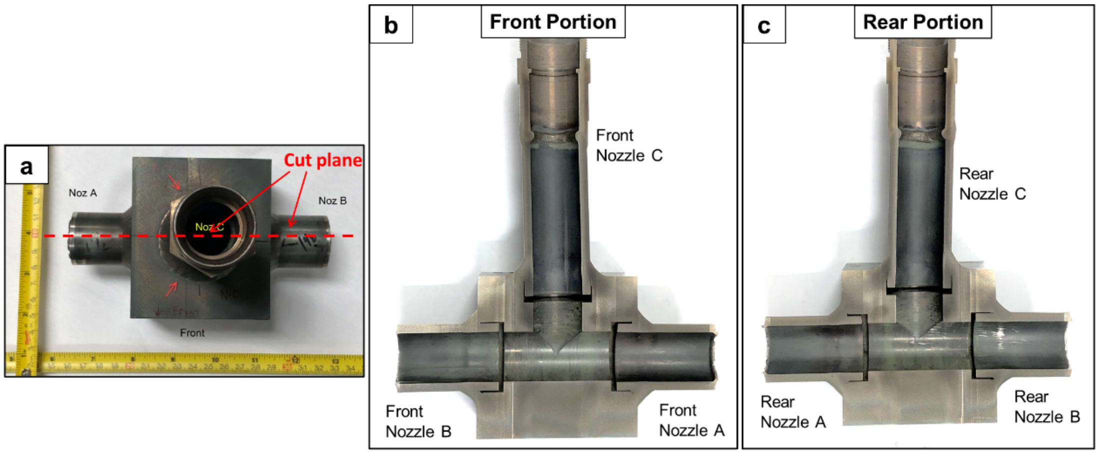

Figure 42: a) Sectioning scheme of the instrumentation tee and b), c) the resulting two sectioned pieces of the tee block.

The Front portion of the tee was chosen for metallographic studies and Figure 43 shows the sectioning scheme for obtaining sample sections for metallographic analysis.

Samples were obtained from Nozzle A and Nozzle B and each of these nozzles were sectioned into 5 and 4 pieces respectively. The sectioned samples were numbered 1 to 5 (or 1 to 4 in Nozzle B) such that the larger numbered sections were closest to the forged block. The intention behind obtaining such successive sections was to determine the growth characteristics of these cracks.

Front Section of the Tee piece

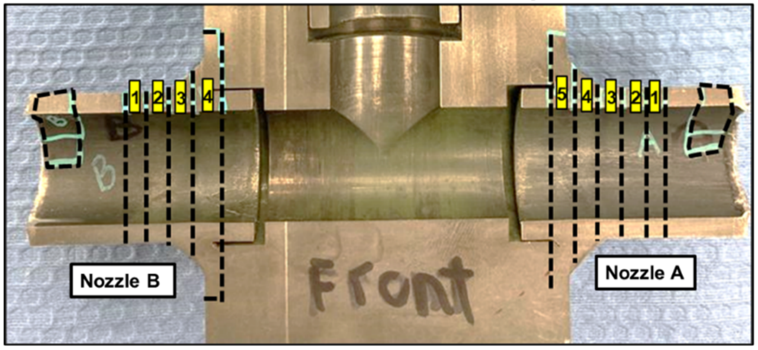

Figure 43: Image showing sectioning scheme for metallography

Macro-scale Imaging and Characterization

Table 7 shows the composition of the 740H forged block and that of the three nozzles that were welded to it. All the tested material conformed with the composition requirements for the material UNS N07740.

Table 7: Table showing the compositions of the different components studied

Element	**Cr**	**Co**	**Al**	**Ti**	**Nb**	**Fe**	**C**	**Mn**	**Mo**
UNS N07740	23.5-25.5	15.0-22.0	1.35-2.00	0.5-2.5	0.5-2.5	0-3.0	0.005-0.008	0-1.0	0-2.0
Nozzle A	24.323	20.004	1.343	1.454	1.506	0.3	0.038	0.24	0.5
Nozzle B	24.387	19.918	1.36	1.466	1.515	0.3	0.036	0.24	0.5
Nozzle C	24.401	19.959	1.373	1.468	1.518	0.3	0.034	0.24	0.5
Body	24.613	19.872	1.389	1.408	1.537	0.29	0.03	0.28	0.49
Element	**Si**	**Cu**	**P**	**S**	**B**	**Ca**	**La**	**Ta**	**V**
UNS N07740	0-1.0	0-0.5	0-0.03	0-0.03	0.0006-0.006	-	-	-	-
Nozzle A	0.138	0.012	<0.002	<0.0005	0.0022	<0.002	<0.002	<0.005	0.005
Nozzle B	0.16	0.01	<0.002	<0.0005	0.0021	<0.002	<0.002	<0.005	0.005
Nozzle C	0.14	0.01	<0.002	<0.0005	0.0016	<0.002	<0.002	<0.005	0.005
Body	0.162	<0.002	<0.002	<0.0005	0.0019	0.005	<0.002	0.006	0.006
Element	**W**	**Zr**	**As**	**Mg**	**Pb**	**Sb**	**Se**	**O**	**N**
UNS N07740	-	-	-	-	-	-	-	-	-
Nozzle A	0.005	0.022	0.002	0.0044	0.00007	<0.0001	<0.0008	0.0009	0.0066
Nozzle B	0.005	0.022	0.002	0.0042	0.00007	<0.0001	<0.0008	0.0003	0.0066
Nozzle C	0.004	0.023	0.002	0.0045	0.00006	<0.0001	<0.0008	0.0004	0.0069
Body	<0.002	0.035	0.003	0.0053	0.00006	<0.0001	<0.0008	0.0002	0.0057

Macro images of the etched cross sections from Nozzle A (labeled A1 to A5) are shown in Figure 44. The section A5 was through both the forged body and tube and the forged body is evident in the outside of the tube cross-section. In this section, some portions of the toes of the fillet welds were also evident. Section A4 was through the fillet weld and the tube and the weld portion of the sectioning area is evident from a wavy nature of the outer diameter of the cross section. Sections A3 through A5 were all through the tube body only, although in A3, small portions of the fillet weld toes were still evident.

From the etched image of section A5, both the tube and forged body show equiaxed grain structure. Also in this section, multiple cracks both in the body of the tube and in the forged body are evident. Most importantly, the cracks in the forged body were radial with respect to the center of the tube. There were radial through-wall cracks through the tube body too but evidence of multiple cracks within the body of the tube but forming immediately below the toe of the welds were also evident in this cross-section. Figure 45 shows magnified macro images of some of the cracks observed in the cross section A-5. Figure 45a is an image with representative cracks observed in the tube body showing both radial cracks and cracks formed below weld toes. Both these types of cracks were intergranular in formation.

Figure 45b was an image from the forged body and shows a radial crack in this body. Clearly the crack in this case is also intergranular and the radial nature of cracking in both the tube body and in the forged body points to factors contributing to significant stress in the hoop direction of the tube such weld constraint and residual stresses developed during events that cause thermal expansion/ contraction. In comparison, the cracks developed immediately below the weld toe are generated due to local residual stresses developed at the toe of the welds. Finally, Figure 45c shows one example of a crack in the weld which seems to have originated from a notch in the weld profile.

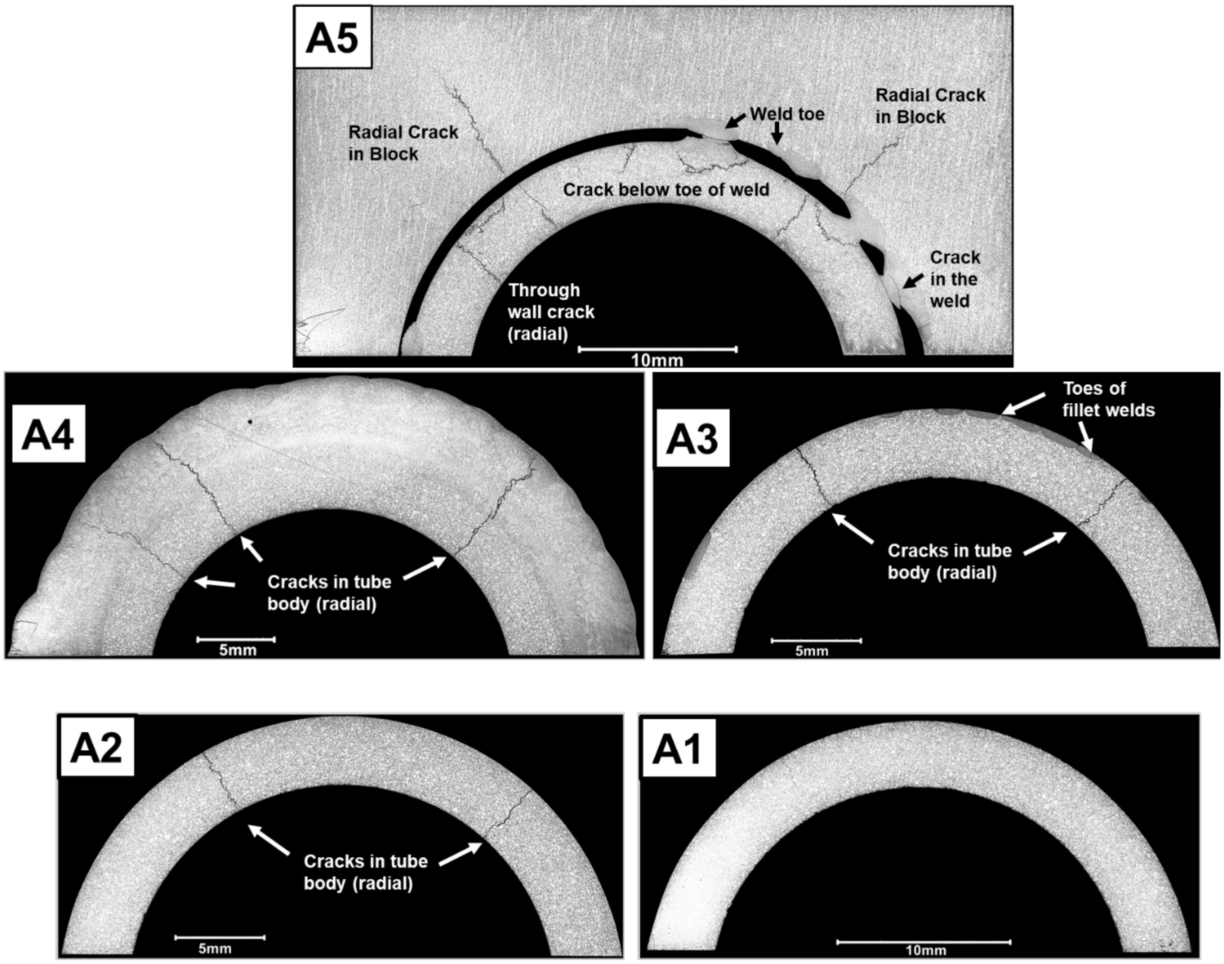

Figure 44: Macro images of the 5 cross-sections from Nozzle A.

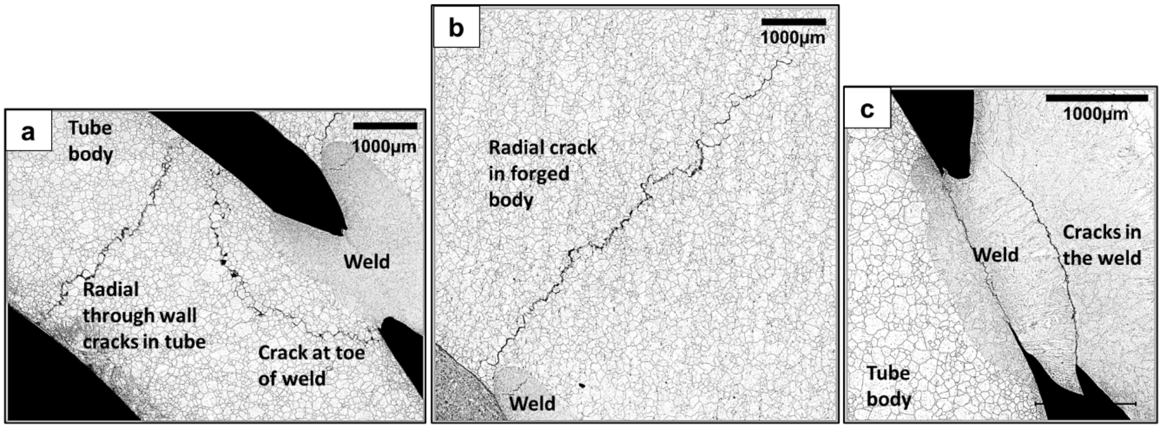

Figure 45: Select images of cracks see in the section A5 which show a) cracking in the tube, b) cracking in the forged body and c) cracking in the fillet welds.

Figure 46 is a magnified image of one of the radial cracks in the sample cross-section A4. This image has a portion of the fillet weld on the left of the image and the tube body on the right of the image separated by the marked weld fusion line. There is a radial crack traversing through the body of the tube and transitioning into the weld. Once again, the crack clearly appears to be intergranular within the tube body and continued to have grown in an intergranular manner.

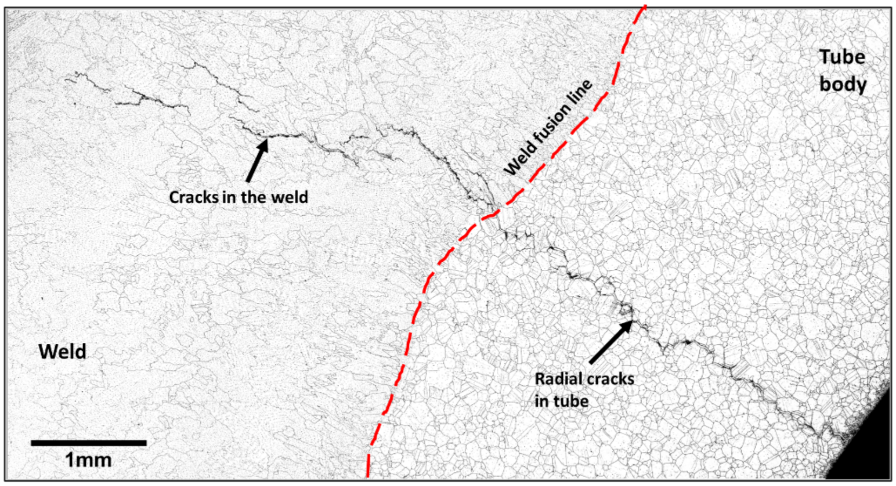

Figure 46: Image of a radial crack from the section A4

Based on the macro analysis of multiple cross sections, the cracks formed in the body of the tube or in the forged body are all intergranular in nature as was seen in the cracked samples from Demonstration Project #1. Furthermore, similar to the samples in Demonstration Project #1, most of the cracks formed were sharp and have minimal branching or were surrounded by secondary cracks. However, in these samples, it was difficult to determine the origination site of these sites. Since the fillet weld in this case were on the OD of the tubes, it is possible that the origin of the cracks may have been at the weld toe of the tube OD region. However, to explain the intergranular nature of crack propagation, micro-scale characterization of the microstructure would be required.

Micro-scale Imaging and Characterization

The grain boundary microstructure in the cross-sections were studied at the micro-scale at select locations using an SEM. Investigations involved analysis of grain boundary features ahead of the crack tips to explain the intergranular nature of cracking. Figure 47 shows a series of low magnification images of crack tips located at various locations of studied cross sections on left column and higher magnification images of the grain boundary regions ahead of the crack tip is shown in the right column from regions as highlighted in each of the lower magnification images.

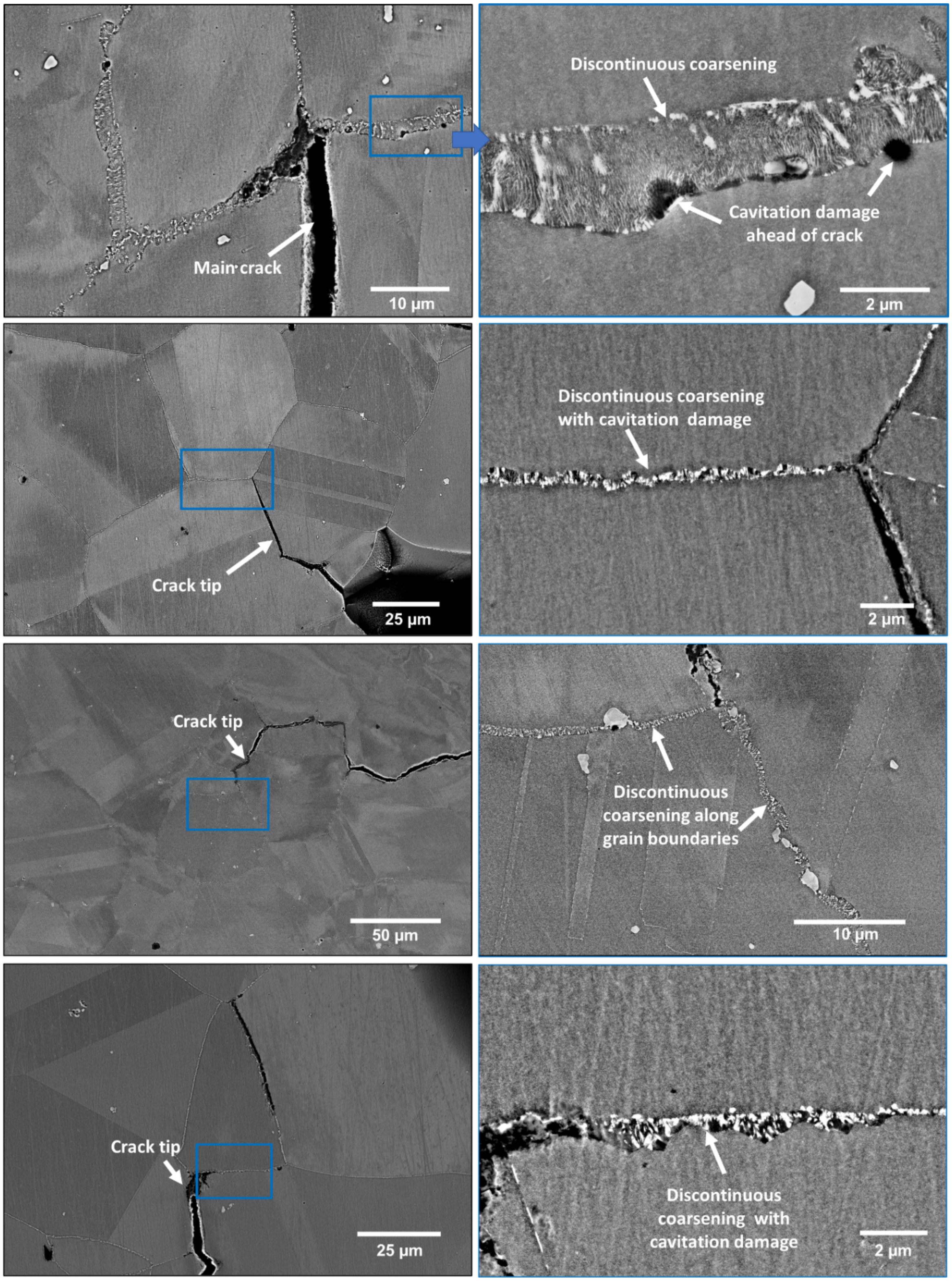

Figure 47: Lower magnification images (left column) of different crack tips from various cross sections and corresponding higher magnification images showing discontinuous precipitation at grain boundaries

Each of these higher magnification images show a common occurrence. Ahead of each of the shown crack tips, the grain boundary exhibits evidence of discontinuous coarsening in the form of elongated finger shaped precipitate features growing away from the main grain boundary. The formation of these features is typically accompanied by region devoid of precipitates, which are known as precipitate free zones or denuded zones. As seen in the results from Demonstration Project #1, these regions can exhibit cavitation damage during SRxC. In many instances in the analysis of cracked samples from this component, the formation of discontinuous coarsening was documented. The presence of such grain boundary structures could make the material more susceptible to SRxC. Furthermore, the cracks in these studied cross-sections also showed the presence of oxide scales once more suggesting that these cracks may have formed during the early stages of PWHT operation. Most observations of discontinuous coarsening were made at or near of tube OD regions but the formation of such grain boundary features become less prominent at the mid-wall and ID regions of the tubes.

Summary of observations from analysis of cracks in Demonstration Project #2

- Nondestructive examinations showed multiple through wall cracks at the three socket welds and all cracks were found to be running along the tube axis
- Analysis of macro-cross sections showed multiple crack morphologies at the inner toe of the socket weld. These include:
    - Cracks in the weld
    - Cracks forming the weld HAZ and following the shape of the weld
    - Radial cracks in the forged body
    - Through-wall cracks in the tubes
- Cracks formed were sharp with minimal branching.
- There was very little indication of damage adjacent to the grains surrounding the cracks.
- The formation of oxide scales was noted on the inner surfaces of the cracks.
- From metallurgical analysis, cracks appear to be forming at the weld and tube interface and propagating into the weld and tube body, however, it is difficult to find initiation sites
- Weld regions near crack show evidence of strain in the matrix and formation of grain boundary features with discontinuous coarsening and precipitate denuded zones. Cavitation damage appears to initiate at these denuded zones.
- The OD regions of the tube and cracked regions within tube body also showed formation of discontinuous coarsening and formations of denuded zones ahead of the cracks and at grain boundaries near cracks.
- Although the grain boundary regions near the welds show formation of discontinuous coarsening and precipitate denuded zones, these formations are not obvious and become less prominent farther away from the weld
- The radial morphology of the cracks in both the tube and the forged body, the sharp/ localized nature of the crack and crack growth along the length of the tube

suggests that the stress state could be playing a major role in the formation of these cracks.

Characterization studies on 740H weld samples from Demonstration Project #3

Background

Demonstration Project #3 is another advanced powercycle demonstration project that utilizes supercritical CO_2 in a direct-fired cycle for power generation. The turbine exhaust piping used in this plant is made from alloy 740H material and several samples of pipe-to-pipe girth welds were provided to EPRI for the evaluation of welds. The plant removed these welds during field welding when dye penetrate examination identified numerous indications. The plant modified its welder training practices and procedures and successfully executed 21 welds of similar dimension which, at the time of reporting, had been in operation for a test campaign. All the received pipes had a 12 in. nominal outer diameter but the wall thicknesses of the pipes varied and are show be in Table 8. Figure 48 shows the four pipes that were provided to EPRI.

Table 8: Table showing the nominal dimensions of the four pipes received as a part of Demonstration Project #3.

Component	Outer diameter (in.)	Wall thickness(in.)	Notes
Pipe A	12	0.287	
Pipe B	12	0.285	WT on other side of weld was 0.257
Pipe C	12	0.306	WT on other side of weld was 0.366
Pipe D	12	0.242	

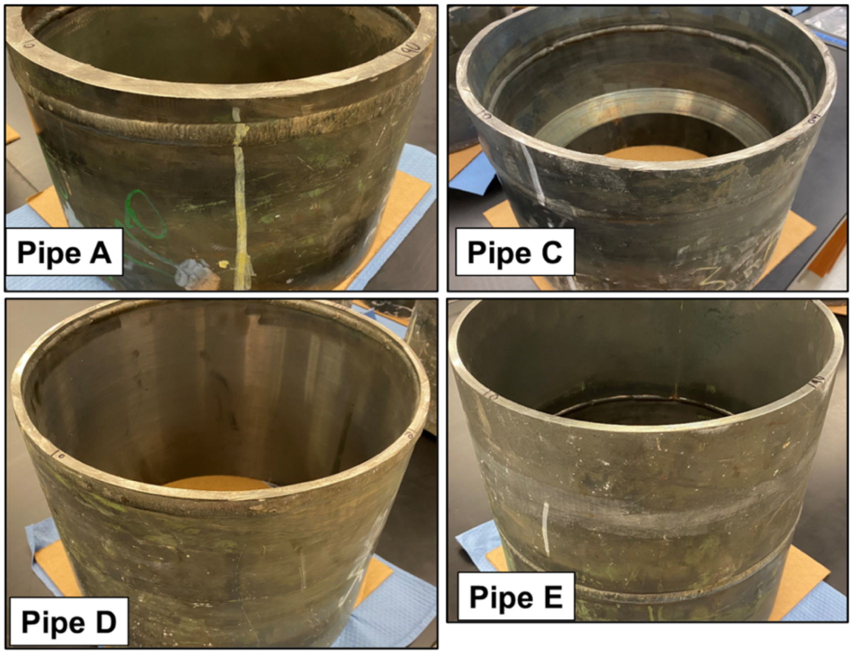

Figure 48: As-received images of the four pipe sections from Demonstration Project #3

Experimental procedure & results for failure investigation

NDE and Sectioning for metallography

NDE investigations using liquid penetrate (LP) testing were carried out on the provided pipe welds and testing was focused on the ID regions of the weld. After LP testing it was found that among the provide pipes, Pipe C showed clear indications of surface breaking discontinuities and only one such indication was found in Pipe D. Pipes A and B did not show any clear indications. Figure 49 shows images of identified areas of discontinuities from the LP testing on Pipe C. At least 10 indications were clearly identified to be cracks oriented in the axial direction (along the pipe axis or length) and a few other indications were attributed to be weld defects. Most of the identified weld axial cracks were on one side of the weld and on the pipe with wall thickness of 0.306 inches. The length of the cracks ranged from ~2 mm to ~6 mm in length on the pipe.

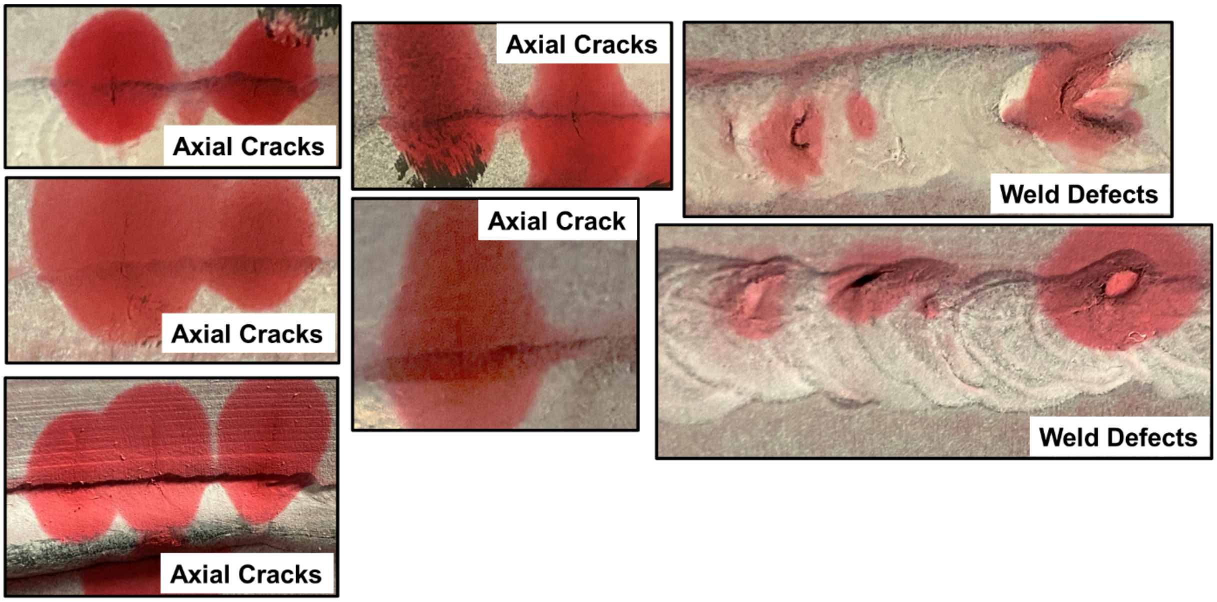

Figure 49: Results from LP testing of Pipe C showing axial cracks and weld defects

A few samples were sectioned from weld on Pipe C using the NDE indications as reference and Figure 50 shows the sectioning scheme as marked on the sample. Multiple sections were taken for metallographic investigation and sections were also taken from the pipe for composition analysis.

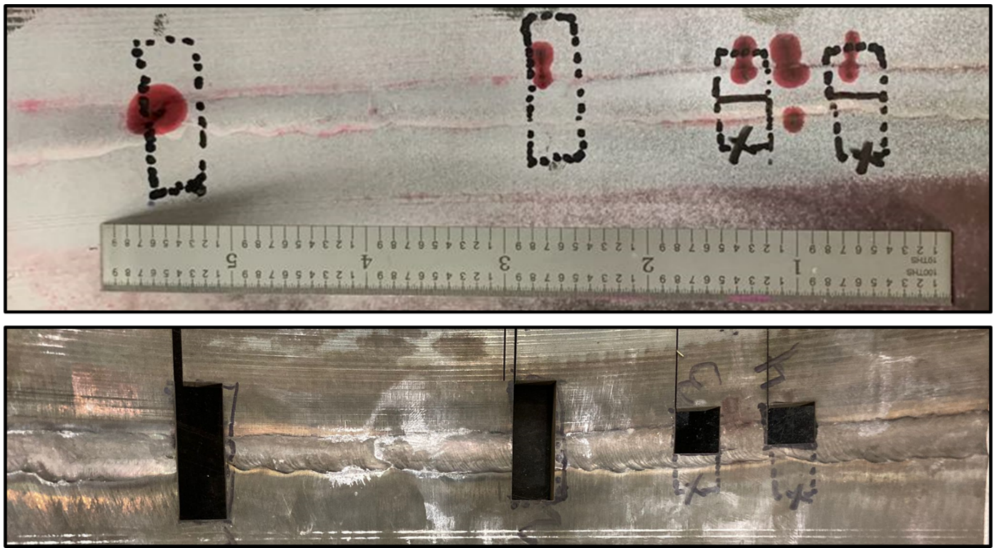

Figure 50: Marking for the sectioning of the LP indications for metallurgical analysis

Among the sectioned samples, one was taken from a region that appeared to be a weld defect and three samples were taken from distinct axial cracks. Two of the samples from the axial cracks were sectioned through the axial cracks to obtained polishing surfaces that were perpendicular to the crack growth direction.

Macro-scale Imaging and Characterization

The composition of the two pipes that were welded in Pipe C are shown in Table 9. From the vales in the table, both pipes conform with the composition requirements for the material UNS N07740.

Table 9: Table showing the compositions of the pipe studied

Element	**Cr**	**Co**	**Al**	**Ti**	**Nb**	**Fe**	**C**	**Mn**	**Mo**
UNS N07740	23.5-25.5	15.0-22.0	1.35-2.00	0.5-2.5	0.5-2.5	0-3.0	0.005-0.008	0-1.0	0-2.0
Pipe C	24.402	20.495	1.454	1.482	1.462	0.14	0.033	0.25	0.53
Pipe C	24.456	20.209	1.462	1.497	1.465	0.14	0.032	0.24	0.52
Element	**Si**	**Cu**	**P**	**S**	**B**	**Ca**	**La**	**Ta**	**V**
UNS N07740	0-1.0	0-0.5	0-0.03	0-0.03	0.0006-0.006	-	-	-	-
Pipe C	0.113	0.006	<0.002	0.0005	0.0016	<0.0005	<0.002	<0.005	0.007
Pipe C	0.136	0.005	<0.002	0.0005	0.0016	<0.0005	<0.002	<0.005	0.008
Element	**W**	**Zr**	**As**	**Mg**	**Pb**	**Sb**	**Se**	**O**	**N**
UNS N07740	-	-	-	-	-	-	-	-	-
Pipe C	<0.005	0.022	<0.002	0.0012	<0.00002	<0.0001	<0.0005	0.0002	0.0046
Pipe C	<0.005	0.022	<0.002	0.0011	<0.00002	<0.0001	<0.0005	0.0001	0.0048

Figure 51 shows the two macro images of the etched surfaces of the samples which were sectioned through the axial cracks. In these images, the growth direction of the cracks is out of viewing plane. Furthermore, from the way these samples were sectioned, a portion of the girth weld close to the OD regions of the weld were retained as marked in the macro images. The sectioning plan to obtain such images is highlighted in the schematic on the right of Figure 51 using a blue dotted line. What is evident from these images is that microstructure of the pipe consists of equiaxed grains and that the cracks formed are once again intergranular. The origin of the cracks, which were most likely located near the ID toe of the weld, is not captured in these cross sections. It is also evident that at these sections, the cracks extend into the weld metal region and are ~ 90% of the way through the section thickness and do not appear to stop at the weld fusion boundary. Similar to the observations from the samples evaluated in the previous two demonstration projects, the cracks formed are sharp with minimal branching or significant amount of secondary cracks surrounding the main crack.

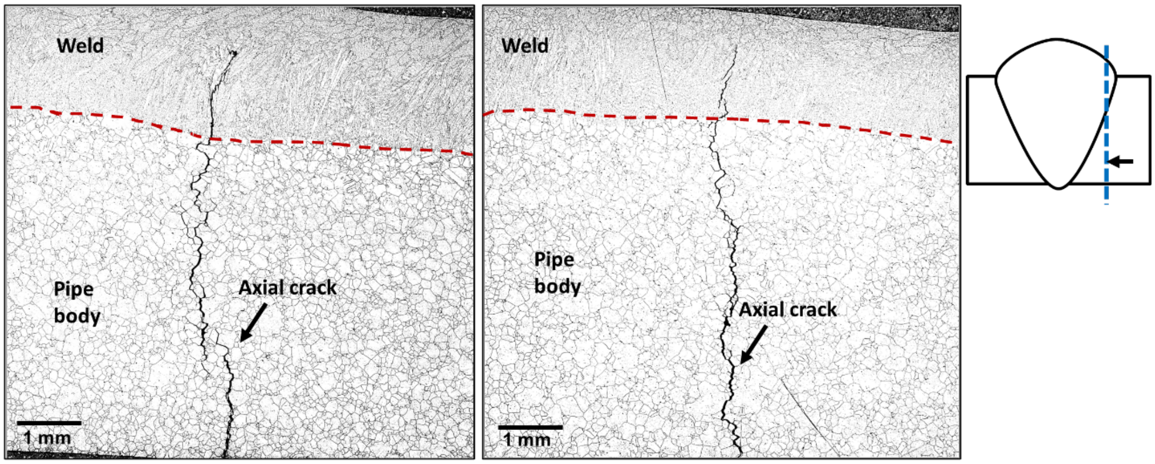

Figure 51: Macro image of cross-sections of two axial cracks. Schematic on the right shows the sectioning plane of the sample with respect to the weld.

To further study the intergranular nature of this crack, micro-scale characterization studies were performed using an SEM. The structure of grain boundaries near the main crack and, in some instances, ahead of the crack tips of any secondary cracks, were documented.

Micro-scale Imaging and Characterization

The etched microstructure of the pipe was studied at locations near the crack and any salient observations made were recorded. Some of the important findings have been shown in various figures below. Figure 52a shows a SE image of a main crack that is propagation in an intergranular fashion along grain boundaries. Some minor amount of branching is observed and the grain boundary features ahead of one such branched crack is shown in Figure 52b and the location of this imaged area is highlighted in

Figure 52a. In can be seen in Figure 52b that the tip of the crack has stopped at a triple point and on one side of the crack is a boundary that exhibits discontinuous coarsening, whereas the other boundary appears to be a normal boundary with a nearly 100% grain boundary coverage by precipitates and no clear indications of discontinuous precipitation or denuded zone formation. The presence of what appears to be an oxide scale is also evident within this crack. The formation of discontinuous precipitates in the adjacent grain boundary is further emphasized in Figure 53 with a higher magnification image of this grain boundary formation. What is immediately evident is that the region with discontinuous coarsening also has formations of PFZs.

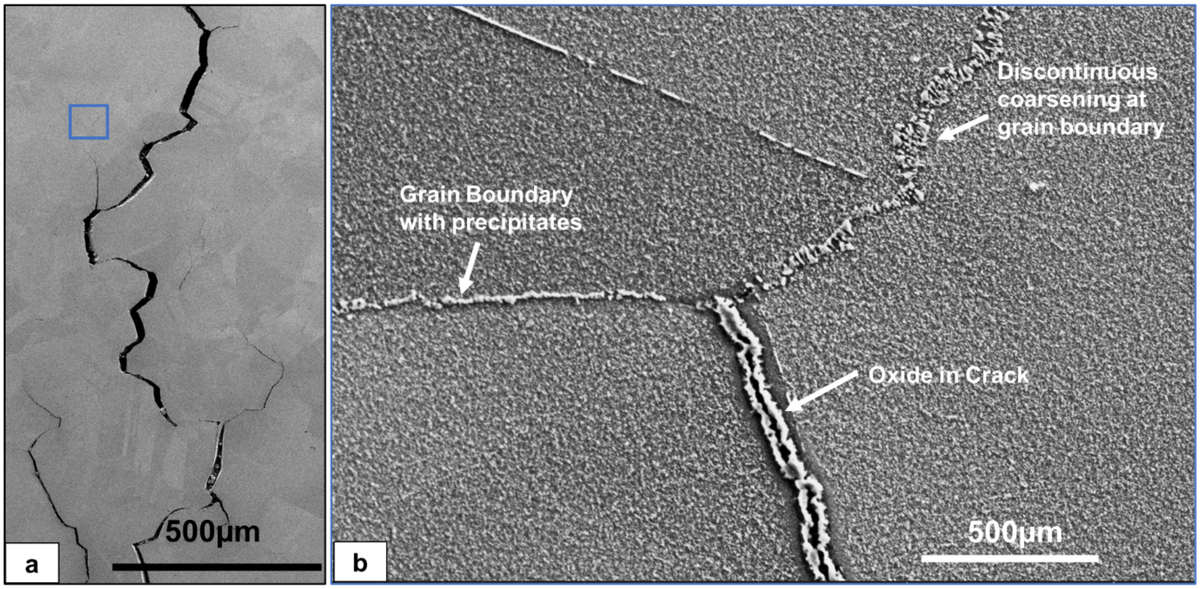

Figure 52: a) Low magnification BSE image showing a portion of the intergranular crack and high magnification BSE image (right) show the grain boundary structure ahead of a secondary crack in Figure 52a.

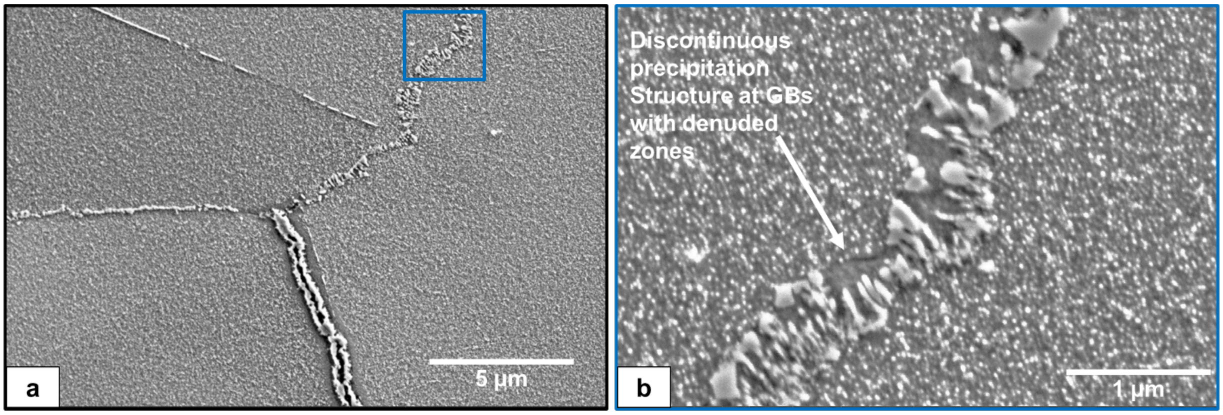

Figure 53: a) Image from Figure 52b marked with a location on a grain boundary and b) higher magnification image of the grain boundary at the marked location in Figure 53a.

Figure 54 shows other similar examples of grain boundary structures ahead of the crack tip where there is clear evidence of discontinuous coarsening and cavitation damage at grain boundary regions ahead of the crack tips.

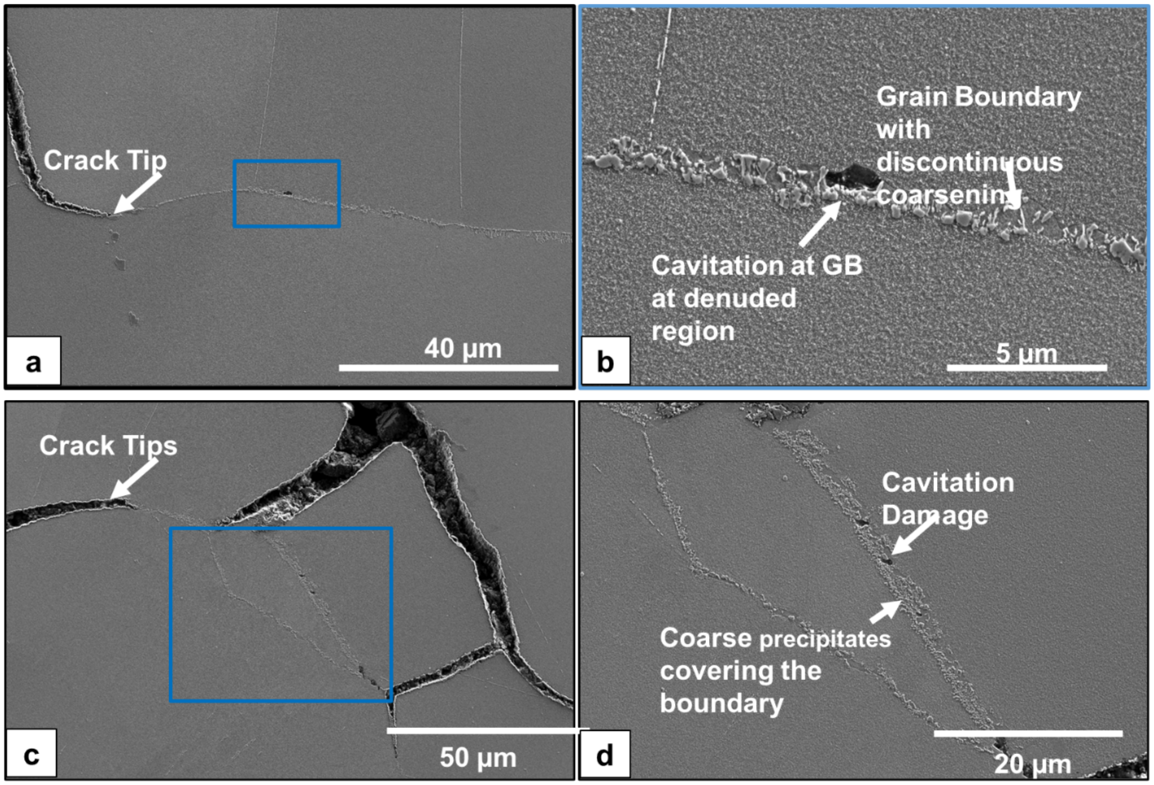

Figure 54: Low magnification (left column) and high magnification (right column) images showing instances of discontinuous coarsening and cavitation damage.

A few grains away from the main branch of the crack however, the grain boundary features do not show any evidence of discontinuous coarsening. An example to highlight this observation is shown in Figure 55 where two grain boundaries removed from the main crack and their precipitation characteristics are shown.

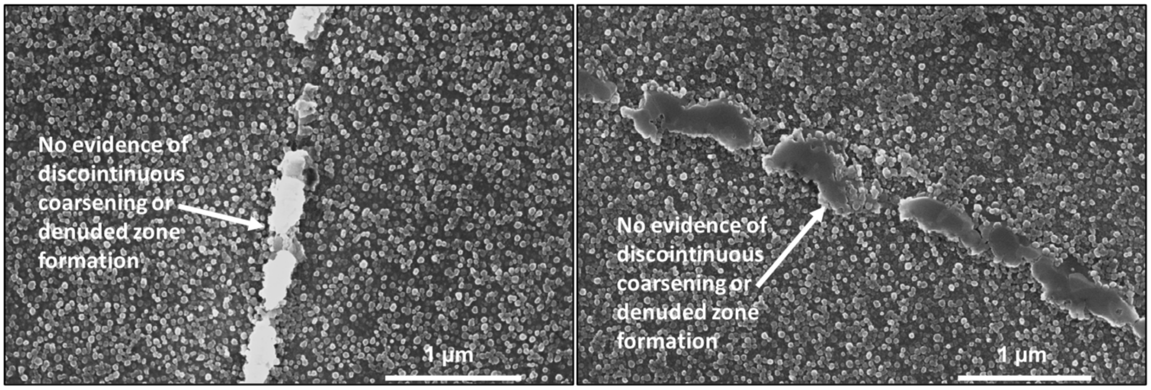

Figure 55: Appearance of grain boundaries away from the cracked region showing complete coverage of boundaries with precipitates.

Summary of observations from analysis of cracks in Demonstration Project #3

- LP testing of pipe-to-pipe welds showed multiple axial cracks in one of the four 740H pipes.
- Metallurgical analysis of these cracked regions showed that these cracks were sharp with minimal branching.
- Presence of denuded zones at grain boundaries ahead of the crack tips were also observed.
- The morphology of grain boundary precipitates and formations of denuded zones varied
    - Some boundaries showed discontinuous precipitates and denuded zone formation (similar to samples from Project #1 and Project #2).
    - Other boundaries showed large colonies of coarsened precipitates along with denuded zones.
    - In some cases, boundaries with only denuded zones and no grain boundary precipitates were also observed
    - However, in all the above instance, cavitation damage was observed at denuded zone regions.

Overall Summary of Failure Analysis and Relevant Findings for Experimental Testing Campaign

The results from the project's detailed failure investigations for three separate alloy 740H applications conclusively identified stress relaxation cracking (SRxC) during the post-weld heat-treatment (PWHT) cycle (also known as strain age cracking or stress relief cracking) as the damage mechanism. The evidence included the following observations:

- All cracking was identified after PWHT in weldments which showed no indications via NDE after welding
- The cracking was intergranular with minimal/no branching and was not uniquely associated with the weld metal, heat affected zone, or base metal region (growth was observed through multiple weldment zones)
- When the crack initiation location could be identified, it was found to be associated with local geometric stress concentrations
- There was limited cavitation ahead of crack tips indicating relaxation of the local stresses was being accommodated via creep damage
- Cracks surfaces had a thin oxide layer suggesting damage occurred early in the PWHT cycle
- Detailed microstructural analysis at the micro to nano-scale showed:
    - Highly strained regions near crack initiation using electron channeling contrast in the SEM
    - Localized recrystallization near crack initiation sites
    - The formation of coarsened zones and associated precipitate free zones (PFZs) in the grain boundaries associated with regions of high strain and cavity initiation and crack growth. Such features were not observed in the base metal or weld metal away from cracking. TEM confirmed a moving grain boundary associated with the CZ. This observation had only previously been observed in creep tested weldments due to compositional gradients in weld metal. Therefore, to confirm a moving boundary in base metal where no compositional gradient is present requires a high stress consistent with the damage mechanism of SRxC which requires a high stress.

There are many contributing factors which need to be considered for SRxC [11]. These can largely be classified as material, thermal history, and stress state. Based on the alloy 740H experience and failure analysis reports, available laboratory data, and knowledge of similar alloys [6-12, 16], a group of experts were asked to rank their opinion on the most important variables to consider leading to SRxC of alloy 740H. Table 10 shows these results with general agreement that the stress state (from residual stresses, constraint, and deformation) was playing a significant role in the observed failures with some disagreement on the importance of the welding process, PWHT conditions, bulk alloy chemistry (within the 740H specification range), and overall weld quality.

Table 10. Results of an expert solicitation of SRxC variables for alloy 740H

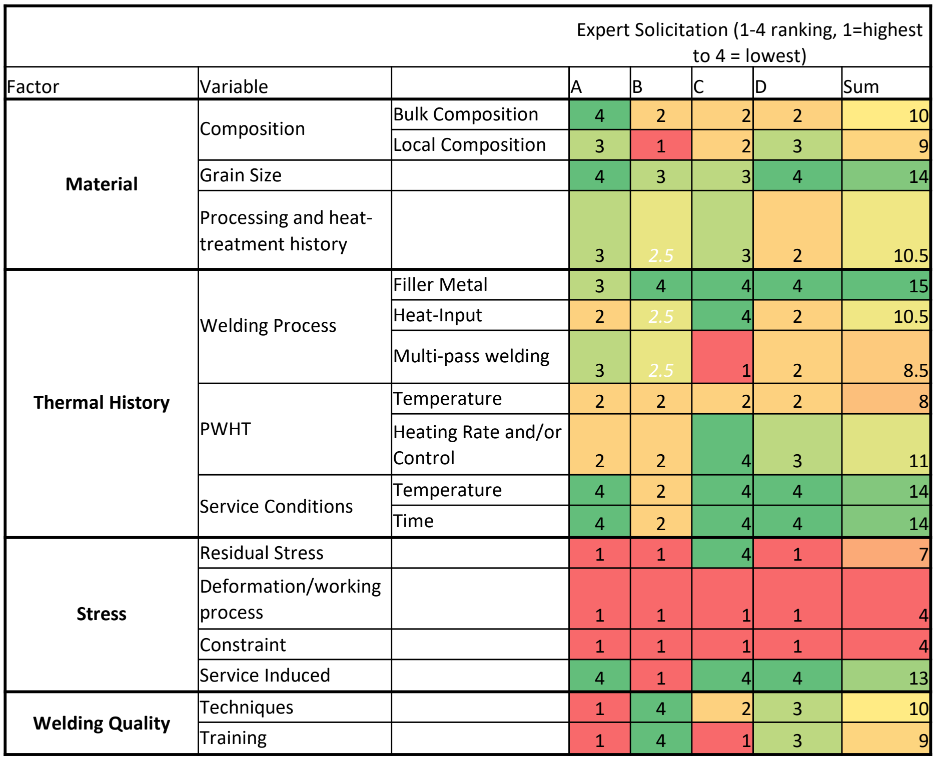

			Expert Solicitation (1-4 ranking, 1=highest to 4 = lowest)				
Factor	Variable		A	B	C	D	Sum
Material	Composition	Bulk Composition	4	2	2	2	10
		Local Composition	3	1	2	3	9
	Grain Size		4	3	3	4	14
	Processing and heat-treatment history		3	2.5	3	2	10.5
Thermal History	Welding Process	Filler Metal	3	4	4	4	15
		Heat-Input	2	2.5	4	2	10.5
		Multi-pass welding	3	2.5	1	2	8.5
	PWHT	Temperature	2	2	2	2	8
		Heating Rate and/or Control	2	2	4	3	11
	Service Conditions	Temperature	4	2	4	4	14
		Time	4	2	4	4	14
Stress	Residual Stress		1	1	4	1	7
	Deformation/working process		1	1	1	1	4
	Constraint		1	1	1	1	4
	Service Induced		4	1	4	4	13
Welding Quality	Techniques		1	4	2	3	10
	Training		1	4	1	3	9

Based on this feedback, the Task 2 laboratory study using a Gleeble™ thermo-mechanical simulator identified the following variables to test for using different heats of alloy 740H:

- Multiple strain levels to define the role of stress
- PWHT temperature
- Starting material condition (Solution annealed versus aged)

Three different heats of 740H alloy were selected for laboratory testing to simulate SRxC. These heats of material represent three separate melts of 740H, each of which was used to create a distinct product form. For ease of discussions, these three heats of materials are labeled as Heat A, Heat B and Heat C. Heat A represented material from a tubular product form, Heat B was a rolled plate material that was made into a seam welded pipe, and Heat C was an extruded pipe material. Heats labeled '2016' and '2018' in the table were other heats of 740H that were previously studied.

Table 11. Three heats of alloy 740H selected for laboratory testing in Task 3 (A, B, and C) along with the composition of two previous heats tested by Lehigh University (2016, 2018).

Element	Cr	Co	Al	Ti	Nb+Ta	Fe	C	Mn	Mo
UNS N07740	23.5-25.5	15.0-22.0	1.35-2.00	0.5-2.5	0.5-2.5	0-3.0	0.005-0.008	0-1.0	0-2.0
HT3130JY (2016 Heat)	24.527	20.218	1.357	1.366	1.497	0.1	0.023	0.25	0.35
HT3500JY (2018 Heat)	24.534	20.249	1.351	1.403	1.461	0.17	0.04	0.28	0.39
CLH4663 (Heat A)	24.334	20.173	0.938	1.775	2.037	0.34	0.029	0.29	0.61
HT6309JK (Heat B)	24.572	20.219	1.366	1.567	1.464	0.12	0.032	0.3	0.54
HT9067JY1 (Heat C)	24.575	20.205	1.507	1.458	1.545	0.41	0.033	0.28	0.56
Element	**Si**	**Cu**	**P**	**S**	**B**	**Ca**	**La**	**Ta**	**V**
UNS N07740	0-1.0	0-0.5	0-0.03	0-0.03	0.0006-0.006	-	-	-	-
HT3130JY (2016 Heat)	0.11	0.004	<0.002	0.0022	0.001	<0.0005	<0.002	<0.005	0.008
HT3500JY (2018 Heat)	0.116	0.004	<0.002	<0.0005	0.0022	<0.0005	<0.002	<0.005	0.007
CLH4663 (Heat A)	0.56	0.035	<0.002	<0.0005	0.0026	0.001	<0.002	<0.005	0.005
HT6309JK (Heat B)	0.128	0.008	<0.002	<0.0005	0.0013	<0.0005	<0.002	<0.005	0.006
HT9067JY1 (Heat C)	0.114	0.018	<0.002	<0.0005	0.0014	<0.0005	<0.002	<0.005	0.006
Element	**W**	**Zr**	**As**	**Mg**	**Pb**	**Sb**	**Se**	**O**	**N**
UNS N07740	-	-	-		-	-	-	-	-
HT3130JY (2016 Heat)	<0.005	0.022	<0.002	0.0022	<0.00002	0.0002	<0.0005	0.0001	0.0041
HT3500JY (2018 Heat)	<0.005	0.02	<0.002	0.0053	<0.00002	<0.0001	<0.0005	0.0003	0.006
CLH4663 (Heat A)	<0.005	0.024	<0.002	0.0062	0.00002	<0.0001	<0.0005	0.0039	0.0083
HT6309JK (Heat B)	<0.005	0.012	<0.002	0.0032	<0.00002	<0.0001	<0.0005	0.0001	0.0046
HT9067JY1 (Heat C)	0.02	0.019	<0.002	0.0013	<0.00002	<0.0001	<0.0005	0.0001	0.0044

Additionally, the role of cold deformation, due evidence of recrystallization in some of the welds, was explored as a variable in Task 3 through welding on cold-worked material. The material utilized for this work was from the same master heat as 'Heat B'.

3.1.2: Summary of Tech-to-market activities

In support of disseminating the learnings of this project's research to the research community to inform future research on alloy 740H, similar alloys, and SRxC, presentations were given (details in Section 6) at:

- A DOE sCO_2 cross-cutting team (FE, NE, EERE) on the energy industry experience with relaxation cracking phenomenon in the fabrication and operation of power plants
- (2 talks) The American Welding Society's (AWS) International Conference on Advanced in Welding and Additive Manufacturing Research (AWAMR).

Additionally, a paper has been reviewed and accepted for publication as a conference proceeding paper for the Superalloys 718 and Derivatives 2023 Conference (to be held in Pittsburgh, PA in May of 2023).

To assist the industry in the application of alloy 740H, in addition to the presentations highlighted above, EPRI hosted a ½ day 740H user group meeting to share fabrication and welding experiences in the application of 740H. Table 12 provides the agenda for the meeting which included over 50 attendees representing a focused group of users, fabricators, field service providers, technology developers, select research organizations involved with demonstration projects, the project team (EPRI and Special Metals Inc.), and multiple DOE offices. Overall, the workshop highlighted the breadth of demonstration activities across CSP, sCO_2, and transformational thermal (A-USC and SC/USC retrofit) technologies and the growing body of successful experience along with the practical challenges associated with the overall maturing supply chain.

Table 12. Agenda for EPRI-Led Meeting on alloy 740H User Experience

DECEMBER 13TH, 2021		
TIME	**TOPIC**	**PRESENTER**
10:00 am	**Welcome and Introductions**	
	Welcome	*Kamala Raghavan, DOE*
	Meeting Goals, Objectives, Specification Outline	*John Shingledecker, EPRI* *John Siefert, EPRI*
10:30 am	**Component and Heavy-Wall Fabrication Experience**	
	A-USC Comtest Experience: Header Fabrication and Assembly	*Dan Purdy, EPRI* *Philip Gilston, GE Steam Power*
	Recent Manufacturing Trials of Induction Bends, Welded Tube & Seam-Welded Pipe	*Jack deBarbadillo, SMC* *Dave O'Donnel, Rath Gibson*
11:00 am	**Demonstrations, Tubing, and Small-Bore Piping**	
	STEP Fired Heater	*Matthew Hauth, Optimus*
	Echogen Experience	*Tim Held, Echogen*
	NIBALO725 & HWT3	*Andreas Klenk and Magdalena Speicher, MPA* *Tobias Steck, GE Power Stuttgart*
12:00 pm	**Break**	
12:30 pm	**Demonstrations, Tubing, and Small-Bore Piping (continued)**	
	STEP & Sunshot Experiences	*Trenton Cook, Southwest Research Institute*
	Fabrication of a 740H Tubular Solar Receiver	*Jack Hinze, Brayton Energy*
	Weld Wire for Nickel-Based Alloys	*Bill Newell, Euroweld*
1:30 pm	**Field Fabrication and Installation Q/A Session**	
	Field & Site Observations	*Ronnie Golihue, SMC*
	Practical Challenges in the Field – Contractor's Perspective	*Tom Bouzek, BHI Energy*
1:50 pm	**Advanced Technologies and Design Needs**	
	Designing solar receivers with 740H	*Chuck Violand, Nooter/Eriksen*
	Compact Heat Exchangers 740H Experience	*Zhinjun Jia, Comprex*
2:10 pm	**Additional Participant Input**	
2:20 pm	Summary Discussion and Next Steps	*J. Shingledecker, EPRI*
2:30 pm	**Adjourn**	

To provide an alternative means of technology transfer to industry, EPRI is in the process of publishing a technical requirements guideline to provide purchasers and end users the opportunity to enhance purchase specifications for alloy 740H and to reduce the variability in fabrication or operation of alloy 740H components or systems [17]. The following section provides some of the key learnings from the project and industry meetings incorporated into the document.

A key part of these recommendations includes comprehensive welding guidance. The qualification of a welding process and welder to ASME Section IX will not guarantee success. Welding of nickel-based alloys and alloy 740H require guidance which goes beyond the minimum requirements given in the code of construction. The basic guidance for alloy 740H can be found in [18] which addresses welding technique and training including the following:

- Cleanliness
- Fluidity & penetration
- Bead shape
- Shielding gas selection
- Heat input, pre-heating, and interpass
- Weld reinforcement

The field findings and research suggest additional practical considerations are required to reduce the risk of SRxC. The new guidance provides recommendations as follows:

1. *Avoid excessive reinforcement and other local geometric changes which lead to high localized stresses.*

Figure 7 shows an example of excessive reinforcement resulting in a high stress location on the tube ID. When combined with the residual stresses from welding, this location initiated the crack which propagated through the wall thickness. For manual welding, providing favorable access and appropriate training and/or experience with nickel-based welding is critically important. Alternatively, automated welding may reduce the propensity for such features.

2. *Joint location and fabrication sequence should be considered in the design. This is especially true for manual welding to provide ease of access, reduce local constraint, minimize alignment requirements, and/or the introduction of excessive welding residual stress.*

In the demonstration project #1, see [12] for additional details, the failed tube butt welds were biased to the return end of the heater. All of the non-return end welds were conducted on a table with favorable welder access. Conversely, as shown in Figure 1, welder access was limited, especially as welding progressed. Furthermore, the closure welds often required ‘jacking tubes into place’ to align the two tubes. Such practices should be avoided and/or prohibited.

3. *Do not place welds at thickness transitions which can lead to high localized stresses in the weldment*

Transition pieces should be utilized to avoid placing welds at thickness transitions where the difference in stiffness can lead to increased localized stresses. This is true for tubing or piping applications. Special design or fabrication considerations must be given to transitions that occur between dissimilar materials to alloy 740H.

4. *Block fittings, intersections or valves must be avoided.*

It is relatively commonplace to procure block forgings that are subsequently machined into fittings, intersections or valves with minimal OD machining or contouring. Figure 56(a) shows a different view of the component from demonstration project #2. While a detailed model was not constructed, it is likely the large block tee piece acted as a heat-sink during welding thus requiring the welder to compensate with excessive heat input. Additionally, the non-symmetric shape of a thin tube into a solid block likely led to additional stresses upon cooling. Figure 5(b) shows an improved design where OD machining provided a more uniform circumferential thickness and eliminated the socket weld in favor of a full penetration butt weld. Figure 56(c) shows the completed new instrument attachment which did not crack after PWHT and is now in-operation.

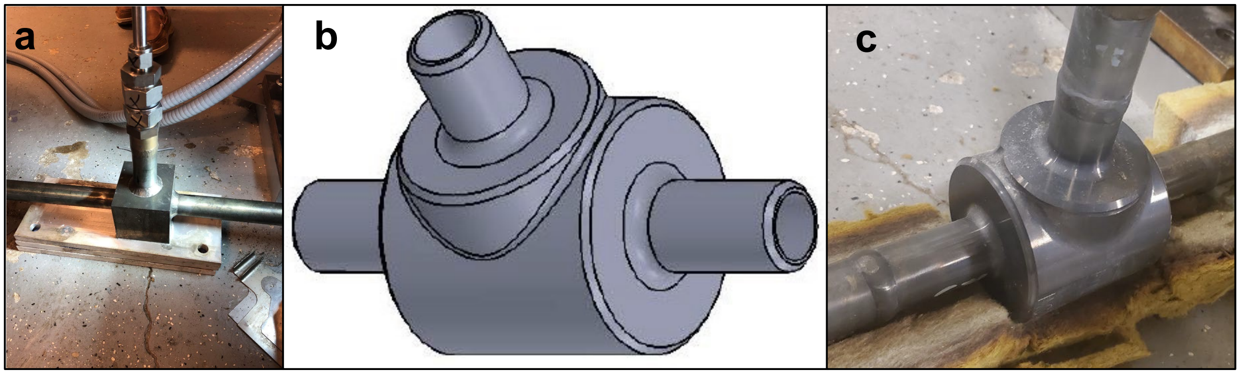

Figure 56. Original instrument ‘block tee’ design (a), a re-designed contoured tee(b), and the final fabricated tee which did not show any cracking (c).

5. *The sequence for volumetric inspection*

In many cases of SRxC, the fabricator or end user performed inspections after welding was complete only to discover failures that are believed to have originated after PWHT during a hydro acceptance test. While some inspection after welding should be performed to identify if gross defects are present and more easily remediated prior to PWHT, it is recommended to perform comprehensive inspection after PWHT as the origination of the majority of recent cracking has been attributed to SRxC.

3.2 Task 2: Laboratory Stress Relaxation Testing

Procedure

The stress relaxation cracking (SRxC) response is known to be affected by plastic strain and PWHT temperature in addition to heat-to-heat variations within a given alloy that can affect both composition and microstructural condition. A test procedure has recently been developed [16] to simulate the cracking mechanism under well controlled laboratory conditions so that these factors can be studied in a systematic manner.

A Gleeble® 3500 thermo-mechanical simulator was used to develop SRxC tests that reproduced the fracture features typical of SRxC failures [16]. Figure 57 shows a schematic illustration of the thermal and mechanical cycle during a basic SRxC test. The SRxC test was divided into three stages. First, the specimen was exposed to a Coarse-Grained HAZ (CGHAZ) thermal cycle with a peak temperature of 1200^{o}C. The CGHAZ thermal cycle was obtained using the Smartweld® package with a representative heat input of 2000 J/mm. After the CGHAZ thermal cycle, the sample was cooled to room temperature, followed by heating to the PWHT temperature at 100°C/min. During the first two stages of the SRxC test, the sample was not constricted and thus could freely expand/contract due to volumetric changes associated with heating/cooling. Once at the PWHT temperature, the 0.2% offset yield stress (at test temperature) was applied at 1.5mm/min crosshead speed to simulate the residual stress from welding, and the crosshead was then locked at this position. The crosshead was held fixed for eight hours during which the variation of stress with time was recorded at a constant temperature, shown by the third stage of the SRxC test in Figure 57. Locking the crosshead mimicked the constriction experienced by the HAZ of a weld during stress relaxation at the PWHT temperature. The test stopped before eight hours if the sample fractured during stress relaxation, otherwise the sample was pulled to failure at 2.5mm/sec at the end of eight hours of stress relaxation. The high strain rate was employed to quickly separate the fracture surfaces to help prevent arcing between the mating faces of the crack, thus preserving the fracture surface for post-test examination. As described above, the SRxC procedures required knowledge of the 0.2% offset yield strength for each PWHT temperature of interest. Thus, prior to the SRxC tests, tensile tests were conducted at each PWHT temperature for each heat. The strain during the tensile tests was measured using a dilatometer, measuring the change in diameter at the center of the sample. The tensile test samples were exposed to the same CGHAZ thermal cycle as the SRC test for that alloy.

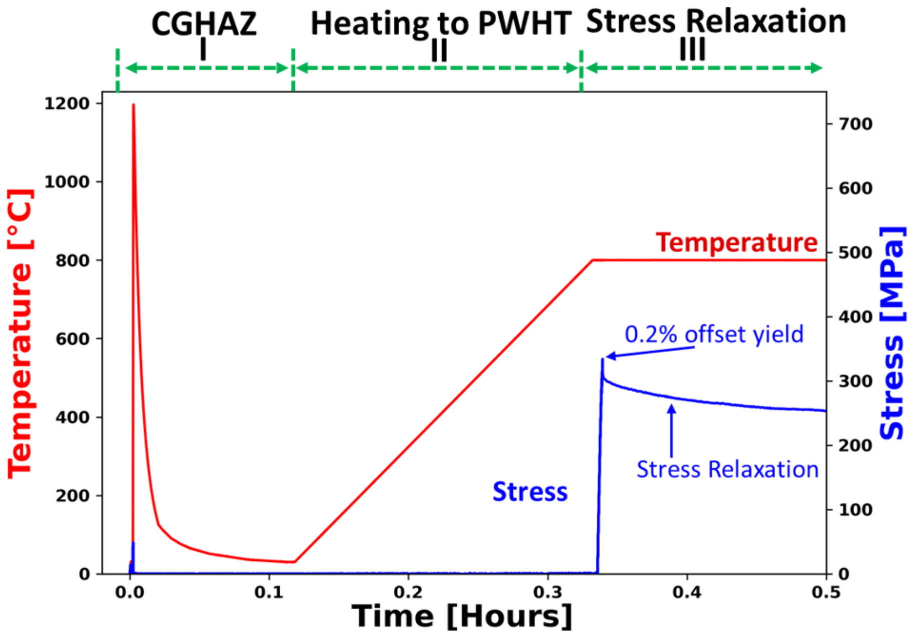

Figure 57. Schematic illustration of the thermal and mechanical cycle during a basic SRxC test.

As shown in Figure 58, the procedure was modified to study the effect of cold work on the SRxC behavior since cold working accelerates precipitation kinetics and increases SRxC susceptibility. Various levels of stress (associated with a corresponding level of plastic strain) were applied to the sample at room temperature after application of the CGHAZ thermal cycle. Stage two terminated with bringing the stress on the sample to zero. The sample was then heated to the PWHT temperature while maintaining zero stress on the sample (i.e., unconstrained). At the PWHT temperature, the 0.2 percent offset yield stress was applied to the sample and the crosshead was locked in place to start the stress relaxation (for eight hours). The 0.2 percent offset yield strength for these tests were re-measured at each PWHT temperature after application of the plastic strain (the earlier measured values could not be used as the application of the plastic strain increased the yield strength of the alloys). Figure 59 shows the sample geometry used of the SRC specimens. A double reduced geometry was devised to prevent failure occurring away from the center of the sample.

After the SRxC tests, one half of the sample was used for fracture surface analysis on a Hitachi 4300® or Zeiss LEO 1550 VP® Scanning Electron Microscopes (SEM). The other half of the sample was sectioned longitudinally, mounted and metallographically prepared for microstructural characterization. Microhardness traces were conducted on a Leco® microhardness tester from near the fracture surface to the unaffected base metal. The samples were then re-polished down to 0.05μm colloidal silica and etched. The samples were electrolytically etched at 6V DC in an 88%-12% solution of H_3PO_4 and H_2SO_4 saturated with CrO_3. The microstructure in the etched samples was first viewed under Riechert-Jung MeF3® Light Optical Microscope (LOM) or Olympus BH 2® fitted with Pax-It® LOM.

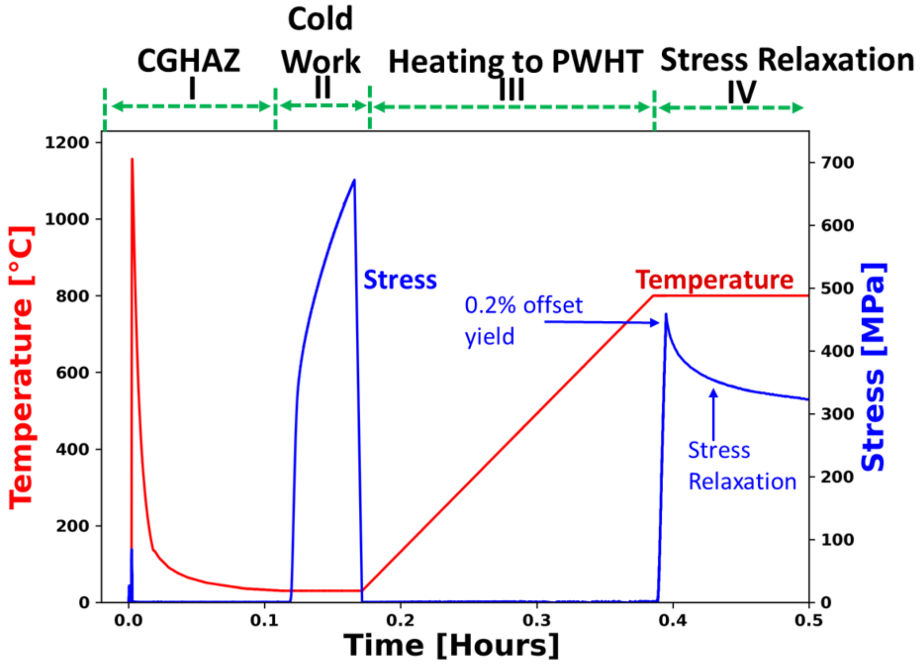

Figure 58. Schematic illustration of the modified SRxC test used to study the effect of cold work on the SRC behavior.

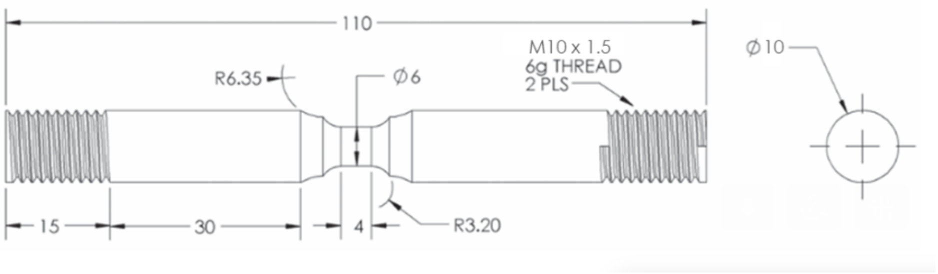

Figure 59. Sample geometry used for the SRxC specimens.

Results and Discussion

Figures 60 through 62 show the tensile test results for each alloy. The results from tests conducted at 800 and 900°C generally exhibit higher yield strengths compared to 700°C, which is attributed to the rapid precipitation of γ' at these temperatures. Also note that significant work hardening occurs at the lower temperatures of 700 and 800°C, and is generally absent at the higher temperatures of 900 and 1,000°C. Serrated yielding, also known as the Portevin–Le Chatelier (PLC) effect, is also observed. The PLC effect is associated with dynamic strain aging, where dislocations are pinned on solute atoms [19]. This has been widely documented for other commercial Ni-base superalloys as well [20-22]. Figure 63 shows the variation in tensile ductility as a function of test temperature. There is a significant ductility minimum at 800°C for all the alloys, and Heats A and C show lower ductility at most temperatures relative to Heat B.

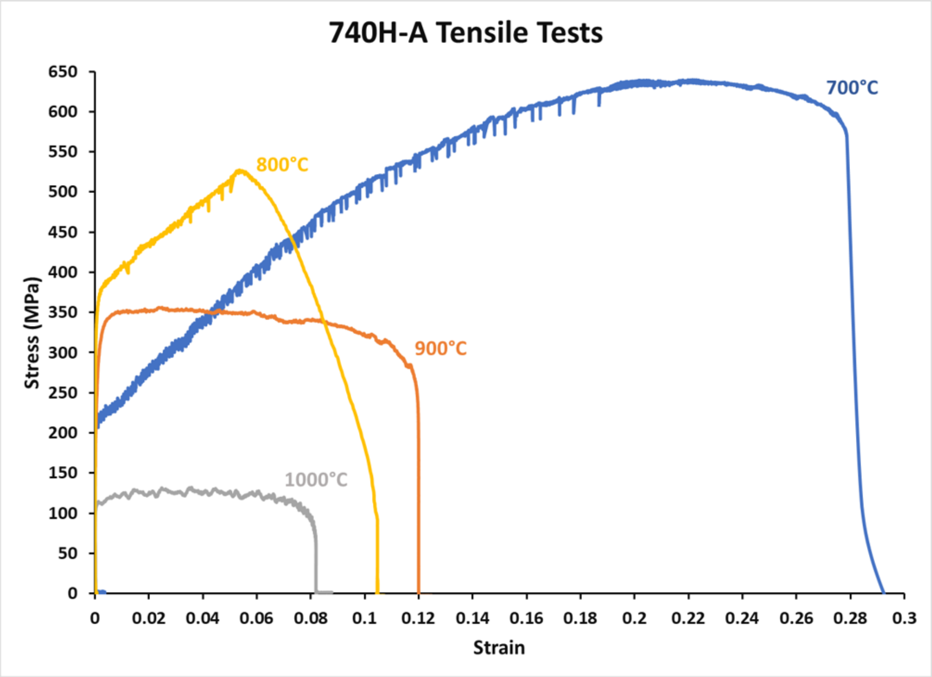

Figure 60. Tensile test results for Heat A.

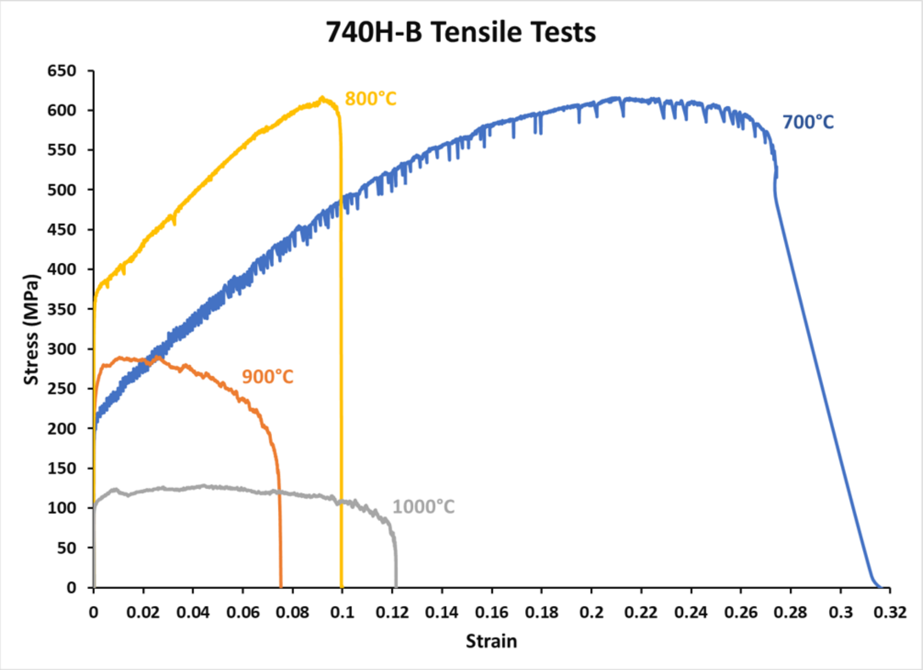

Figure 61. Tensile test results for Heat B.

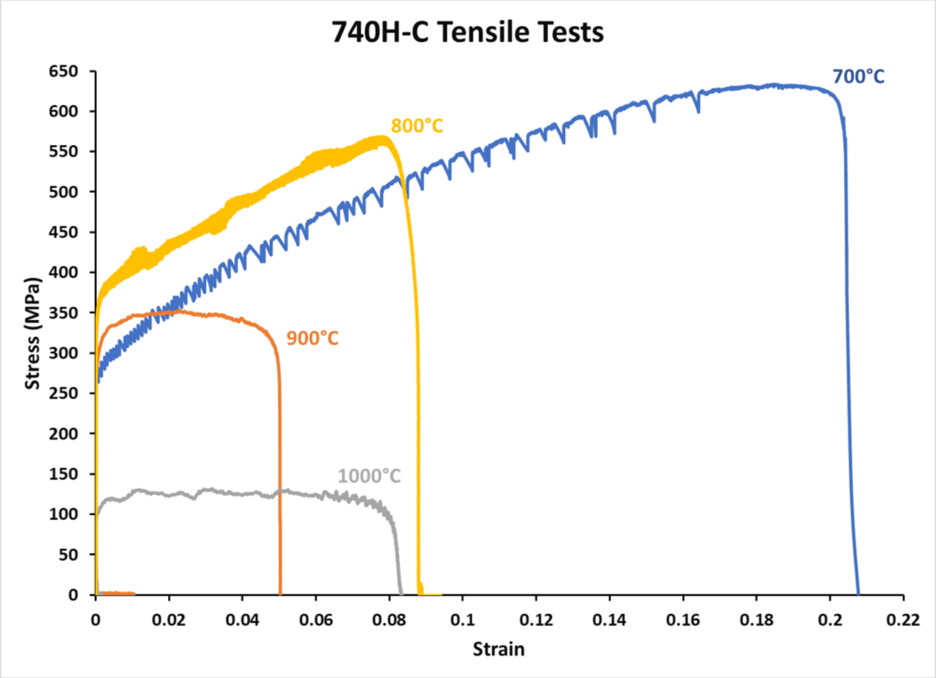

Figure 62. Tensile test results for Heat C.

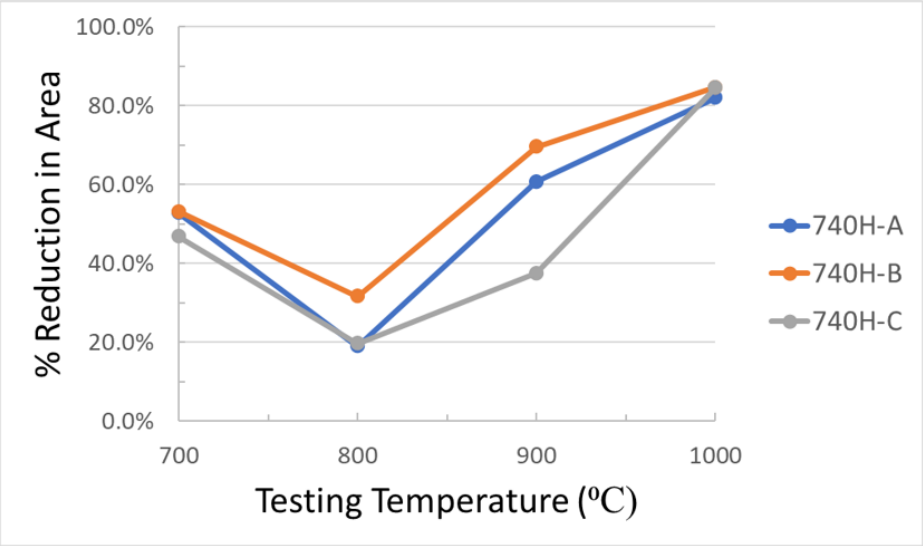

Figure 63. Variation in tensile ductility as a function of test temperature for all the heats.

Figure 64 compares the stress-strain curves at 800°C for all three heats of material evaluated in this project along with two additional heats labeled as “2016” and “2018”. Heat 2016 was shown to be quite susceptible to SRxC using the described test method [16], while the 2018 was shown to be quite resistant to SRxC under a wide range of test conditions [23]. Note that the 2016 heat shows a significantly reduced ductility relative to the 2018 heat. Similarly, there is a wide range of tensile ductility values associated with Heats A, B, and C. The tensile ductility results correlate reasonably well with the fracture modes of the tensile samples that are shown in Figures 65 through 76. At 700^{o}C, Heats A and B show microvoid coalescence (MVC) whereas Heat C shows some evidence of intergranular fracture that is reminiscent of SRxC. At 800^{o}C, all heats show intergranular fracture, but Heat B (with the highest tensile ductility) also shows significant amounts of ductile microvoid coalescence. Heats A and B exhibit all microvoid coalescence at 900^{o}C, whereas Heat C exhibits some intergranular fracture. All the heats fail by microvoid coalescence at 1000^{o}C.

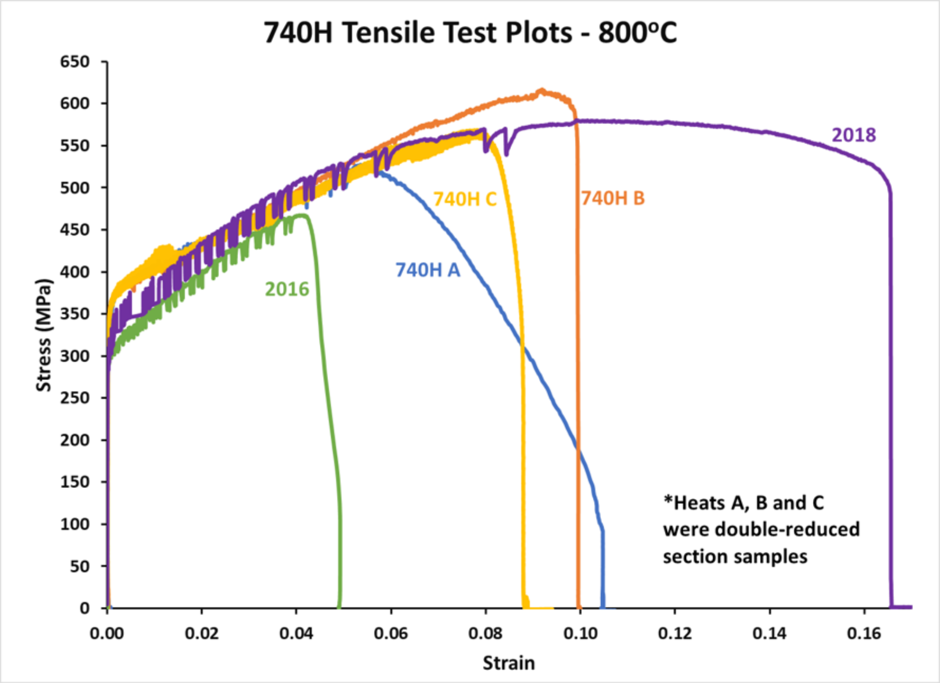

Figure 64. Stress-strain curves at 800^{o}C for all three heats of material evaluated in this project along with two additional heats labeled as “2016” and “2018”.

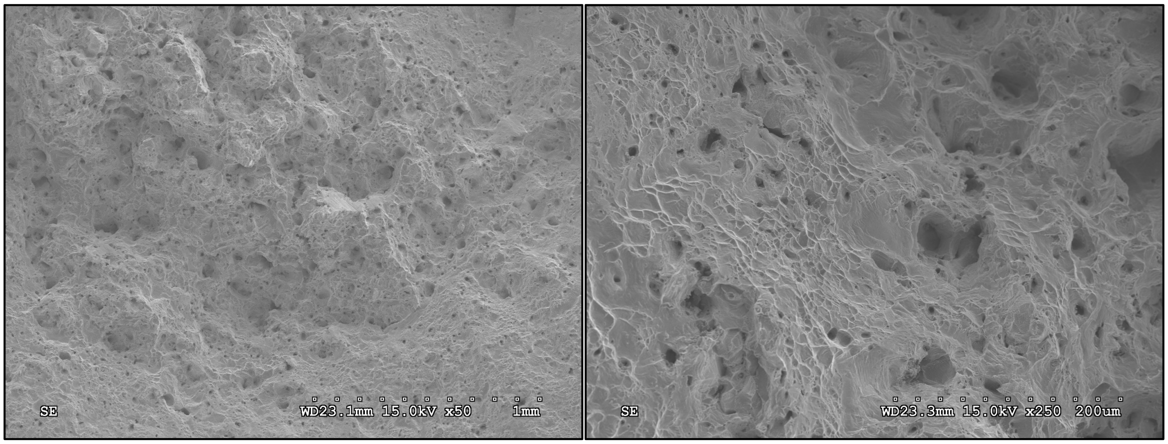

Figure 65. Fracture surfaces from Heat A tensile tested at 700^{o}C.

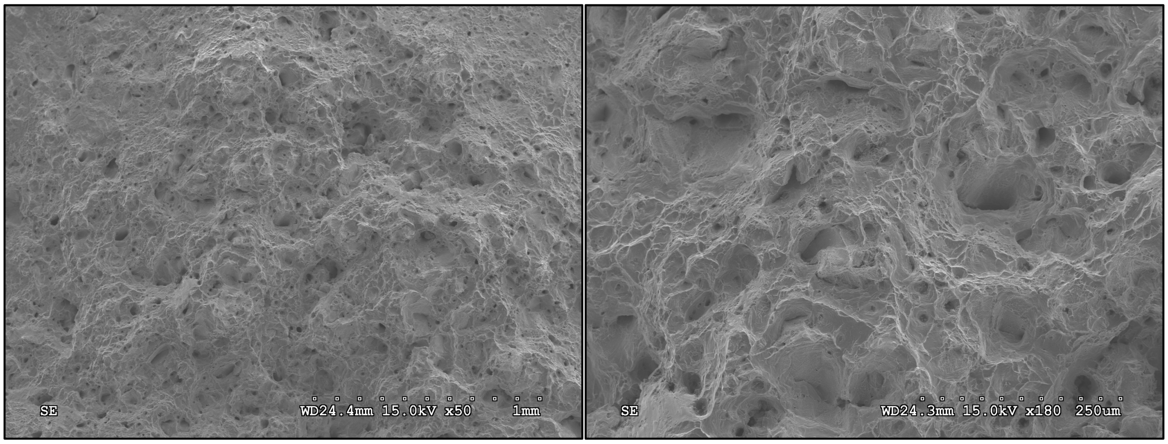

Figure 66. Fracture surfaces from Heat B tensile tested at 700°C.

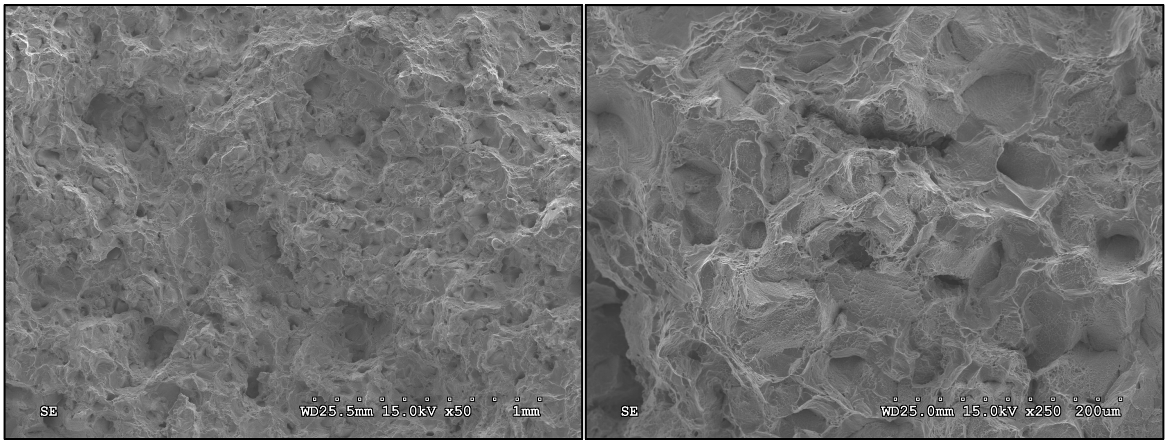

Figure 67. Fracture surfaces from Heat C tensile tested at 700°C.

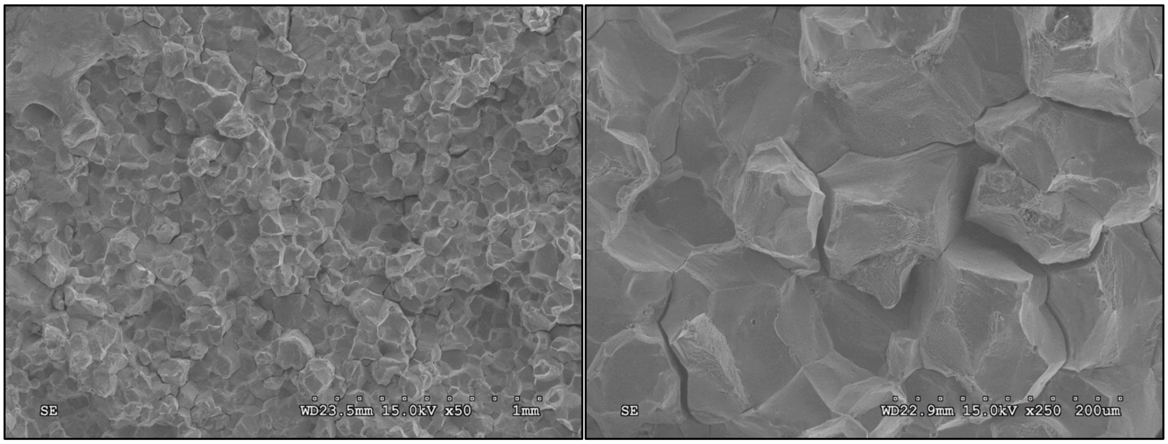

Figure 68. Fracture surfaces from Heat A tensile tested at 800°C.

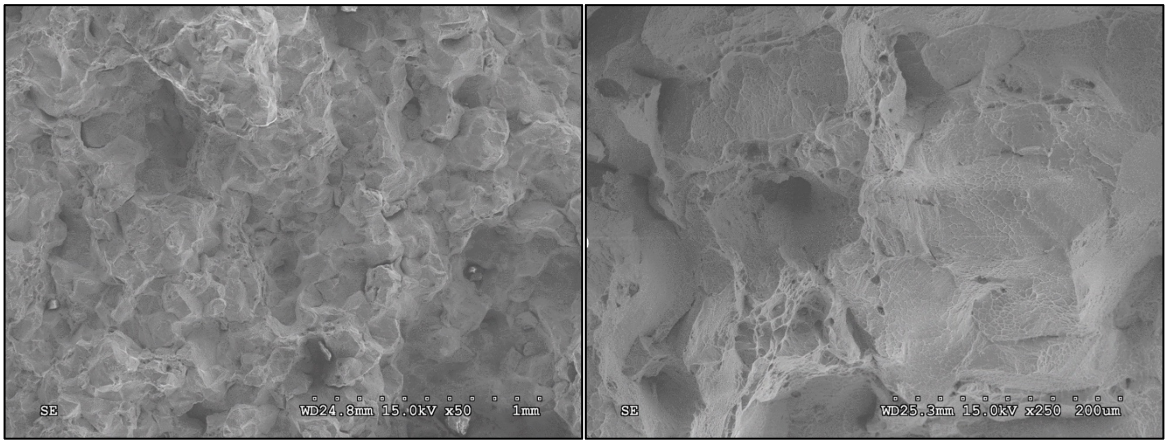

Figure 69. Fracture surfaces from Heat B tensile tested at 800^{o}C.

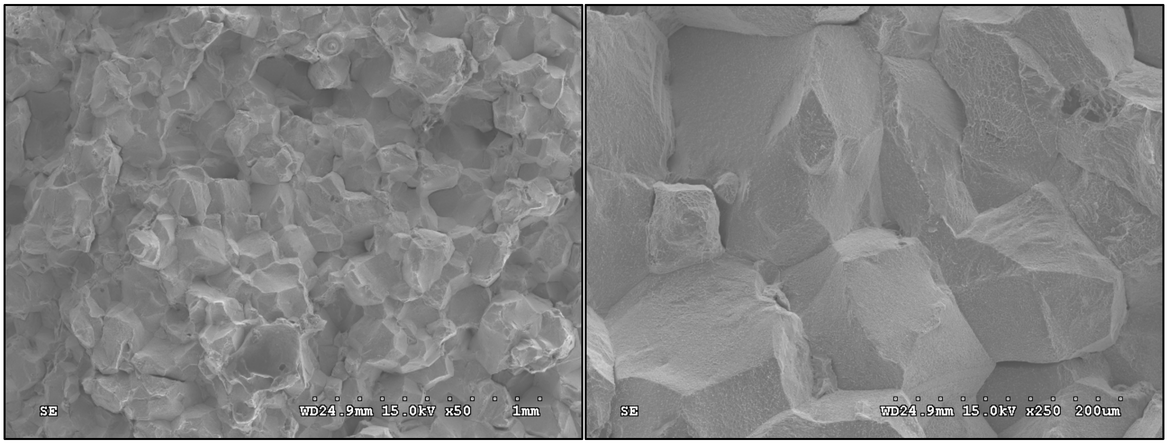

Figure 70. Fracture surfaces from Heat C tensile tested at 800^{o}C.

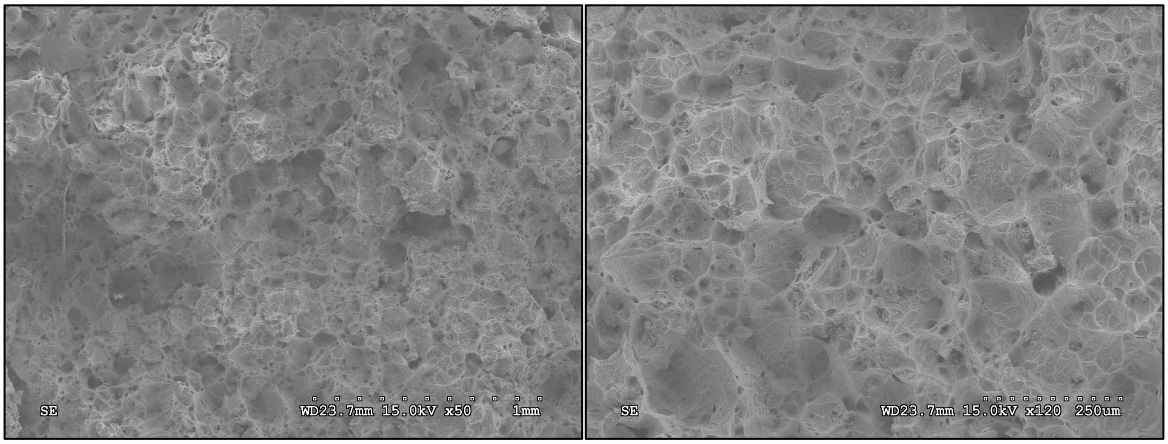

Figure 71. Fracture surfaces from Heat A tensile tested at 900^{o}C.

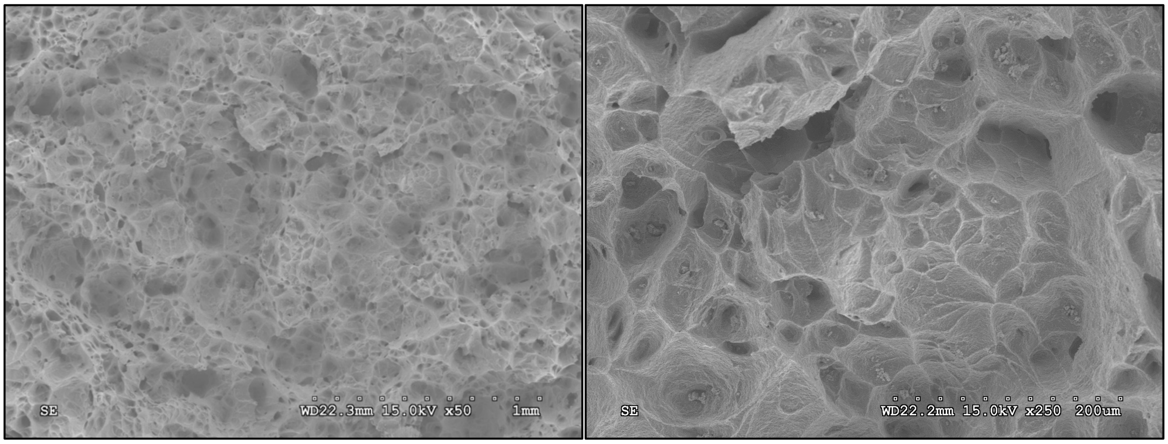

Figure 72. Fracture surfaces from Heat B tensile tested at 900^{o}C.

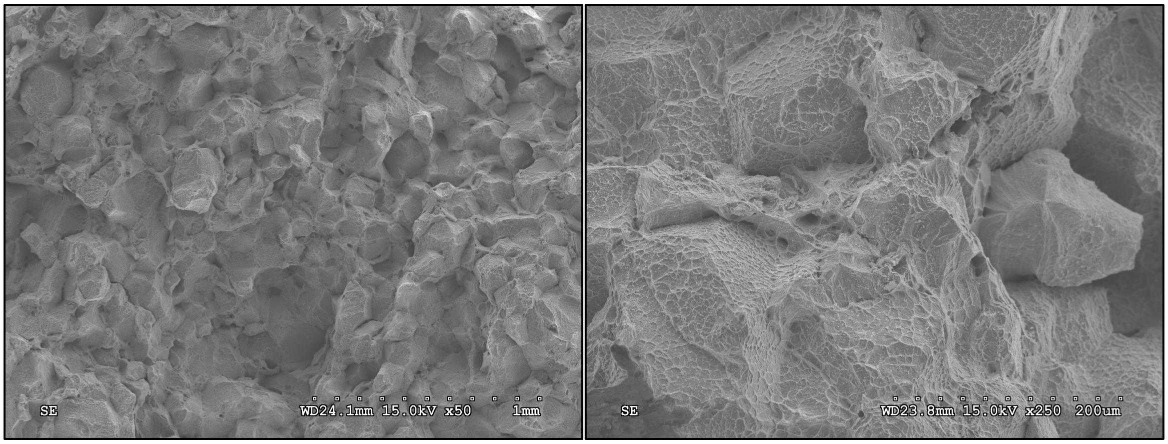

Figure 73. Fracture surfaces from Heat C tensile tested at 900^{o}C.

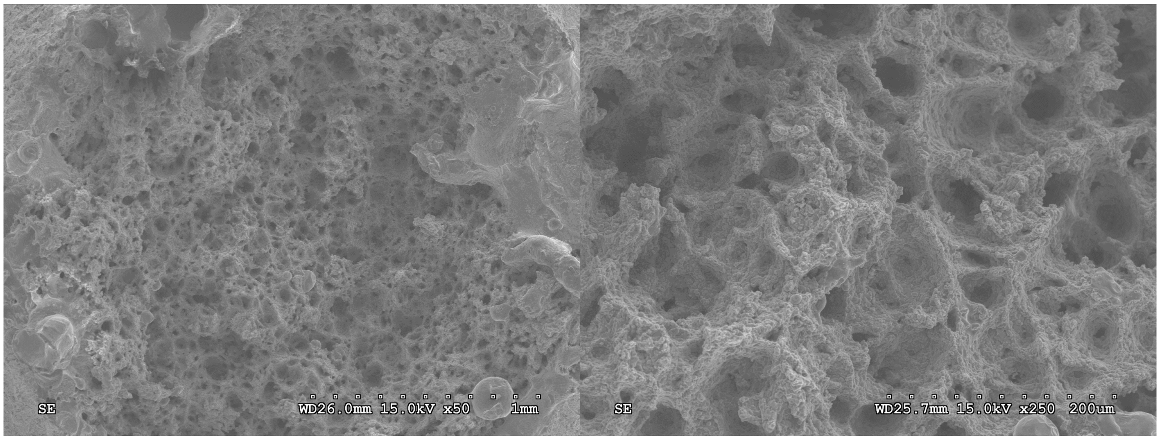

Figure 74. Fracture surfaces from Heat A tensile tested at 1000^{o}C.

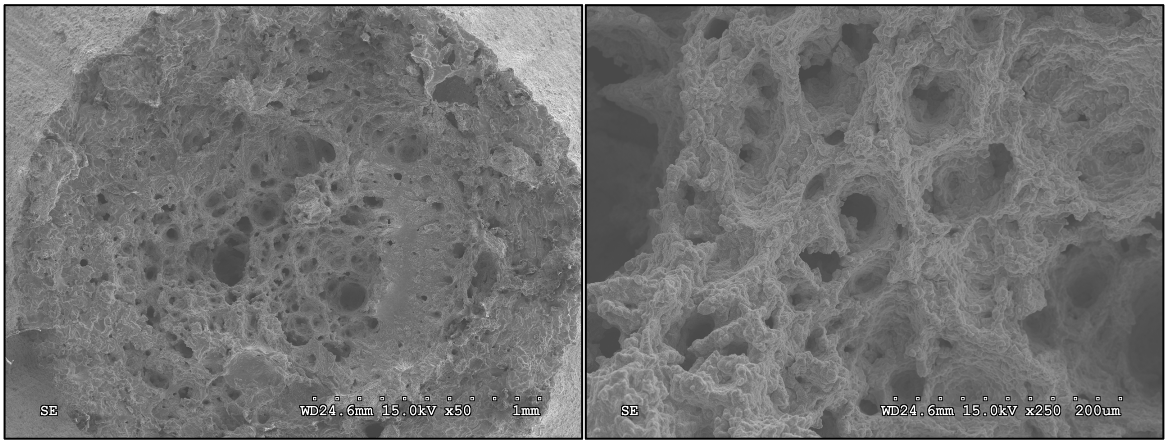

Figure 75. Fracture surfaces from Heat B tensile tested at 1000^{o}C.

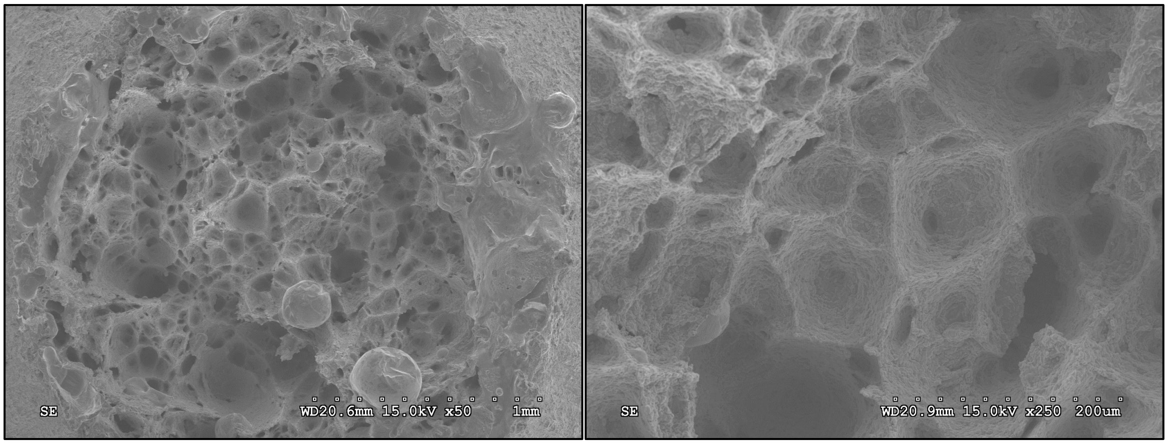

Figure 76. Fracture surfaces from Heat C tensile tested at 1000^{o}C.

Results from the SRxC tests conducted at 800^{o}C are shown in Figures 77 through 79. Results are shown for tests conducted at various levels of plastic strain that were applied after the CGHAZ thermal cycle and before the PWHT was applied. Strain levels from zero to just below the tensile failure strain for each heat were used during these tests. Note that none of the samples failed for Heat A even when a strain of 6% was applied, which is near the tensile fracture strain. For Heat B, failure in the SRxC test did not occur until a plastic strain level similar to the tensile fracture strain of 9% was used. Heat C failed at plastic strain levels of 4.75% and 5.5%, which are below the tensile fracture strain of ~ 8% (Figure 64). Note that relatively high SRxC susceptibility of Heat C correlates with the tensile results in which Heat C exhibited low tensile ductility and the largest amount of intergranular fracture. These results suggests that a simple tensile test, combined with fractography, may provide a preliminary indication of SRxC susceptibility.

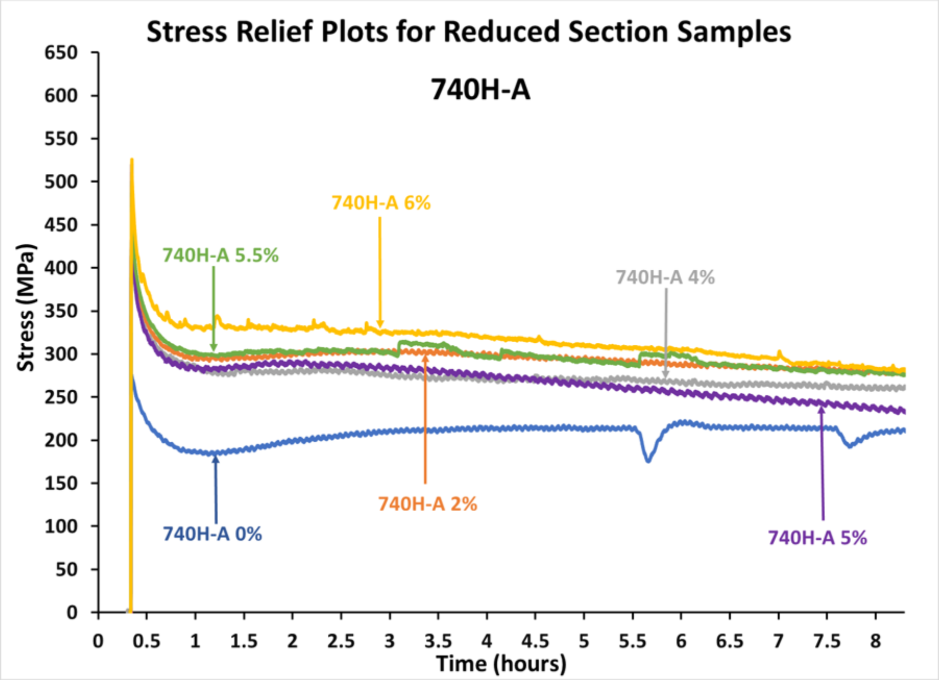

Figure 77. Results from the SRxC tests conducted at 800^{o}C for Heat A at various strain levels.

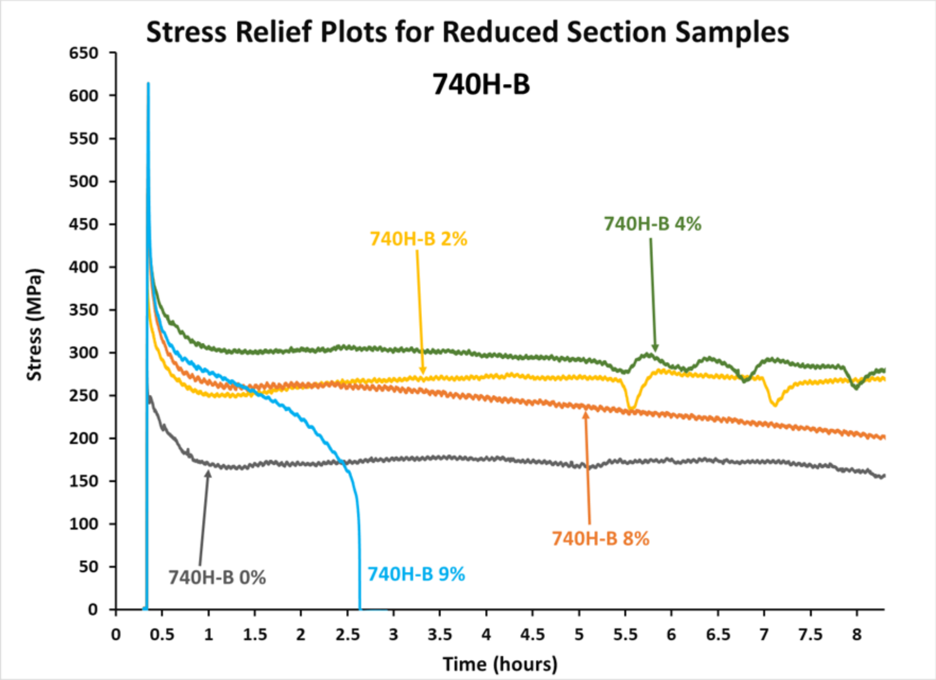

Figure 78. Results from the SRxC tests conducted at 800^{o}C for Heat B at various strain levels.

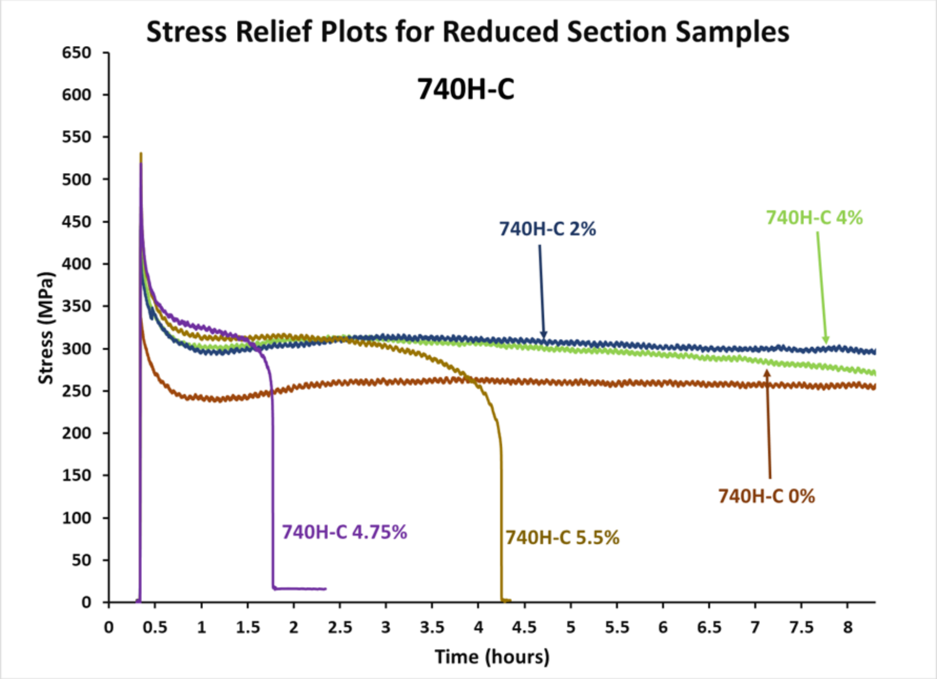

Figure 79. Results from the SRxC tests conducted at 800°C for Heat C at various strain levels

Figures 80 through 82 show SRxC results for each heat conducted at various PWHT temperatures and a constant plastic strain of 4%. None of the samples failed under these conditions. It is interesting to note that the level of residual stress reduction is rather small at both 700°C and 800°C, whereas a significant reduction in residual stress occurs when the PWHT temperature is increased to 900°C. This large reduction in residual stress is likely to be at least partly associated with instability and a concomitant lower phase fraction of γ' at 900°C. Considering that 900°C also provides a significant improvement in ductility (and reduction of brittle intergranular fracture) for all heats considered (Figure 63), additional work may be warranted to increase the standard PWHT temperature of IN740H to temperatures above 800°C if practically feasible.

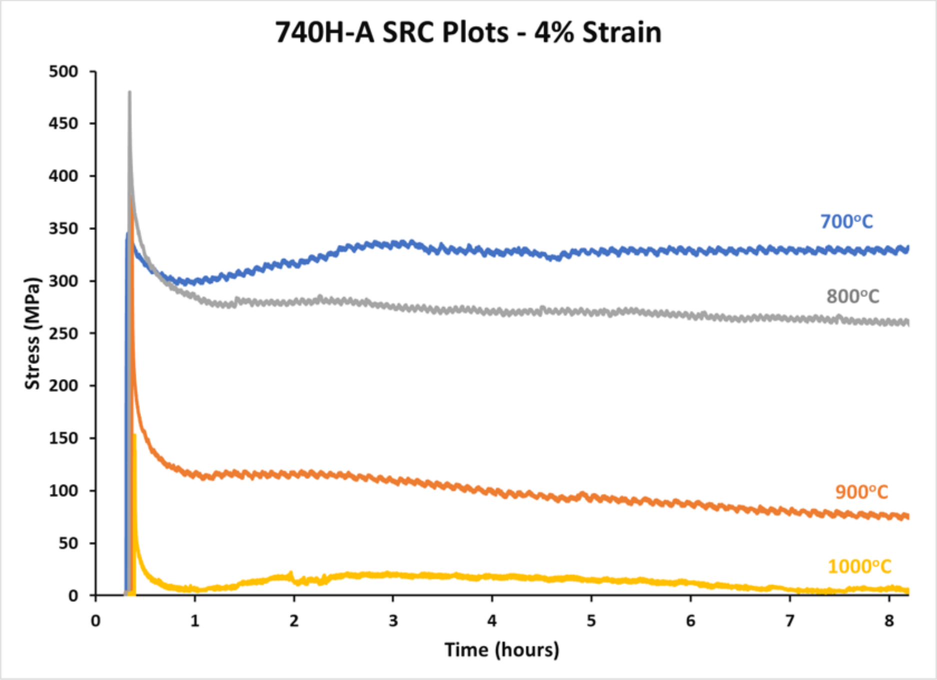

Figure 80. Results from the SRxC tests conducted Heat A at various PWHT temperatures and a constant plastic strain of 4%.

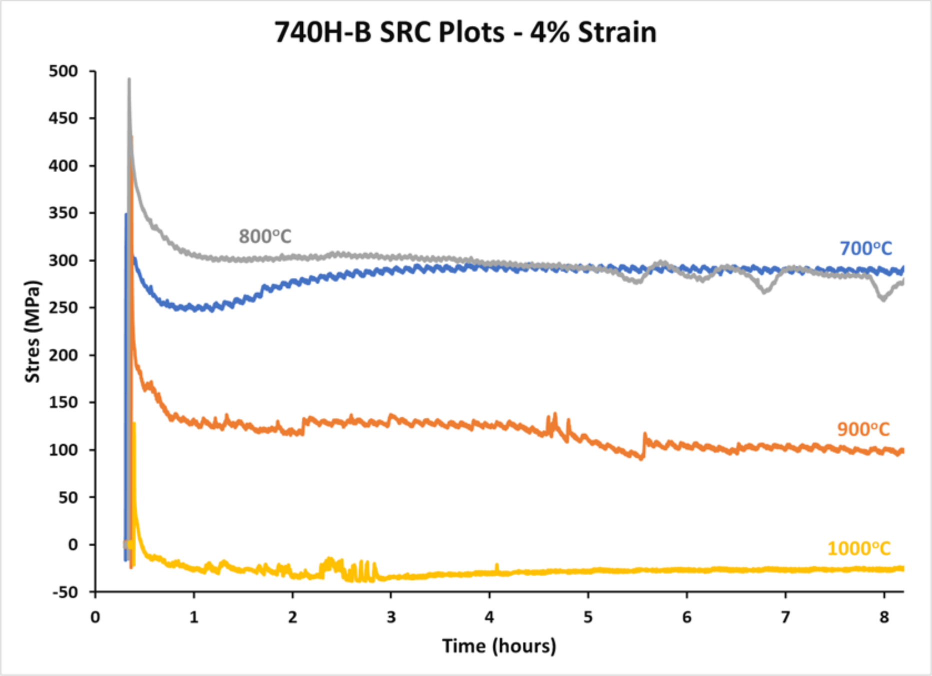

Figure 81. Results from the SRxC tests conducted Heat B at various PWHT temperatures and a constant plastic strain of 4%.

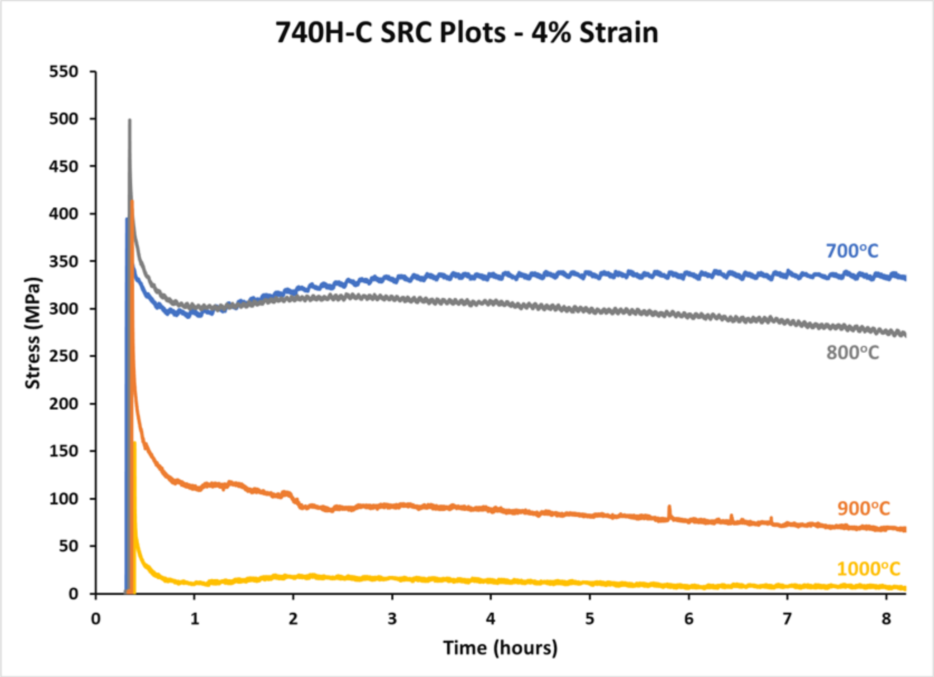

Figure 82. Results from the SRxC tests conducted Heat C at various PWHT temperatures and a constant plastic strain of 4%.

Additional tests were conducted to evaluate the SRxC susceptibility of IN740H in the solution treated and precipitation hardened conditions. Heat C was used for these experiments since it exhibited the highest susceptibility to SRxC. The sample used for the solution treated condition was given the CGHAZ treatment to a peak temperature of 1200°C, held at 1200°C for two minutes to promote dissolution of γ', and then free-cooled to room temperature (at about 8.4°C/s). The sample used for the precipitation hardened condition was first given the same treatment as the solution treated sample, followed by slow heating to 800°C at about 1°C/s, held at 800°C for 30 minutes to promote γ' formation, and then free-cooled to room temperature (at about 3.7°C/s). Forty Vickers hardness tests were conducted on each sample to verify the expected differences in precipitation. The solution treated sample had a hardness of 200 HV ± 8.8 HV, while the precipitation hardened sample had a hardness of 355 HV ± 8.5 HV. The difference is also readily apparent in the tensile tests (conducted at 800°C) that are shown in Figure 83. Figure 84 compares the SRxC results for each condition when tested at 800°C and a strain level of 2%. The sample in the precipitation treated condition failed almost immediately, while the sample in the solution treated condition failed after about four hours. Thus, as expected, the starting condition of the alloy will have a significant effect on the ability of the alloy to successfully relieve residual stress during PWHT by plastic deformation without brittle fracture. It is also interesting to note that the extended time (two minutes) at 1200°C for the sample tested in the solution treated condition increased susceptibility to SRxC relative to no hold time at the CGHAZ peak temperature. Note from Figure 79 that the same heat (Heat C) did not fail after eight hours at 800°C when a standard CGHAZ thermal cycle and strain of 2% was used. However, the sample failed in about four hours after being held at the peak CGHAZ temperature for two minutes. This suggests that, in the absence of a hold time, the γ' may only have time to coarsen (and not fully dissolve) during the CGHAZ thermal cycle, which could lead to softening and an increased ability to relieve residual stress by plastic deformation during the subsequent PWHT. In contrast, the extended time at the CGHAZ peak temperature may dissolve all/most of the γ', and then lead to subsequent precipitation of fine γ' during the PWHT temperature. The associated increase in strength would limit the ability of the alloy to uniformly relieve the residual stress by plastic deformation. Additional microstructural characterization should be conducted on these samples to conform this possible effect.

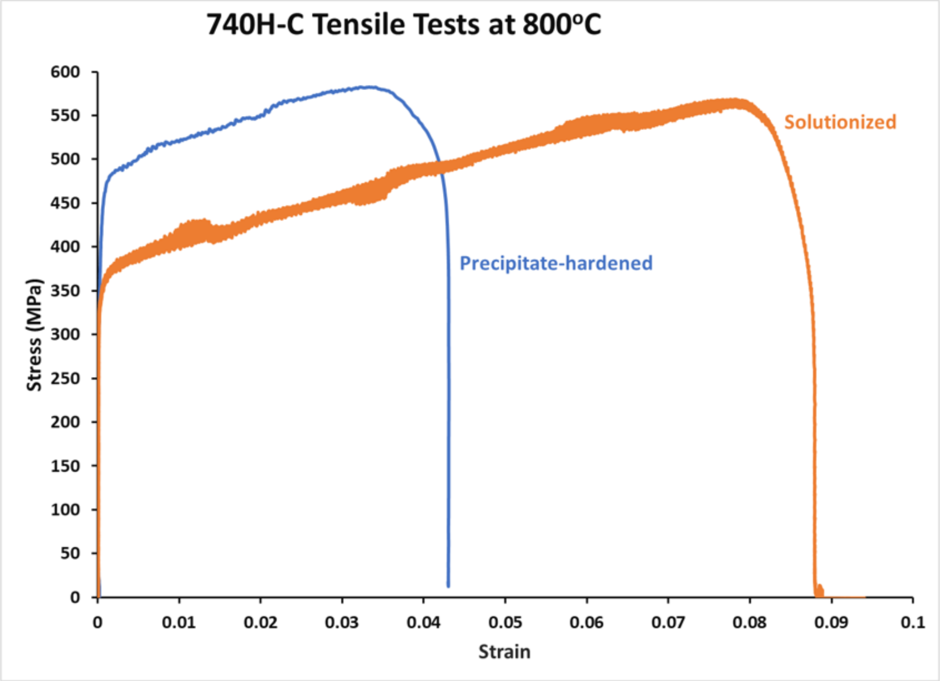

Figure 83. Tensile tests conducted at 800°C for Heat C in the precipitation hardened and solution treated conditions.

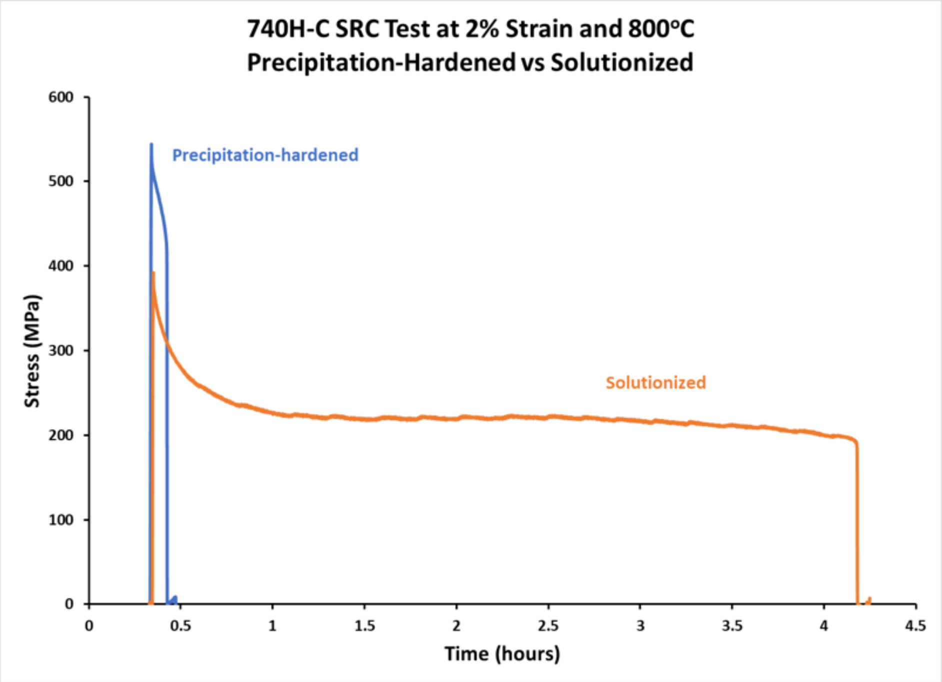

Figure 84. SRxC test results conducted at 800°C for Heat C in the precipitation hardened and solution treated conditions at a strain level of 2%.

Figure 85 shows typical fracture features associated with the failures from this test. The results shown as an example are from Heat C that was tested at 4.75% strain that failed after about 1.5 hours at the PWHT of 800°C. The failed surface exhibits intergranular fracture in which microvoid coalescence is confined to the grain boundaries (Figure 85a). The SEM photomicrographs shown in Figures 85b and 85c were acquired on a cross sectional sample from areas of secondary grain boundary cracking just below the fracture surface. The cracking is associated with precipitate-free zones along the grain boundaries. Thus, failure occurs due to localized plastic deformation of the soft zone along the grain boundaries associated with the precipitate-free zone, which accurately simulates the changes in grain boundaries observed from the service failures.

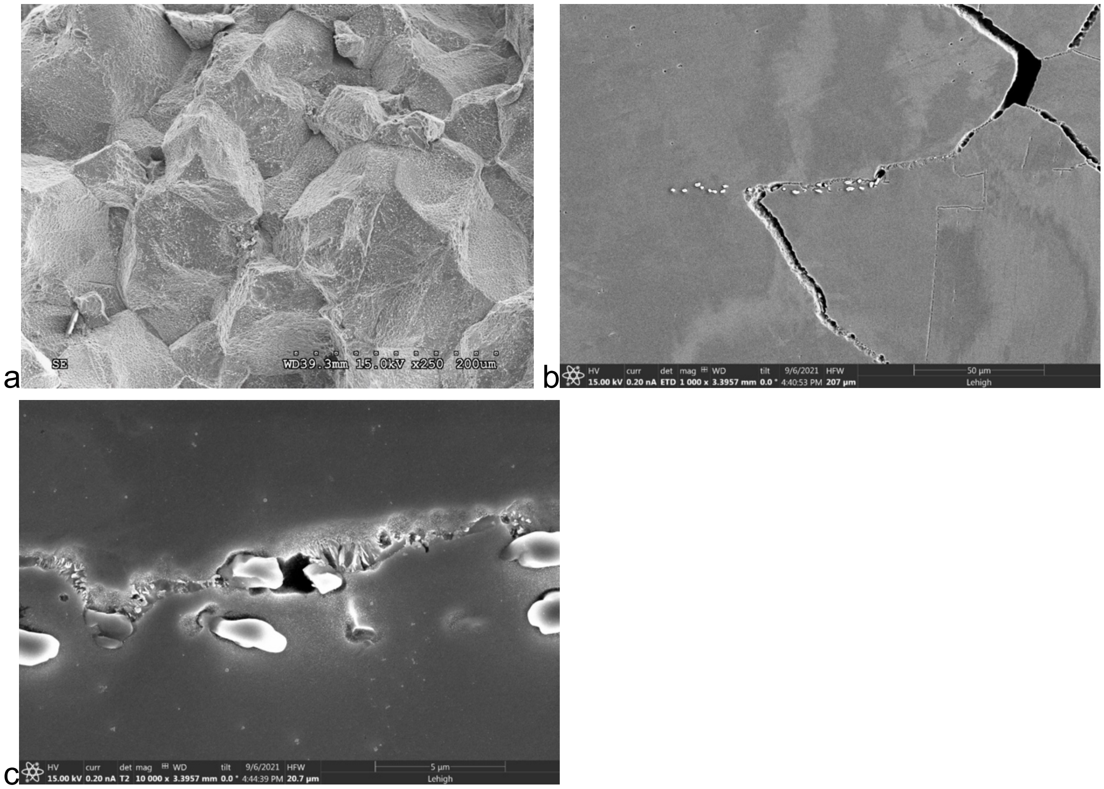

Figure 85. Examples of SEM characterization of typical fracture features associated with the failures from Heat C that was tested at 4.75% strain that failed after about 1.5 hours at the PWHT of 800 ^{o}C, including (a) the fracture face, (b) a cross-sectional image of typical grain boundary cracks, and (c) confirmation of PFZs associated with the observed cracking

Figure 86 shows LOM cross-sectional images from Heat C in which the sample was given 2% plastic strain and tested for eight hours at 800 ^{o}C but was not pulled to failure after the test (this sample did not fracture after eight hours at 800^{o}C). Although the sample did not fail during the test, there is obviously extensive crack initiation after eight hours at the PWHT temperature. This demonstrates that the failure time and/or lack of failure during the test cannot be used alone as an indicator of SRxC susceptibility.

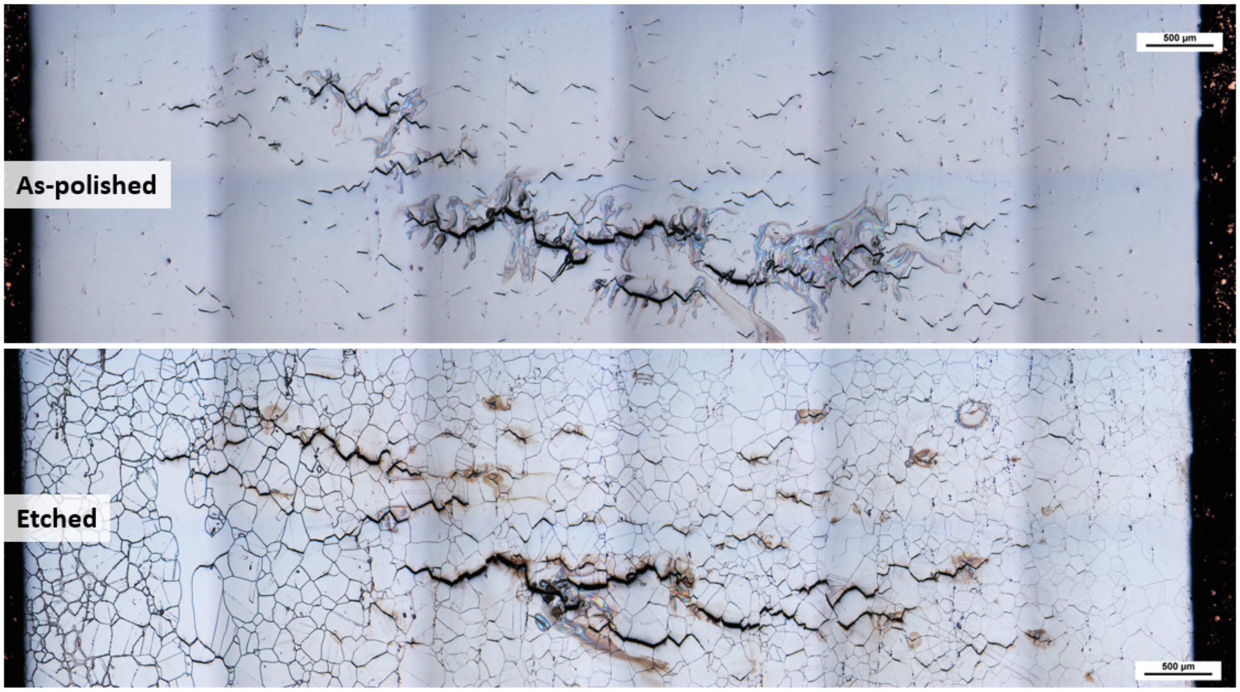

Figure 86. LOM cross-sectional images from Heat C in which the sample was given 2% plastic strain and tested for eight hours at 800°C, but was not pulled to failure after the test (this sample did not fracture after eight hours at 800°C).

A procedure was recently developed [16] that utilizes six measures of the SRxC test results to develop a method for quantitatively ranking the cracking susceptibility of various alloys, PWHT temperatures, and strain levels. The procedure in described in detail elsewhere [16] and is briefly reviewed here. The six measures of SRxC susceptibility include the time to failure, amount of stress relaxed, ductility, increase in hardness during PWHT (relative to unaffected base metal), type of fracture mode, and nature of secondary cracking below the fracture. Higher susceptibility to SRxC is correlated to reductions in the failure time, amount of stress relaxed, and ductility. An increase in hardness during PWHT would also indicate increased SRxC susceptibility, as would the occurrence of intergranular cracking.

In terms of the fracture and secondary cracking mode, recent work [16] has shown that four different types of fracture modes and subsurface cracking can occur during SRxC testing, depending on the susceptibility of the alloy and PHWT conditions (i.e., temperature and plastic strain). The different types of fracture and subsurface cracking modes observed in this work are shown in Figures 87 and 88, respectively. Type I and II fracture modes are intergranular with very low ductility. Type I fracture, which was not observed in this work, exhibits grain facets that are smooth with no evidence of significant localized plastic deformation. In contrast, the Type II fractures exhibit grain facets with microvoid coalescence (MVC), suggesting localized softening near the grain boundary. The Type III fracture mode is a mixed type of IG and ductile MVC with moderate ductility. Thus, Type III fracture mode indicates moderate susceptibility to SRxC. The Type IV fracture mode is completely ductile with MVC, which indicates that the alloy can accommodate plastic strain and hence is resistant to SRxC. The Type III & IV fracture surfaces are from the samples that did not fail during the test and hence were pulled to failure at the end of eight hours. Similarly, four major types of secondary cracks were observed below the fracture surface as shown in Figure 88. The Type I secondary cracks exhibit extensive intergranular cracking with equiaxed grains and low ductility. Minimal plastic deformation of the grains (as evident by the preserved equiaxed grain structure) with intergranular secondary cracks is indicative of cracking (instead of plastic deformation) being the active mechanism of stress relaxation. Hence, Type I secondary cracks indicate high SRxC susceptibility. The Type II cracks are also rather sharp and intergranular, but with lower frequency than Type I cracks. In addition, samples with Type II cracks exhibit slightly increased plasticity (as indicated by the elongated grains) that is indicative of lower SRxC susceptibility as compared to Type I. The Type III cracks are intergranular, but the cracks are rounded with evidence of blunting associated with appreciable plastic deformation. Finally, samples with Type IV cracks exhibit extensive plasticity (MVC) and no failure during the SRC test, thus show resistance to SRxC under the test conditions.

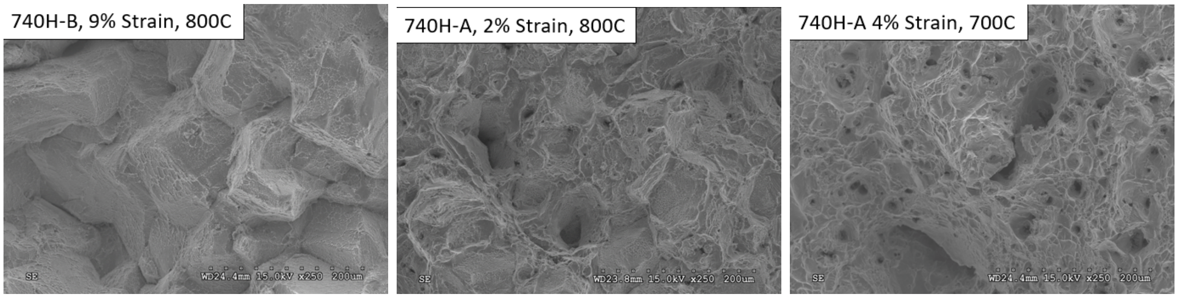

Figure 87. Different types of fracture modes observed in this work. Left – Type II, Middle – Type III, Right – Type IV.

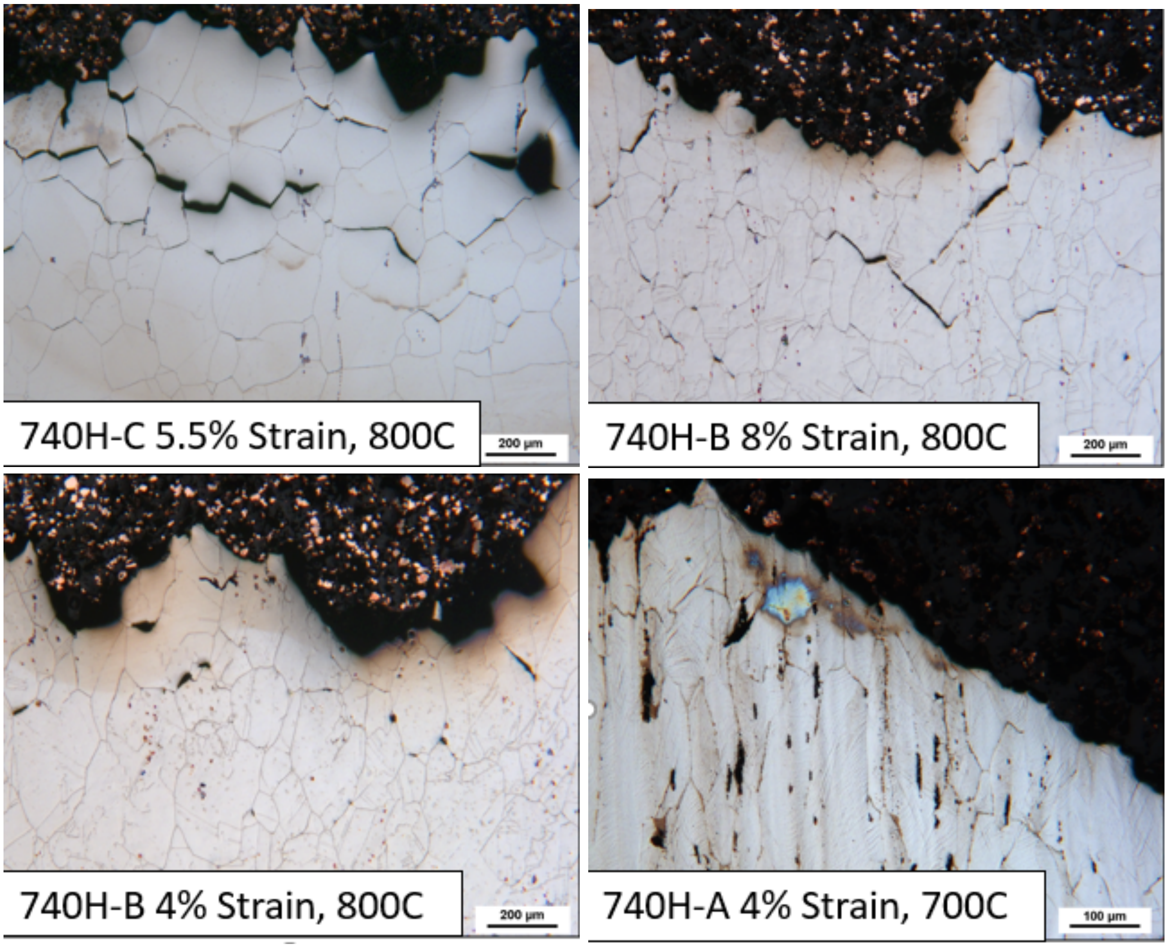

Figure 88. Different types of subsurface cracking modes observed in this work. Top Left – Type I, Top Right – Type II, Bottom Left – Type III, Bottom Right – Type IV

The six measures of SRxC susceptibility (time to failure, percentage stress relaxed, ductility, increase in hardness during PWHT, fracture mode, secondary cracking mode) were combined with concepts of the Risk Priority Number (RPN). The RPN is a tool in Failure Modes and Effect Analysis (FMEA) used for risk assessment of various critical modes of failure for any design or process. In a similar manner, the six measures of cracking susceptibility were combined to provide a Susceptibility Number (SN), where higher SN values correlate with higher cracking susceptibility. Figure 89 shows the SN values for different alloys and conditions. The red data points are from recent SRxC test results [16] conducted for a very wide range of alloys, PWHT temperatures, and plastic strain levels, while the blue data points are for tests conducted in this project. These previous results (i.e., red data points) demonstrated very good correlations to known SRxC susceptibility levels observed in practice. For example, the precipitation hardened alloys (Grade 22V steel, 282, IN740H, 347H) are known to be quite susceptible to SRxC at temperatures where the precipitation kinetics are the fastest, and this is revealed in the SRxC results. The precipitation hardened alloys are generally more susceptible to

SRxC because an unfavorable microstructure can form during PWHT in which the grain interior becomes quite strong while a softened precipitate-free zone can form along the grain boundaries. With this microstructure, plastic deformation associated with stress relief is highly localized along the soft precipitate-free zone, leading to premature fracture that exhibits the classic intergranular fracture that has microvoid coalescence confined to the grain boundary regions. Plastic strain increases the susceptibility to SRxC when the PWHT is conducted within the temperature range where the precipitation kinetics are high. This occurs for two reasons. First, application of plastic strain prior to PWHT reduces the amount of plastic strain available for stress relief. Second, the increase in dislocation density associated with plastic strain accelerates the precipitation kinetics due to enhanced diffusion. Alloys, PWHT temperatures, and strain levels that fell within the “Susceptible” range in Figure 89 all exhibited failure during the SRxC test with intergranular fracture, subsurface intergranular cracking, and low ductility (< 10%). Alloys, PWHT temperatures, and strain levels within “Moderate” range did not fail during the SRxC test, but exhibited some extent of intergranular fracture and subsurface cracking with moderate ductility (< 20%).

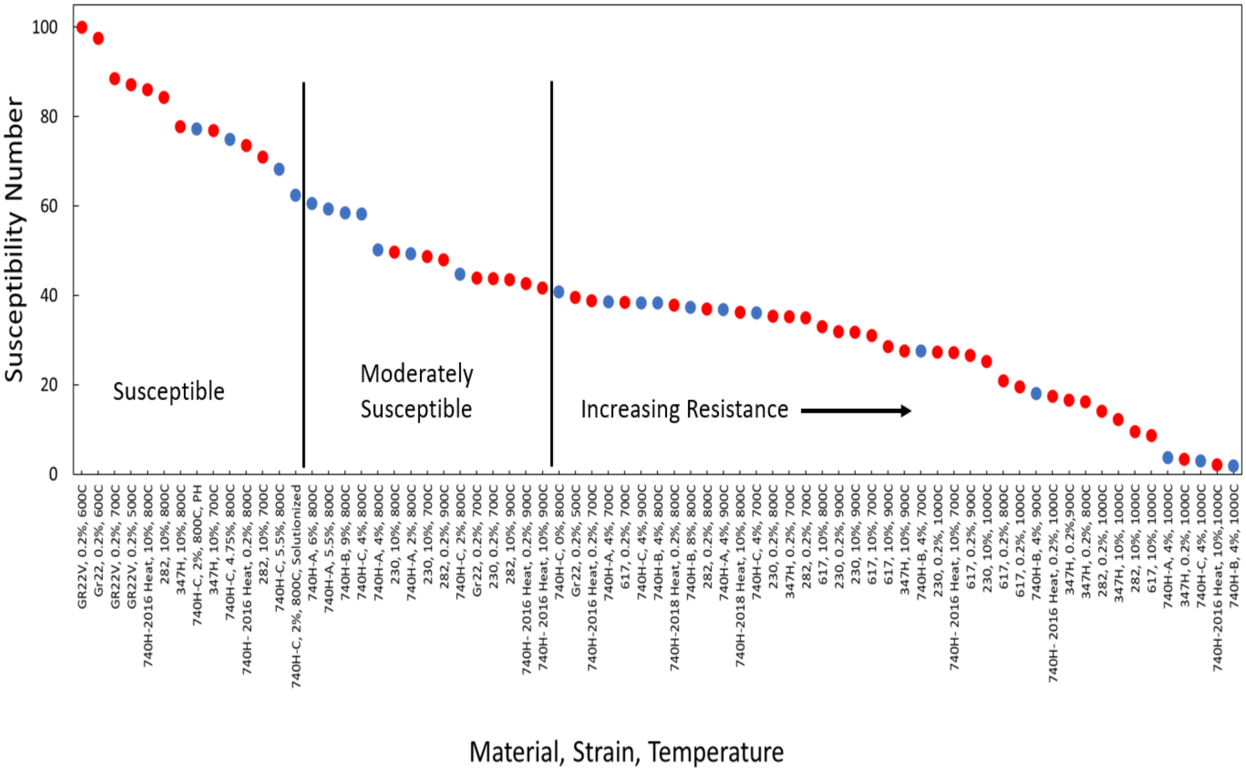

Figure 89. Susceptibility Numbers for different alloys, PWHT temperatures, and plastic strain values. The red data points are from recent SRxC test results conducted for a very wide range of alloys, PWHT temperatures, and plastic strain levels, while the blue data points are for tests conducted in this project.

The SN values from this study, taken together with the results previously described from this project, provide important insights into the SRxC mechanism and factors that affect SRxC susceptibility on alloy 740H. First, it is clear that the formation of soft, precipitate-free zones play a key role in localizing strain along the grain boundary regions and promoting premature failure. This is supported by the presence of stress relief cracks along the precipitate-free zones and the intergranular fracture mode that has localized MVC along the grain boundaries. This fracture mechanism was observed in both the field failures and laboratory SRxC tests. The formation of the precipitate-free zones is, in turn, driven by discontinuous precipitate growth and coarsening that occurs in the presence of a moving boundary. Recent work conducted to understand the reduced creep rupture life of fusion welds in alloy 740H also identified discontinuous coarsening as a contributor to premature failure [14,24]. Since stress relaxation can occur by a creep mechanism at longer PWHT times, it is reasonable to find this mechanism active in PWHT failures as well.

The results presented here also demonstrate that the susceptibility of alloy 740H to stress relief cracking can vary significantly with PWHT temperature, plastic strain, starting microstructural condition, and heat-to-heat variations. The high SRxC susceptibility at 800^{o}C can likely be attributed to the fast precipitation kinetics of γ'. At temperatures below 800^{o}C, the driving force for precipitation is large, but precipitate nucleation and growth is relatively low due to reduced diffusion. The diffusion increases at temperature above 800^{o}C, but the driving force for precipitate nucleation and growth is low. Thus, the γ' precipitate nucleation and growth rate is optimized near 800^{o}C, leading to a concomitant peak in SRxC susceptibility. The stress relaxation results show that significantly more residual stress can be relieved at temperatures above 800^{o}C with the additional benefit of reduced cracking susceptibility. Thus, higher PWHT temperatures may be considered if this is feasible. There may be a practical limitation with this approach with large components, since considerable time at 800^{o}C can still occur during heating to higher PWHT temperatures.

Increased plastic strain clearly increases SRxC susceptibility. As already discussed, plastic strain prior to PWHT reduces the amount of plastic strain available for stress relief and accelerates the precipitation kinetics due to enhanced diffusion, each of which will promote SRxC.

In terms of heat-to-heat variations, Heat C from this study and Heat 2016 from the previous study were each highly susceptible to SRxC. Note that, of the five heats of alloy 740H considered, only these two alloys are in the “Susceptible” range in Figure 89, and these heats only fall within this range when tested at 800^{o}C. The variation in SRxC susceptibility from the different heats can be associated with prior thermal/deformation treatments and/or composition. The influence of plastic strain has already been discussed above and will increase SRxC susceptibility. Thus, differences in SRxC susceptibility observed from the different heats in this work may be attributed to differences in prior deformation history. Similarly, prior thermal treatments may initiate discontinuous precipitation/coarsening prior to PWHT and make SRxC more likely. These factors would require additional characterization of the various heats in the as-received condition and should be considered for future work.

The composition can play a key role when considering SRxC of Ni base alloys, and the Sulfur (S) concentration can be particularly important. For example, studies on Ni have shown that S concentrations as low as 20 ppm can lead to a significant loss of ductility and complete intergranular fracture for commercially pure Ni below 950°C [25]. Previous experiments carried out on Ni doped with S showed a significant drop in ductility at around 700°C for sulfur contents as low as 9 ppm [25]. This effect is generally attributed to S segregation to the grain boundaries that leads to localized embrittlement. At temperatures below 900°C, S will segregate to the grain boundary, which reduces grain boundary coherence [26]. As temperature increases, the equilibrium level of sulfur segregation decreases, and thus at temperatures above 900°C, the effect of S on ductility is reduced [27]. The ductility minimum comes from a balance between diffusion rate and the thermodynamics of equilibrium sulfur segregation. The ductility minimum is alloy specific because changes in composition will affect the S solubility and diffusion rate [28]. However, testing on pure Ni and commercial Ni alloys has shown that significant sulfur segregation is observed at 600-800°C, leading to a ductility minimum in this range [25,29]. It is interesting to note that this may correlate with the low ductility observed for IN740H at 800^{o}C in Figure 63. The deleterious influence of S in alloy 740H and other Ni base alloys is mitigated by the addition of “gettering elements” that can react with S and other tramp elements to prevent them from segregating to the grain boundaries [6,30], and Mg has been shown to be quite effective at reducing embrittlement due to S [31,32]. The amount of Mg is tightly controlled since excess amounts of Mg can form a laves phase (Ni_2Mg) that also causes a loss in hot ductility [31].

In view of these demonstrated effects from Mg and S, the Mg/S ratio may shed some light on the observed differences in SRxC susceptibility of the five heats of IN740H considered in this work. The Mg/S ratio for each heat is shown in Table 13 (based on compositions reported earlier or additional specific analysis). Note that the 2016 and C heats exhibited significantly higher SRxC susceptibility than the remaining alloys and also have lower Mg/S ratios, particularly for the 2016 heat. These variations in Mg and S may account for at least some of the observed differences in SRxC susceptibility between the different heats of alloy 740H and deserve further attention with future work. It should also be noted that an optimally designed melting/remelting practice is necessary to avoid the potentially embrittling effects of excessive retained and uncombined Mg and S and that the processing of different product forms may have a role in the local grain boundary structures and cracking susceptibility. Detailed atomic level studies of trace grain boundary elemental segregation, possibly using high-resolution TEM or atom probe tomography, could be topics for further study.

Table 13. Comparison of Mg and S in the alloy 740H heats subjected to SRxC testing in wt.%

Heat ->	2016	2018	A	B	C
Product Form	Plate	Plate	Tubing	Plate	Extruded Pipe
Mg, wt.%	0.0022	0.0053	0.0062	0.0032	0.0013
S, wt.%	0.0025	0.0004	0.001	0.0005	0.0003
Mg/S	0.88	13.3	6.2	6.4	4.3

Conclusions from Laboratory Testing

Stress relaxation cracking tests (SRxC) were conducted on various heats of alloy 740H to understand the influences of heat-to-heat variations, PWHT temperature, starting condition, and plastic strain. The following conclusions can be drawn from these results:

1. Heats 2016 and C exhibited the highest susceptibility to SRxC cracking. The differences in cracking behavior between the heats may be attributed to differences in starting microstructure (as affected by prior thermal/deformation treatments) and composition.

2. The susceptibility to SRxC is the greatest at a PWHT temperature of 800^{o}C for all heats, which also corresponds to the temperature at which γ' forms at the fastest rate. Segregation of S to the grain boundaries at this temperature may also play a role. This temperature also corresponded to an intergranular fracture mode and minimum in the ductility for the tensile test. Thus, a simple tensile test, combined with fractography, may provide a preliminary indication of SRxC susceptibility

3. The level of residual stress reduction is not very large at 700^{o}C and 800^{o}C, whereas a significant reduction in residual stress occurs when the PWHT temperature is increased to 900^{o}C. Additional work may be warranted to increase the standard PWHT temperature of alloy 740H to temperatures above 800^{o}C if practically feasible realizing that to achieve such high temperatures would require heating through the lower temperature regime.

4. Plastic strain prior to PWHT increases SRxC susceptibility, and the influence of strain varied with each heat. The detrimental effect of plastic strain prior to PWHT is attributed to reduced ductility available for stress relief and acceleration of the γ' precipitation kinetics due to enhanced diffusion.

5. Additional SRxC tests conducted on Heat C demonstrated that SRxC susceptibility is the greatest when tested in the precipitation hardened condition after a hold at 800 ^{o}C to maximize the γ’ content and concomitant hardness. A two minute hold at the peak welding thermal cycle temperature of 1200^{o}C also increased SRxC susceptibility.

6. The SRxC failures in these laboratory tests were associated with the formation of soft, precipitate-free zones and an intergranular fracture mode that exhibited localized microvoid coalescence (MVC) along the grain boundaries. This fracture mechanism was observed in the field failures. The formation of the precipitate-free zones is, in turn, driven by discontinuous precipitate growth and coarsening that occurs during PWHT.

7. Additional microstructural characterization should be conducted on the various heats of alloy 740H in both in the as-received and SRxC-tested condition in order to understand: a) differences in starting microstructural condition (as affected by differences in thermal/deformation treatment) that may influence SRxC susceptibility and b) how differences in local grain boundary chemistry (such as Mg and S levels) may contribute to SRxC susceptibility. High resolution electron microscopy would be instrumental in this endeavor.

3.3 Task 3: Industrial Guidance and Implementation

Background

Cold strain prior to, during or after welding was identified during assessment of field weld failures as a strong contributor to stress relaxation cracking (SRxC) during the post weld stress relief treatment. This cold strain could originate from preparation of surfaces for welding, physical alignment of the joint components or induced stress from constraints, especially on closure welds for large structures. Areas with sharp notches or dimensional variations as well as welding flaws could serve to concentrate stress in critical areas. Observation of recrystallization in heat affected zone of cracked weldments was a strong indication of the localized presence of a high degree of plastic strain. The industrial welding trials discussed below were designed to provide more quantitative data on the effect of cold strain.

Test Plan

Three conditions of strain were investigated (0%, 5% and 10%). The 1-1/2 in parent plate was obtained from commercial scale VIM/ESR heat HT6308JK (same master heat as Heat B tested in Task 2). This plate was band saw split to approximately ¾ in, solution annealed at 2050°F for 30 min and water quenched. They were then milled to 0.500, 0.525 or 0.550 inches thick. The thicker plates were cold rolled on a two-high pilot rolling mill to 0.500 inch to achieve the desired level of cold strain. The final matching plates were 12 x 4 x ½ inch. The joint geometry consisted of a 25° bevel, 1/8 in gap with no land. Backing strips and runout tabs were not used. The joint combinations explored were no strain to no strain, 5% cold strain to no strain, 10% no strain to no strain and 10% strain to 10% strain. The test plates were tack welded to a 740H 1.5" thick strongback as shown in Figure 90.

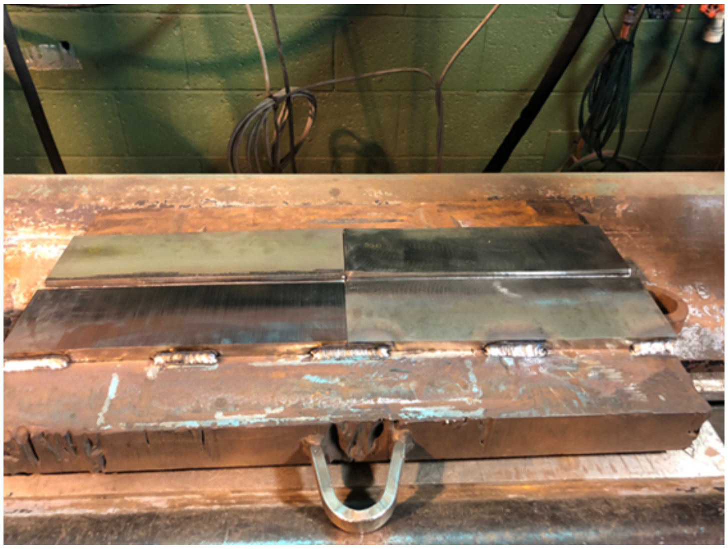

Figure 90. Plates tack welded to strongback

The Gas-Tungsten Arc (GTA) welding pass schedule and parameters are contained in Table 14. Matching filler wire supplied by Special Metals Welding Products Company from Heat HT5502JY was used. The joint consisted of a manual root pass and nominally 9 fill passes including two cap passes. The plate combinations on the strongback were post weld heat treated in a lab-scale box furnace for 4 hours at 1472°F and air cooled. The plates were then removed from the strongback. Some warpage was noted on several plates, which is an indication some unrelaxed residual stress. Photographs of progressive welding stages are shown in Figures 91a-c.

Table 14. Welding Parameters

Parameter	Value	
Base Metal	INCONEL alloy 740H (HT6308JK)	
Filler Metal	INCONEL 740H (HT5502JY) 0.045” Diameter	
Amperage	Manual Root Pass	Automatic Fill Passes
	100	184
Voltage	15	12
Travel Speed (IPM)	4	5
75% Argon/25% Helium Shielding Gas	35 cfh	35 cfh
Filler Metal Speed (IPM)	0.093” @ ~20	60
Pre-Weld Condition	Wrought/Wrought Weldment	2050°F/30min/WQ
	5% Strained/Wrought Weldment	2050°F/30min/WQ Cold-Worked 5%
	10% Strained/Wrought Weldment	2050°F/30min/WQ Cold-Worked 10%
Post-Weld Condition	Fully Restrained Aged: 1472/4hr/AC	

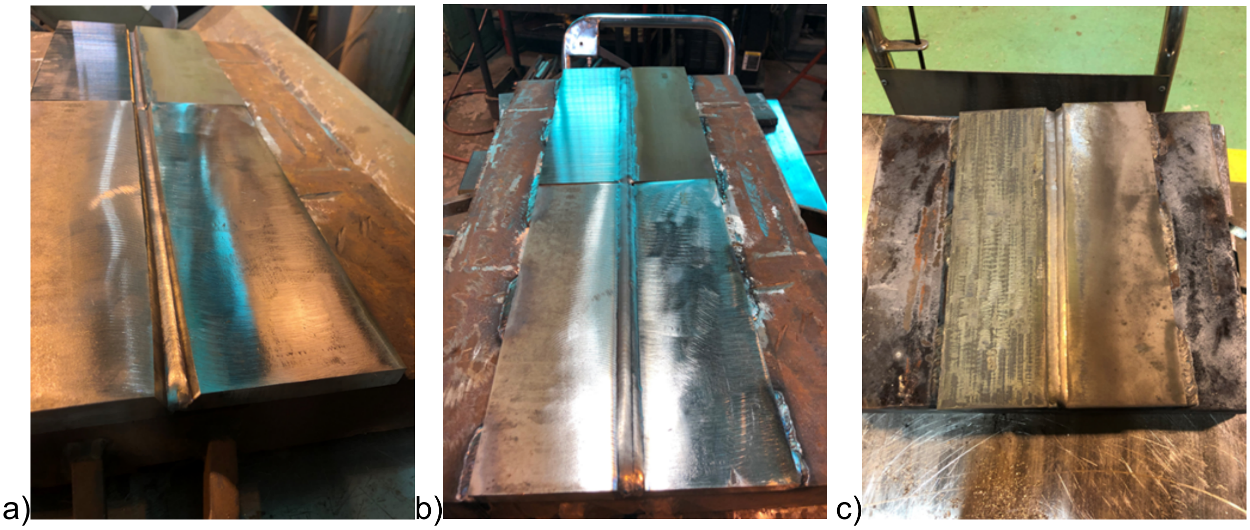

Figure 91. a) Root pass, b) Filler passes, c) Finished weldment

Results

The completed weldments were radiographed at Mistras Group lab in South Point Ohio to their internal procedure 100-RT-001, Rev 20 which is compliant with ASME B&PV Code Section V Article 2. No indications were found. After radiography, transverse sections were cut for metallographic examination. At least four and as many as seven sections were examined for evidence of microcracks or grain boundary creep voids. Apart from scattered minor solidification porosity in the fusion zone, no cracks or voids were seen in any of the weld joint combinations. Representative micrographs from the various plates are shown in Figures 92-95.

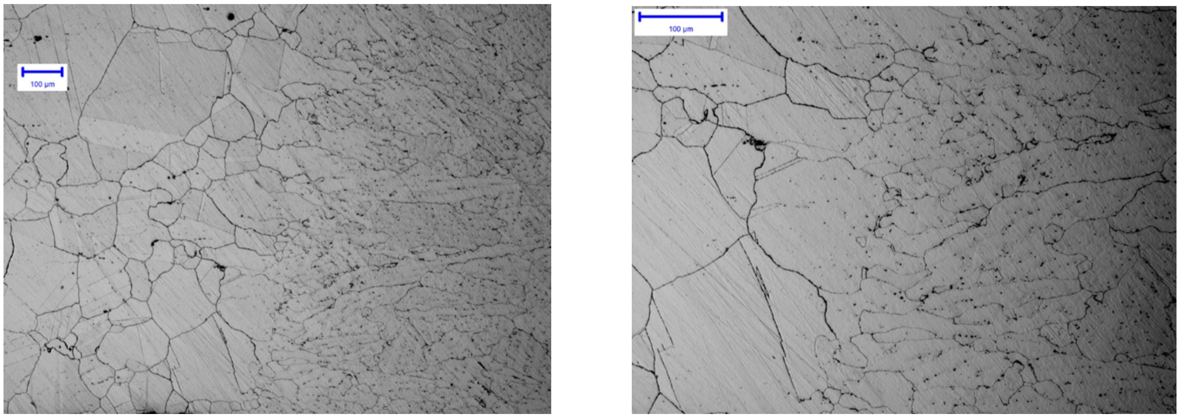

Figure 92. no strain weldment

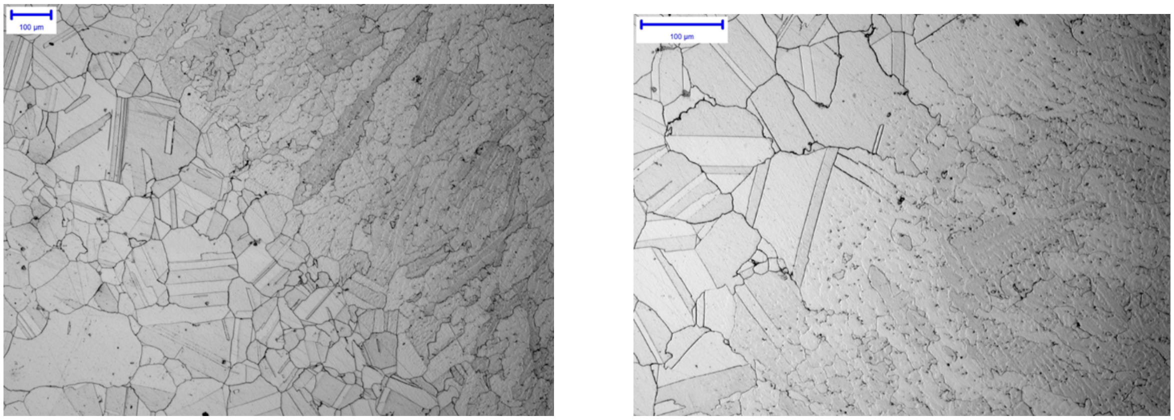

Figure 93. 5% strain to no strain weldment

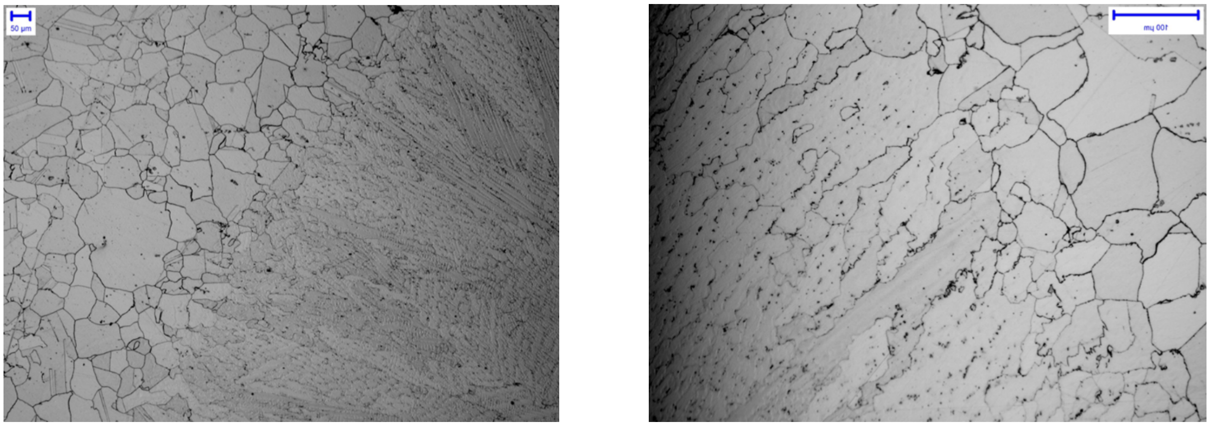

Figure 94. 10% strain to no strain weldment

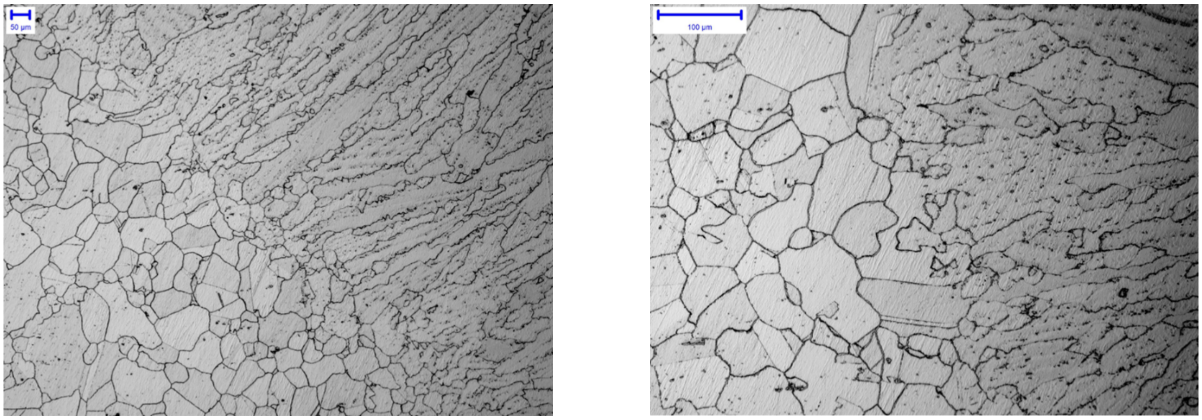

Figure 95. 10% strain to 10% strain weldment.

Discussion

The failure to generate stress relaxation cracking, especially in the 10% strained plates, was unexpected and puzzling. Assessment of failed field welds where cold strain was present, laboratory Gleeble simulations (Task 2) and cold bending studies (Task 1) have all shown that cold strain in alloy 740H promotes cracking in thermal cycles by a strain aging mechanism. In this work there may have been some mitigating factors such as the cold rolling strain being compressive and uniform across the plate thickness. Welding the plates to the strongback was necessary to prevent extreme warpage that was experienced on an initial trial. However, that may have served to keep the residual stress compressive until it was able to relax. Additionally, this heat was found to perform better (moderate susceptibility at the PWHT temperature) in the Task 2 work. This trial did not provide the desired cracking evidence, but the negative result does not negate the premise that localized cold strain in conjunction with geometric stress concentrations and welding flaws are the drivers of stress relief cracking in alloy 740H weldments. The work shows the challenge in creating a universal SRxC laboratory test method.

4. Significant Accomplishments and Conclusions:

The project made significant progress in the understanding of practical issues in applying alloy 740H in advanced demonstration/power plant applications. In only 18months, the project gathered a community of alloy 740H users, collected hard-to-obtain field samples of failures, conducted a detailed characterization study, produced and tested over 50 laboratory samples based on a targeted assessment of variables, disseminated the learnings to the scientific and engineering community, and produced an industry first-of-a-kind guidance document for end user application. The project timeline was originally 12 months, but was extended to 18 months due to the project being successful in engaging industry which allowed more samples from the field to be evaluated.

Overall, the following conclusions can be made:

- Task 1: SRxC field failures:
    - 3 unique instances of cracking were assessed in detail confirming failure by the SRxC mechanism in weldments during PWHT
        - Cracks were intergranular with minimal branching and were only identified after PWHT
    - Overall observations suggested stress state had a significant influence on crack initiation:
        - Cracking was in weldments but was not restricted to one unique weldment zone (BM, HAZ, WM)
        - High strain was observed in microstructures near crack initiation (channeling contrast, recrystallization)
        - Cracks initiated at stress concentrations
    - Additional unique microstructural features associated with SRxC in 740H included:
        - Precipitate denuded zones at GBs ahead of crack tips
        - Evidence of cavitation damage at denuded zones / precipitate free zones (PFZs) ahead of secondary crack tips
        - Discontinuous precipitation with elongated precipitates within denuded zones
        - No evidence of GB denuded zones further away from main crack
        - Intergranular and narrow crack morphology with very little branching
        - Evidence of oxide scale within the cracks
        - Advanced TEM characterization confirmed the mechanism for PFZ formation
    - Table 15 provides a summary of the observations in comparison with typical nickel-based alloy cracking mechanisms
    - An expert assessment of the finding was used in conjunction with available literature data to plan focused laboratory testing

- Task 2: Laboratory testing of three heat of alloy 740H and review of previous testing found the following:

  - A laboratory-based test method reproduced the formation of PFZs in alloy 740H which for some heats and test conditions formed relaxation cracks during simulated PWHT cycles
  - 3 unique heats were tests and when combined with previous research found two heats to be more susceptible to SRxC: possible role of chemistry (S, Mg, …) and product form manufacture
  - SRxC susceptibility is greatest at 800^{o}C for all heats due to γ' precipitation kinetics
  - Stress relaxation is greater at 900^{o}C which suggests alternative PWHT cycles may reduce risk of SRxC
  - Plastic strain prior to PWHT increases SRxC susceptibility which is in direct support of field findings
  - Solution annealed material may be more resistant SRxC compared to the age hardened condition
- Overall end user experience with alloy 740H has been positive with 1,000's of welds and many tons of components produced. Based on the experience, SRxC during PWHT appears to be the most challenging damage mechanism to address, and based on the findings from this work and the produced guideline, there are a number of practical steps end-users, component suppliers, and fabricators can take to mitigate the risks associated with SRxC.

Table 15. Characteristics and observations considered in the determination of the SRxC mechanism for alloy 740H

	Hot Cracking		Stress Relaxation Cracking (Strain Age Cracking)		Environmentally Assisted Cracking		740H Observations		
Subcategories	*Solidification Cracking*	*Liquation Cracking*	*Fabrication Related*	*Service Related*	*Stress Assisted Grain Boundary Oxidation (SAGBO)*	*Stress corrosion cracking (SCC)*	Demo #1:	Demo #2	Demo #3
Cracking Location	WM	FL/HAZ	WM, FL, HAZ, BM	HAZ	HAZ/BM	WM, HAZ, BM	Weld Toe with variable propagation: **HAZ/FL/WM**	**WM, HAZ, BM**	**WM, BM** (Tube and Body)
Timing	During Cooling of Welding Cycle	During Cooling of Welding Cycle	During PWHT	During High-Temperature Service	During Service	During Service or corrosive exposure after welding	NDE prior to heat-treatment did not find cracks, cracking and full thickness **cracks identified after PWHT**		
Requires	Welding	Welding	Welding or Imposition of Strain followed by high-temperature exposure		High-temperature exposure to oxygen containing environment	Exposure to environment containing halides (Cl, Br, etc.), S, or other corrosive species [Low/intermediate temperature]	Circumferential orientation in tube butt **welds**	Axial orientation in pipe girth **welds**	Radial orientation in tube to block socket **welds** and axial along tubes
Source of stress/strain	Contraction from cooling	Contraction from cooling	Localized relaxation of welding residual stress	Relaxation of Welding residual stress and/or thermal cycling in service	Operational stresses	Multiple (welding residual stresses, service induced)	Evidence for **highly localized strain at toe of welds, variable workmanship led to stress concentrations** (SEM showed strong channeling contrast + recrystallization at crack initiation locations)		
Crack Morphology	Interdendritic cracking	Intergranular	Intergranular cracking, minimal branching		Intergranular	Intergranular, branching	**Intergranular, minimal branching**		**Intergranular**, multiple individual cracks (**no branching**)
Crack Initiation	Within WM	Within HAZ	Generally at a surface/region of stress concentration	various	Surface exposed to oxygen and high tensile strain	Surface exposed to corrosive species	**Weld toe near stress concentration on ID**	**ID initiated**; location not determined	**ID initiated**, multiple cracks initiated at weld toes and weld HAZs
Additional crack observations		Often limited to small number of grains in HAZ close to FL	Cavitation ahead of crack tips, oxide scales observed inside cracks		Oxidation within crack and ahead of crack tip	corrosive species within the crack	Oxide in cracks likely from heat-treatment cycle , **cavitation ahead of crack tips**		
Typical Microstructural features	Weld metal segregation	liquation of a few grains	Rapid precipitation / hardening (often associated with γ' precipitation)	Localized hardening of the microstructure (often associated with fine carbide or γ' precipitation)	Generally high strength lower ductility superalloys	selective corrosion of grain boundaries from main crack(s)	Cavitation ahead of crack tips occurred in **PFZs (denuded of gamma prime), CZ leading to PFZs found near crack initiation sites but not identified away from failure.** Fine gamma precipitates in matrix surround grain boundaries		

5. Path Forward:

This project convened for the first time an industrial users group for alloy 740H to share experiences and discuss ongoing development work. Such a forum is critical to understanding the application of the newly developed guideline for alloy 740H and providing feedback. EPRI materials guidelines are ‘living documents’ which can be improved with user feedback and new scientific learnings. EPRI plans to continue to engage this community as well as other end-users through a number of forums including: EPRI’s Materials & Repair program advisory structure which as over 30 utilities and companies focused on materials, welding, life management, and repair topics for energy applications; EPRI supported Advanced Energy Systems supply chain workshops to engage designers, fabricators, material suppliers, component manufacturers, and advanced manufacturing companies for future power generation technologies; and EPRI’s advances in materials for power plant conferences.

EPRI will continue to add to its database of failure investigations and has recently started, based on the learning of this work, a new failure analysis for another 740H field cracking observation. Areas of potential future study beyond the scope of this project which have been identified for alloy 740H and similar alloys include the following:

- Post-exposure materials evaluations from advanced CSP and sCO_2 power cycle demonstrations projects to ‘close-the-loop’ on the application of new materials (e.g. alloy 740H) and/or existing materials to new extreme environment applications. This should ideally involve both failure analysis as well as documenting successful applications to build end-user confidence in new technologies and the required materials of construction.
- Exploration of alternative post-weld heat-treatment (PWHT) approaches (temperatures and cycles) to minimize risk of SRxC in alloy 740H without negatively impacting the high-temperature performance of weldments.
- Welding repair development for serviced exposed alloy 740H and similar alloys.
- Modeling and characterization of residual stresses in alloy 740H and other high-temperature nickel-based alloys to develop improved guidance for reducing cracking risks for these alloys through joint design and possibly automated welding.
- Review and validation of non-destructive evaluation (NDE) methods for identifying SRxC and other potential service-related defects in support of long-term management of nickel-based alloys for advanced applications.
- Further detailed characterization of selected heats tested in this work at the nano-scale to evaluate the heat-to-heat variability in the observed laboratory SRxC testing. The focus of this work should include microstructure and grain boundary segregation (possible effects of Mg and S on cracking) using atomic resolution TEM and/or atom probe tomography (APT). Limited interrupted Gleeble™ studies (where samples are not pulled to failure) may be needed to validate results.

6. Products:

Peer Reviewed Conference Paper [1 complete, 2 in-progress]

	Conference Publications (include only if accepted by organizer)								
	Full Author List (same naming convention as Journal Articles)	**"Article Title"**	**Paper Number**	**Conference/Proceedings Title**	**Conference Location**	**Date (MM/DD/YYYY;** First day if multiple days)	**CD Rom Volume or Volume, pp. (##-##)**	**DOI, if applicable**	**ISBN**
E	John Shingledecker, John Siefert, Tapasvi Lolla, John Dupont, John DeBarbadillo, Ronnie Gollihue ,	Factors Influencing Propensity for Stress Relaxation Cracking in Inconel ® Alloy 740H® and Practical Guidance for Applications	Accepted for publication	*Superalloy 718 and Derivatives 2023 Conference*	Pittsburgh, Pennsylvania	05/14/23			

**The EPRI team is in the process of developing two additional peer reviewed journal publications focused on the characterization of failures and the thermo-mechanical laboratory results*

Conference Presentations [2 completed]

	Conference Presentations						
	Full Author List (same naming convention as Journal Articles)	**"Paper Title"**	**Paper Number**	**Session/Symposium/Conference**	**Conference Location (of the format City, State_Acronym)**	**Date (MM/DD/YYYY; First day if multiple days)**	**DOI, if applicable**
F	J. Shingledecker, T. Lolla, J. Siefert, J. Dupont, J. deBarbadillo, R. Gollihue	PRACTICAL APPLICATION AND THE DEVELOPMENT OF AN INDUSTRY SPECIFICATION FOR INCONEL ALLOY 740H		Session 6: Qualification Schemes / Advances in Welding and Additive Manufacturing Research (AWAMR)	Virtual	June 13-16, 2022	
	T. Lolla, J. Shingledecker, J. Siefert, G. West	METALLURGICAL OBSERVATIONS OF STRESS RELAXATION CRACKING IN AUSTENITIC MATERIALS		Session 9: Weldability Studies / Advances in Welding and Additive Manufacturing Research (AWAMR)	Virtual	June 13-16, 2022	

Workshops or other events [2 completed]

	Workshops and Other In-Person Events Held					
	Title of Event	**Start Date of Event (MM/DD/YYYY)**	**End Date of Event (MM/DD/YYYY)**	**Location of Event** (City, 2-Letter State Abbreviation, e.g. Cleveland, OH)	**Event URL, if applicable**	**Stakeholder Types Engaged** (e.g. Utilities; PUCs; etc.)
K	DOE sCO2 Cross-Cutting Team Workshop	3/xx/2020	3/xx/2020	Virtual	https://netl.doe.gov/sites/default/	Multiple DOE program offices, national labs, end users
	Meeting on 740H Fabrication and Welding Experience	12/13/21	12/13/21	Virtual		Manufacturers, utilities, technology developers, field fabricators SMC, EPRI, DOE (muli-office)

Publicly Available Guideline [1 – in publication]

	Other Noteworthy Products - EPRI Technical Report					
	Title	**Reference**				
M	Technical Requirements for Procurement of Components Fabricated from INCONEL ® Alloy 740H®.	EPRI, Palo Alto, CA: 2022. 3002025494.				

Technical Assistance

	Technical Assistance (TA) Outputs					
	TA Recipient Name (of the format FirstName LastName, e.g. John Smith)	**Estimated Total Hours Spent Providing TA**	**Start Date of TA (MM/DD/YYYY)**	**End Date of TA (even if same as Start Date; MM/DD/YYYY)**	**Primary TA Topic**	**Primary TA Topic Text, if Other selected**
N	Echogen 740H Cracking Investigation	4 hours spent in discussions with Echogen in addition to the technical work which is part of the project workshope			Other Item Not Listed (please provide descriptive text in next column)	Decision making on corrective action for fabricating new joint geometry

7. Project Team and Roles:

EPRI

- John Shingledecker, Ph.D., Principal Investigator: Overall project management and technical project management, lead industry engagement, lead guideline drafting [Subtask 1.1, 1.4]
- Tapasvi Lolla Ph.D.: Lead failure investigations, materials management, and advanced characterization [Subtasks 1.2, 1.3, 2.1]
- John Siefert, Ph.D.: Technical project support and guidance, guideline authorship [Subtask 1.4]

John Dupont Metallurgical Consulting (at Lehigh University)

- John Dupont, Ph.D.,: Conduct laboratory based testing and analysis, overall project technical guidance, support advanced characterization activities [Task 2]

Special Metals Corporation

- John (Jack) deBarbadillo, Ph.D.: Industrial guidance [Subtask 3.1]
- Ronald (Ronnie) Gollihue: Field welding guidance, material supply, weld testing [Task 3]

8. References:

[1] .J. deBarbadillo, “INCONEL alloy 740H”, Materials for Ultra-Supercritical and Advanced Ultra-Supercritical Power Plants, ed. A. Di Gianfrancisco, Elsevier, London, 2017, 469-506. ISBN: 978-08-100552-1

[2] *Improving Economics of Generation 3 CSP System Components Through Fabrication and Application of High Temperature Nickel-Based Alloys*. DE-EE0008367

[3] John Shingledecker, John deBarbadillo, Ronnie Gollihue, Eeva Griscom, Dan Purdy, Alex Bridges. “Development and Performance of INCONEL® Alloy 740H® Seam-Welded Piping” *submitted to the International Journal of Pressure Vessels and Piping*

[4] John A. Siefert, Cara Libby, John Shingledecker. “Concentrating solar power (CSP) power cycle improvements through application of advanced materials.” AIP Conf. Proc. 1734, 070030 (2016). http://dx.doi.org/10.1063/1.4949177

[5] Design Guidance for High Temperature Concentrating Solar Power Components, ANL-20/03

[6] J. Dupont, J. C. Lippold and S. D. Keiser: ‘Welding metallurgy and weldability of nickel base superalloys’; 2009, New York, John Wiley and Sons Inc.

[7] S.A. David, J.A. Siefert, J.N. Dupont, J.P. Shingledecker. “Weldability and weld performance of candidate nickel base superalloys for advanced ultrasupercritical fossil power plants part I: fundamentals.” Science and Technology of Welding and Joining. Vol. 20, Issue 7 (October 2015), pp. 532-552.

[8] John P. Shingledecker, John A. Siefert. “Age Hardenable Nickel-based Alloy Developments and Research for New High Temperature Power Cycles.” In Ott E. et al. (eds) Proceedings of the 9th International Symposium on Superalloy 718 & Derivatives: Energy, Aerospace, and Industrial Applications, © 2018 The Minerals, Metals & Materials Series. Springer, Cham. https://doi.org/10.1007/978-3-319-89480-5_1

[9] J.A. Siefert, J.P. Shingledecker, J.N. Dupont, S.A. David. “Weldability and weld performance of candidate nickel base superalloys for advanced ultrasupercritical fossil power plants part II: weldability and cross-weld creep performance.” Science and Technology of Welding and Joining. Available online October 2015. http://dx.doi.org/10.1179/1362171815Y.0000000094

[10] John deBarbadillo, Ronald Gollihue, Brian Baker. “Recent Development in Welding 740H” DOE-NETL. available at: https://netl.doe.gov/sites/default/files/netl-file/21WELD_Debarbadillo.pdf

[11] J.A. Siefert, J.P Shingledecker and T. Lolla, “Power Generation Industry Experience: Stress Relaxation Cracking (SRxC) and Strain Induced Precipitation Hardening (SIPH) Failures,” presented at the DOE sCO2 Cross-Cutting Team Workshop, March 2020. Available at: https://netl.doe.gov/sites/default/files/netl-file/21WELD_Shingledecker.pdf

[12] John Shingledecker, John Siefert, Tapasvi Lolla, Matthew Hauth, Mark Stevens, Trenton Cook. “Investigation of Weldment Cracking During Fabrication of a 700^{o}C Fired sCO2 Heater.” *The 7th International Supercritical CO2 Power Cycles Symposium.*

February 21 – 24, 2022, San Antonio, Texas. Paper #170. Available at: https://sco2symposium.com/proceedings2022/170-paper.pdf

[13] "Case 2702-3." BPVC Code Cases: Boilers and Pressure Vessels. BPVC-CC-BPV-2016, ASME (2016).

[14] Bechetti, D.H., Dupont, J.N., Watanabe, M. et al. Characterization of Discontinuous Coarsening Reaction Products in INCONEL® Alloy 740H® Fusion Welds. Metall Mater Trans A 48, 1727–1743 (2017). https://doi.org/10.1007/s11661-016-3952-2

[15] Bechetti, D.H., DuPont, J.N., de Barbadillo, J.J. et al. Microstructural Evolution of INCONEL® Alloy 740H® Fusion Welds During Creep. Metall Mater Trans A 46, 739–755 (2015). https://doi.org/10.1007/s11661-014-2682-6

[16] R. Kant, J. DuPont. "Stress Relief Cracking Susceptibility in High-Temperature Alloys." Welding Journal, AWS, February 2019, 29-s. https://doi.org/10.29391/2019.98.003

[17] Technical Requirements for Procurement of Components Fabricated from INCONEL ® Alloy 740H®. EPRI, Palo Alto, CA: 2022. 3002025494. *In Publication*

[18] A Practical Guide on Welding INCONEL® Alloy 740H®. Special Metals Brochure

[19] A. Yilmaz: Sci. Technol. Adv. Mater., DOI:10.1088/1468-6996/12/6/063001.

[20] X. Wang, G. Han, C. Cui, S. Guan, J. Li, G. Hou, Y. Zhou, and X. Sun, J. Mater. Sci. Technol., 2019, vol. 35, pp. 84–7

[21] R. Zhang, C. Tian, C. Cui, Y. Zhou, and X. Sun: J. Alloys Compd., 2020, vol. 818, p. 152863.

[22] Y. Cai, C. Tian, S. Fu, G. Han, C. Cui, and Q. Zhang: Mater. Sci. Eng. A, 2015, vol. 638, pp. 314–21.

[23] Jonah Duch, PhD Dissertation, Lehigh University, December, 2021.

[24] D.H. Bechetti, J.N. DuPont, J.A. Siefert, and J.P. Shingledecker: Metallurgical and Materials Transactions A, 2016, Vol. 47, p. 4502.

[25] R.A. Mulford: Treatise Mater. Sci. Technol., 1983, vol. 25, pp. 1–19.

[26] T. Hu, S. Yang, N. Zhou, Y. Zhang, and J. Luo: Nat. Commun., DOI:10.1038/s41467-018-05070-2.

[27] D. McLean: Grain Boundaries in Metals, Clarendon Press, Oxford, 1957.

[28] R.A. Mulford: Metall. Trans. A, Phys. Metall. Mater. Sci., 1983, vol. 14 A, pp. 865–70.

[29] R.T. Holt and W. Wallace: Int. Met. Rev., 1976, vol. 21, pp. 1–24.

[30] F. Turner: Met. Technol., 1984, vol. 11, pp. 446–52.

[31] J.J. Debarbadillo: Superalloys, 1976, pp. 95-107.

[32] K. Banerjee: Mater. Sci. Appl., 2011, vol. 02, pp. 1243–55.

Appendix: Additional characterization images

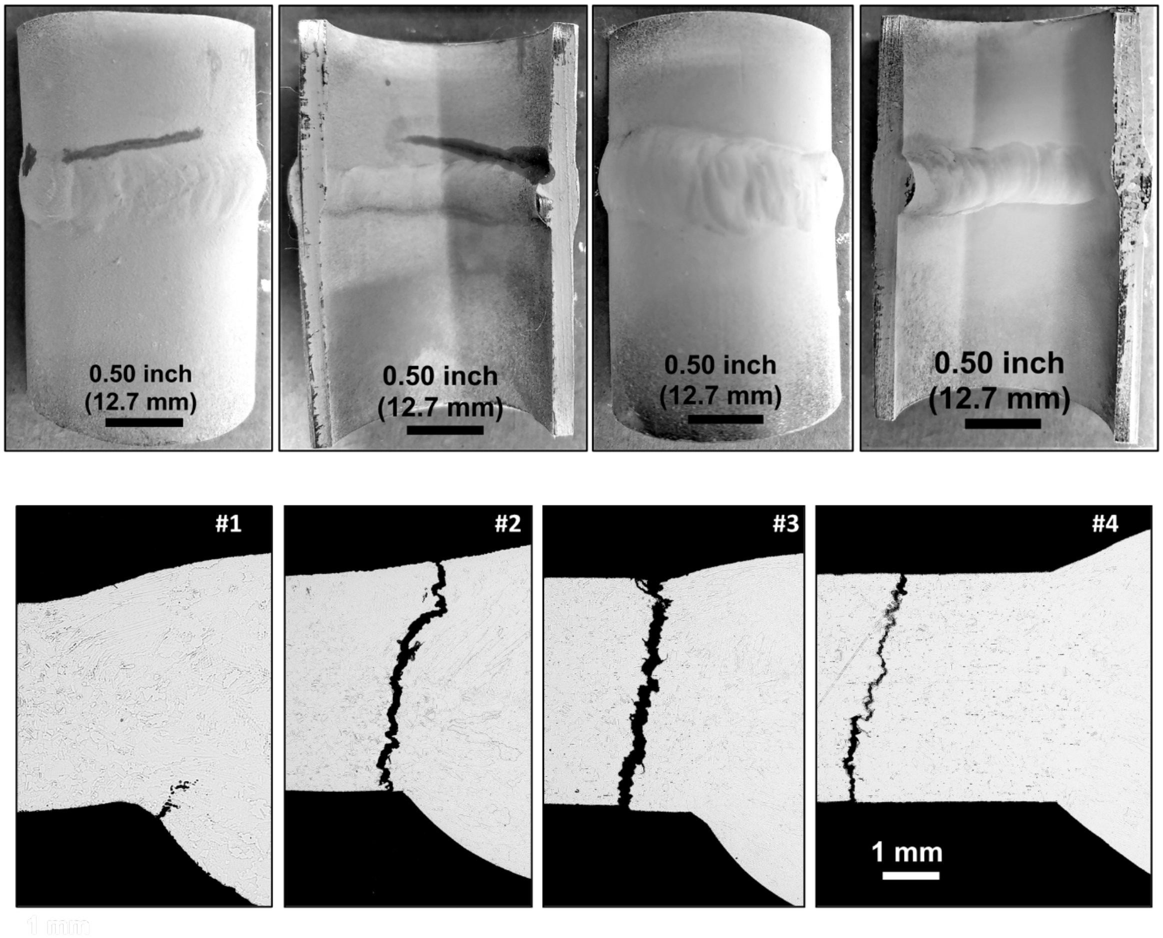

Figure A1: Images of LP testing showing the ID and OD surfaces of split tubes along with crack and polished cross section images of crack showing crack propagation characteristics in sample Row 14 Weld 25

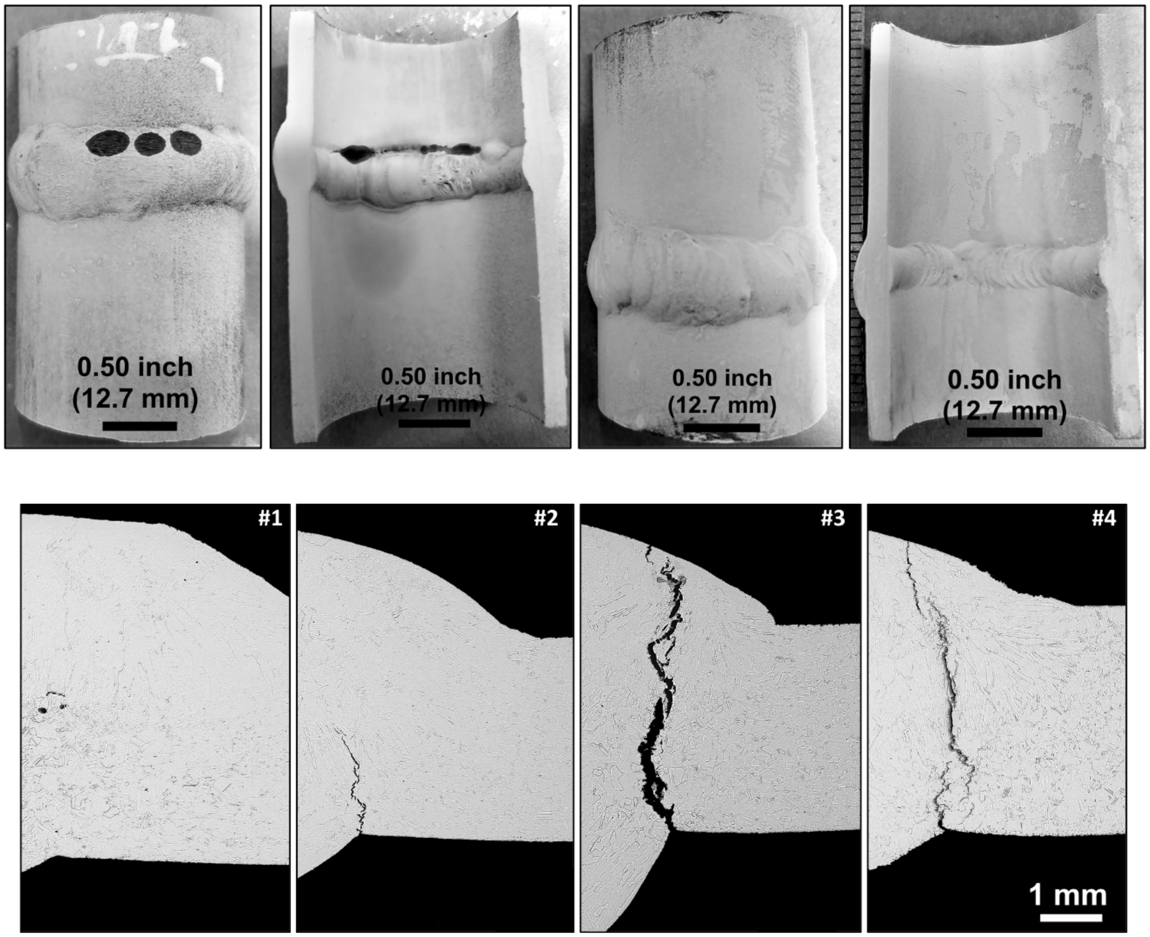

Figure A2: Images of LP testing showing the ID and OD surfaces of split tubes along with crack and polished cross section images of crack showing crack propagation characteristics in sample Row 13 Weld 34

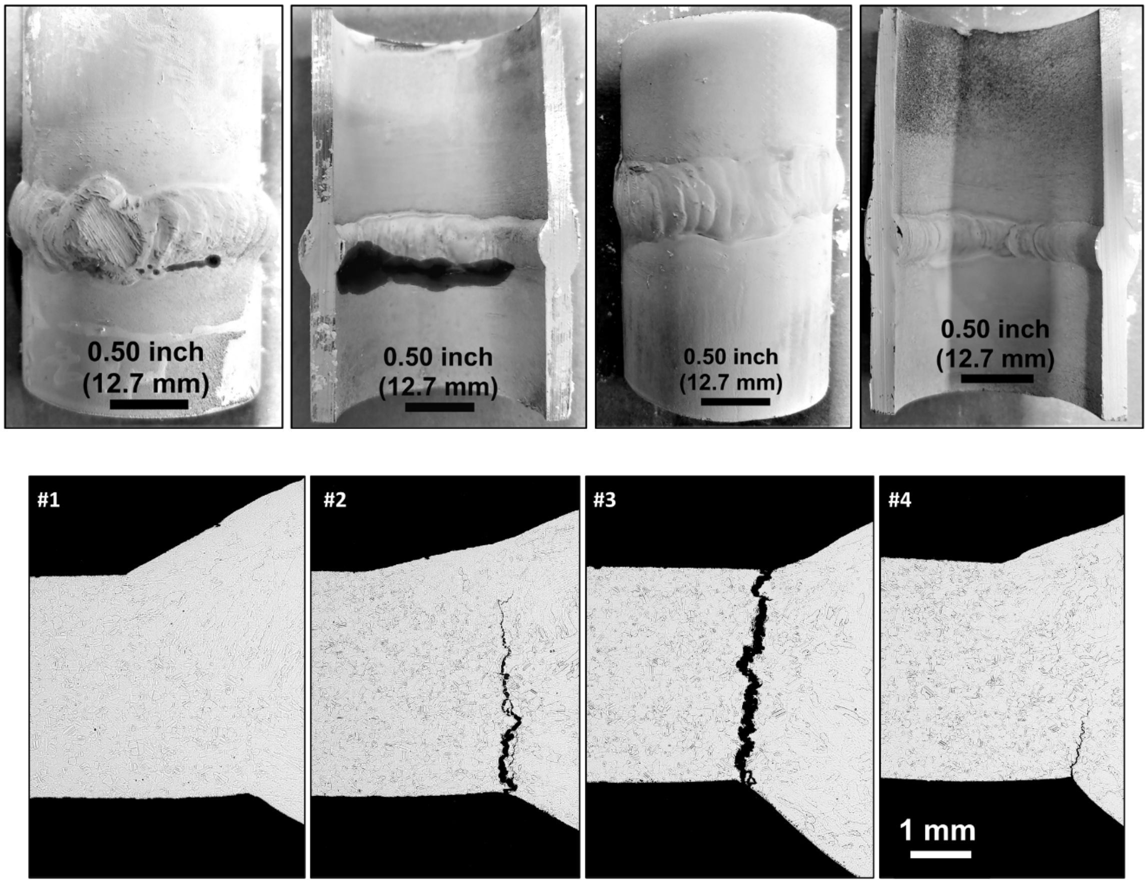

Figure A3: Images of LP testing showing the ID and OD surfaces of split tubes along with crack and polished cross section images of crack showing crack propagation characteristics in sample Row 13 Weld 4

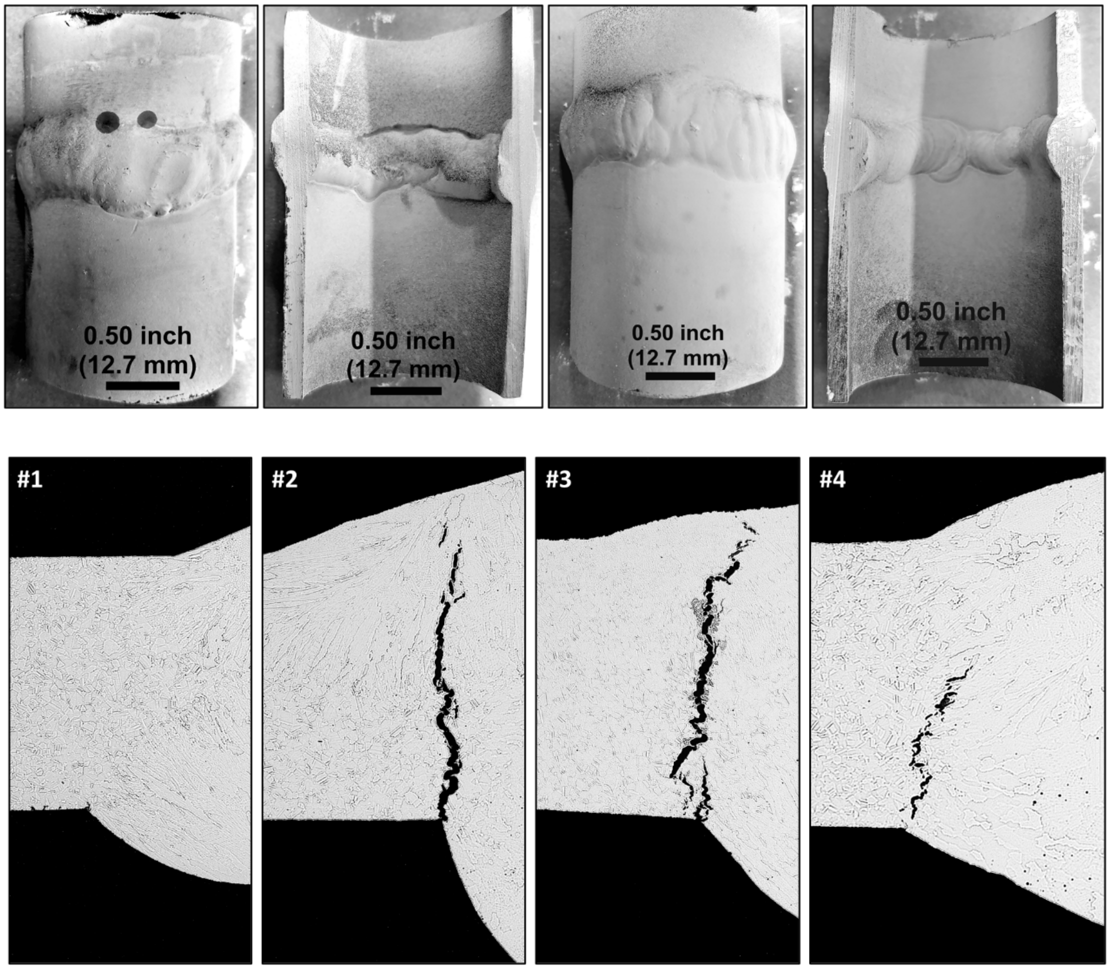

Figure A4: Images of LP testing showing the ID and OD surfaces of split tubes along with crack and polished cross section images of crack showing crack propagation characteristics in sample Row 13 Weld 20

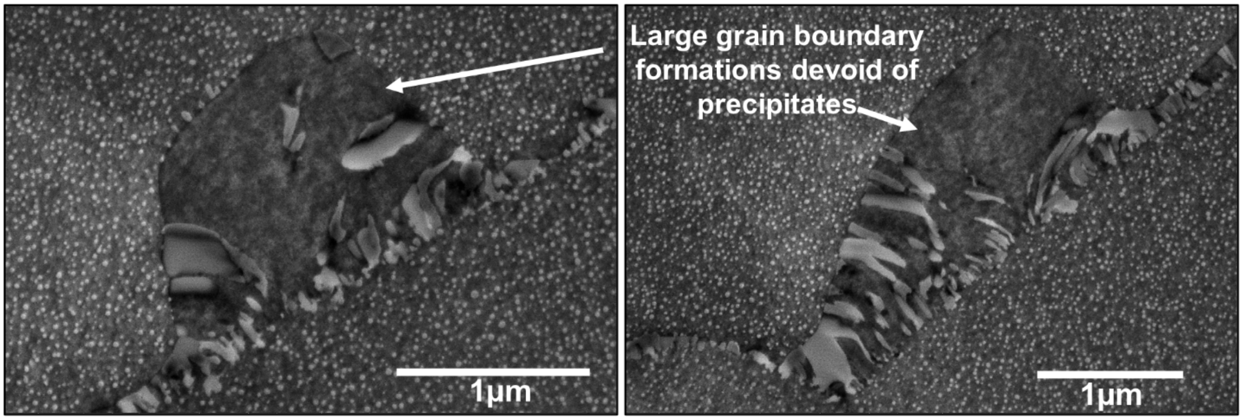

Figure A5: Images showing examples of large grain boundary denuded zones with discontinuous coarsening.

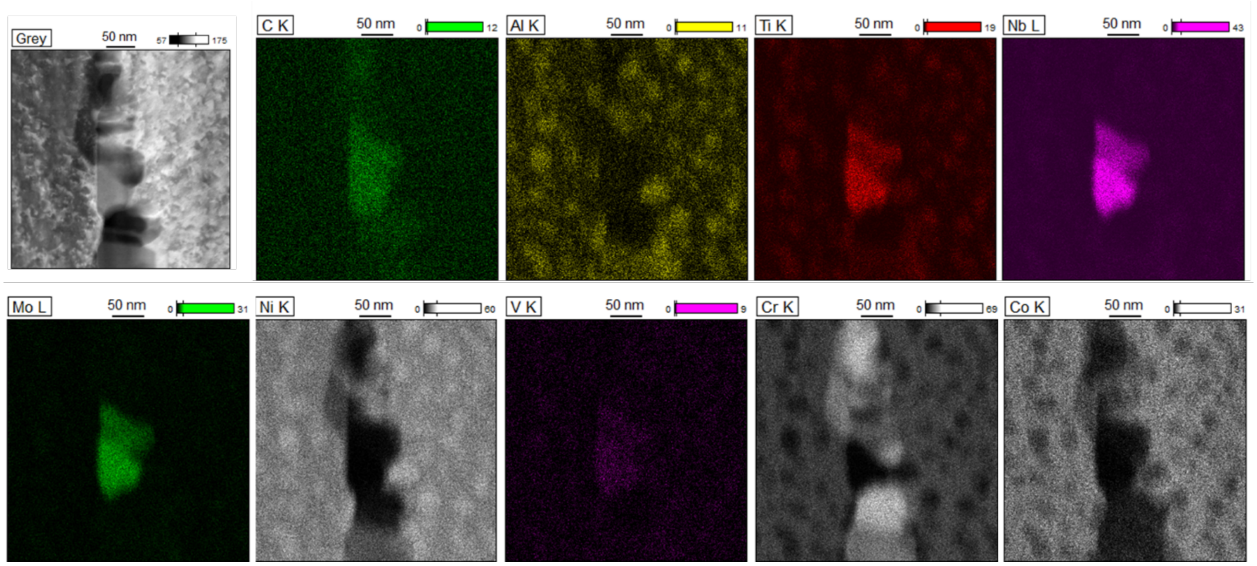

Figure A6: Results showing the distribution of various alloying elements from STEM EDS mapping done at a grain boundary region that is farther away from cracking site of sample Row 14 Weld 25 showing complete grain boundary coverage by precipitates.

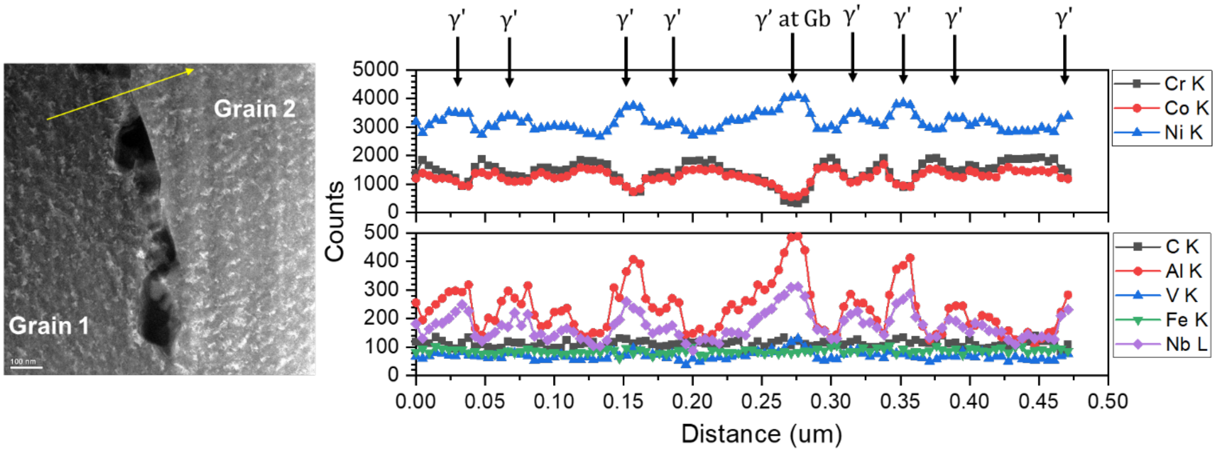

Figure A7: STEM-EDS line scan made across a grain boundary precipitate feature in a TEM sample obtained from a region farther away from location of crack in sample Row 14 Weld 25.

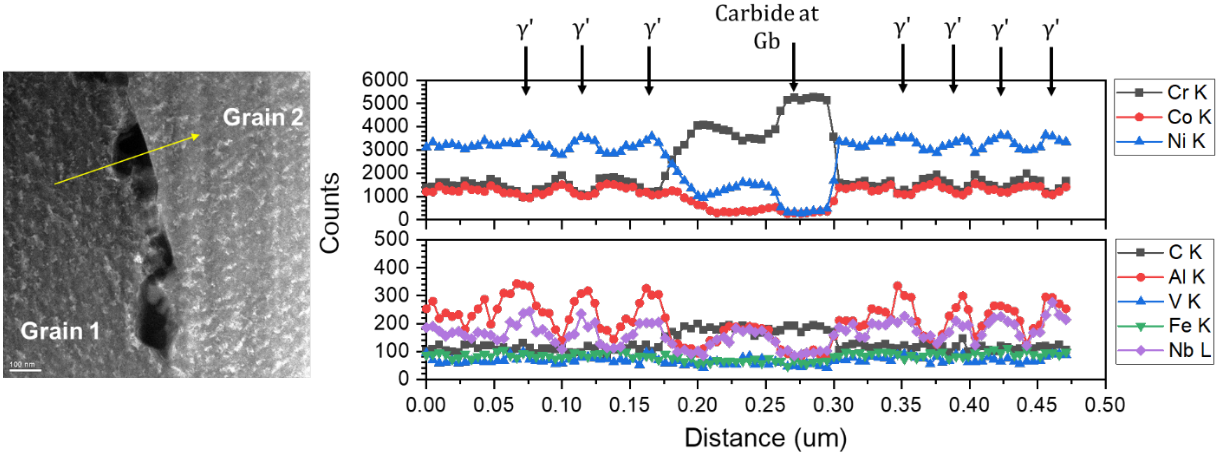

Figure A8: STEM-EDS line scan made across a grain boundary precipitate feature in a TEM sample obtained from a region farther away from location of crack in sample Row 14 Weld 25.

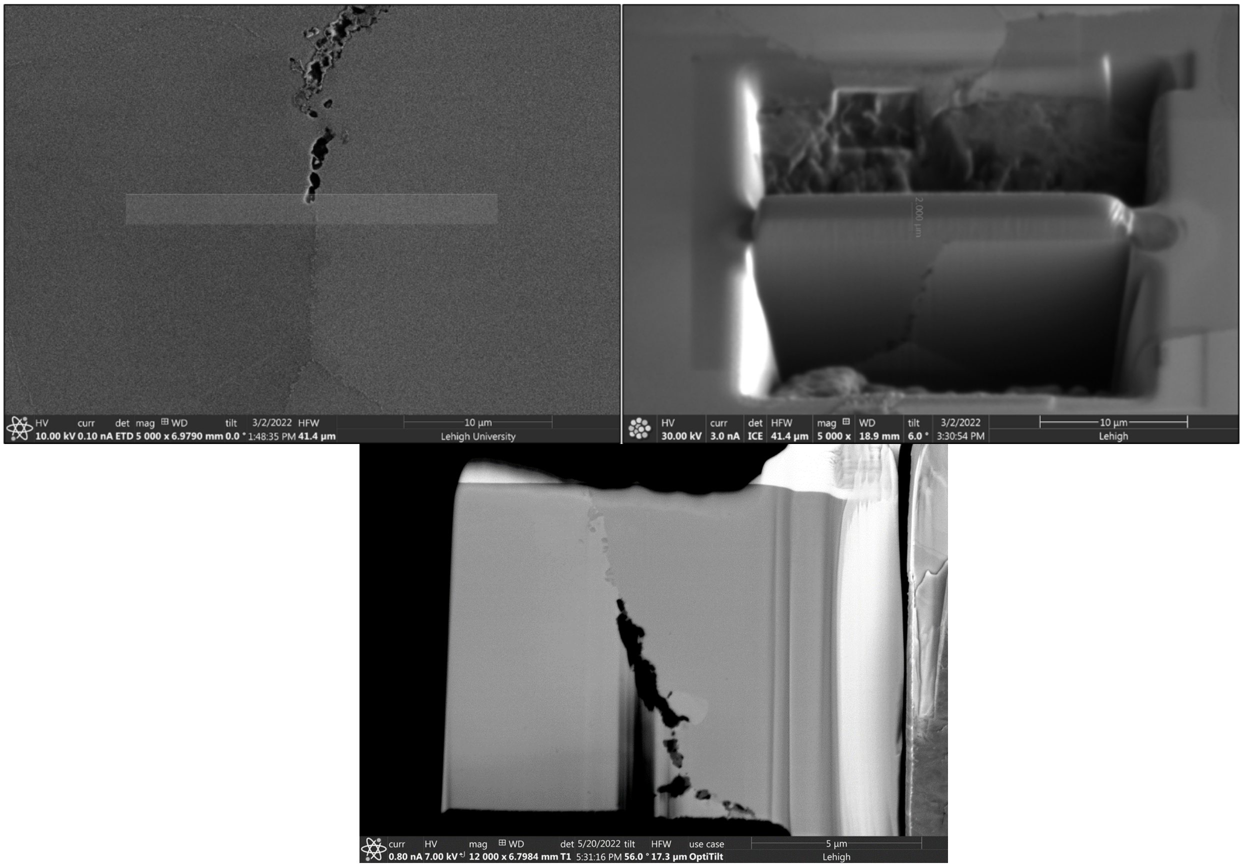

Figure A9: SEM images showing the extraction of a TEM sample for analysis from a grain boundary region immediately ahead of an intergranular crack.

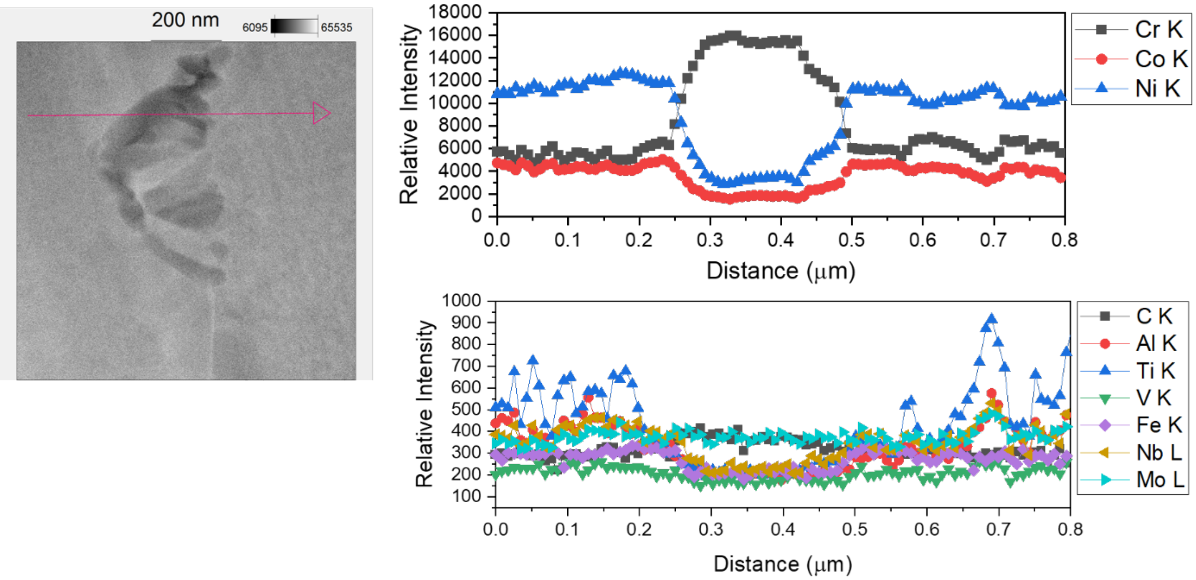

Figure A10: STEM-EDS line scan made across precipitate features in the TEM sample showing in Figure A7.

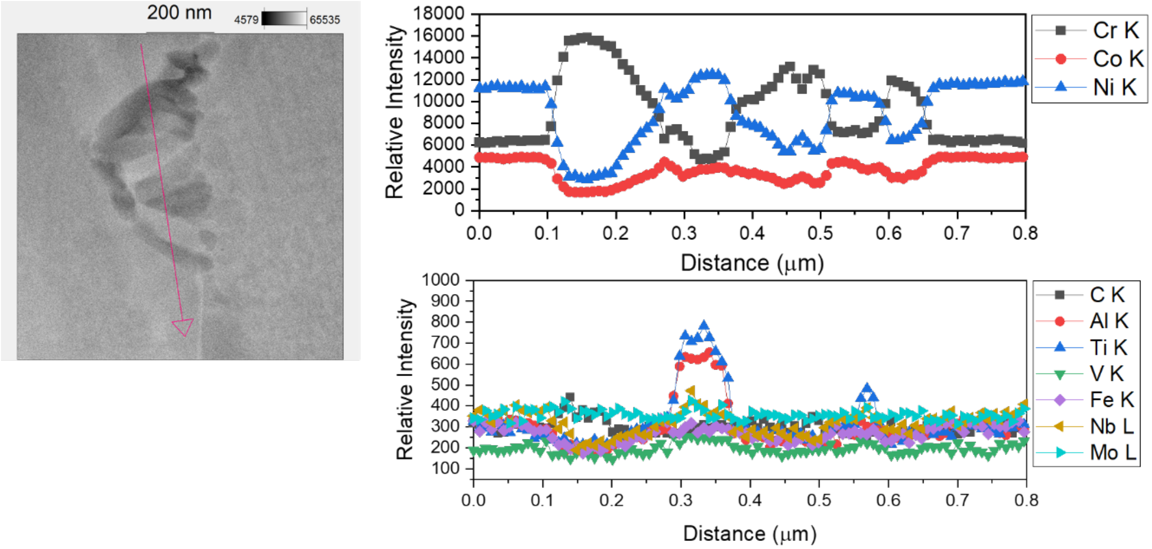

Figure A11: STEM-EDS line scan made across precipitate features in the TEM sample showing in Figure A7.

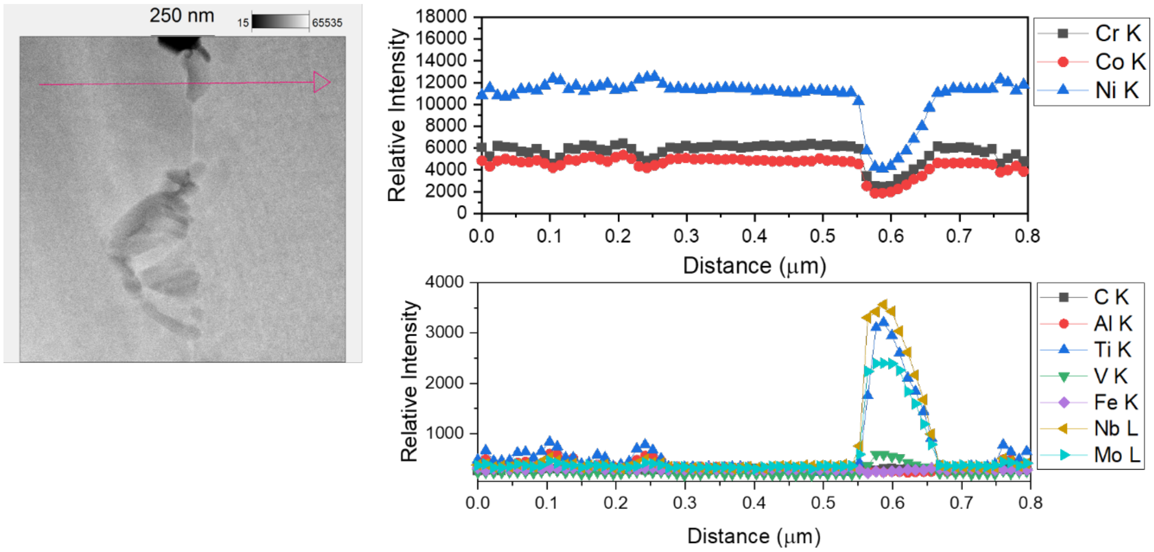

Figure A12: STEM-EDS line scan made across precipitate features in the TEM sample showing in Figure A7.

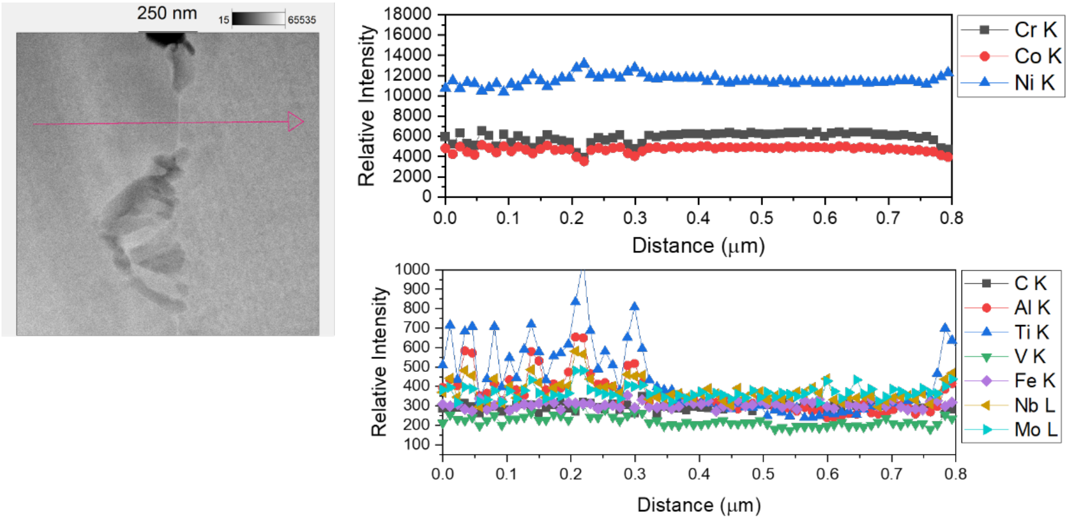

Figure A13: STEM-EDS line scan made across precipitate features in the TEM sample showing in Figure A7.

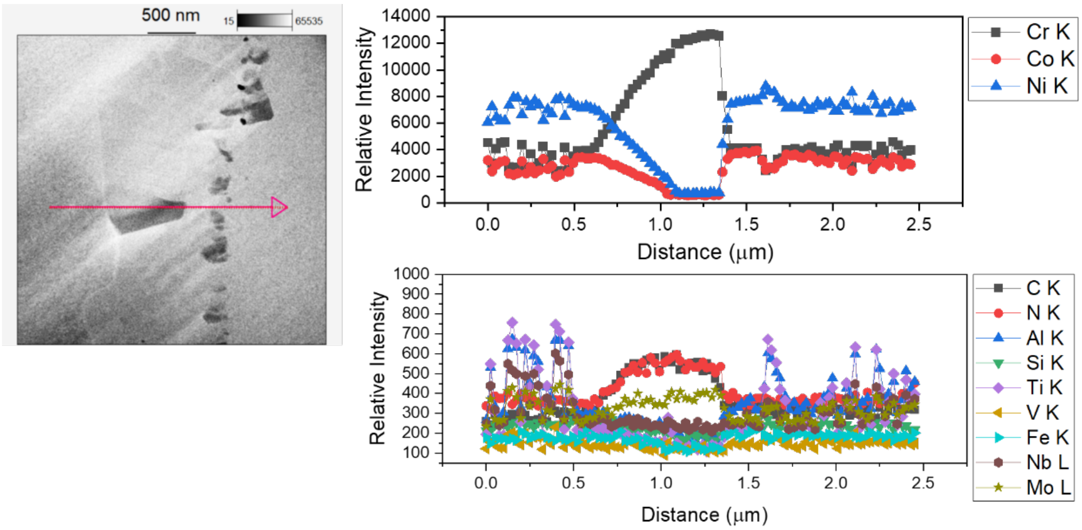

Figure A13: STEM-EDS line scan made across precipitate features in the second TEM sample from sample Row 14 Weld 25.

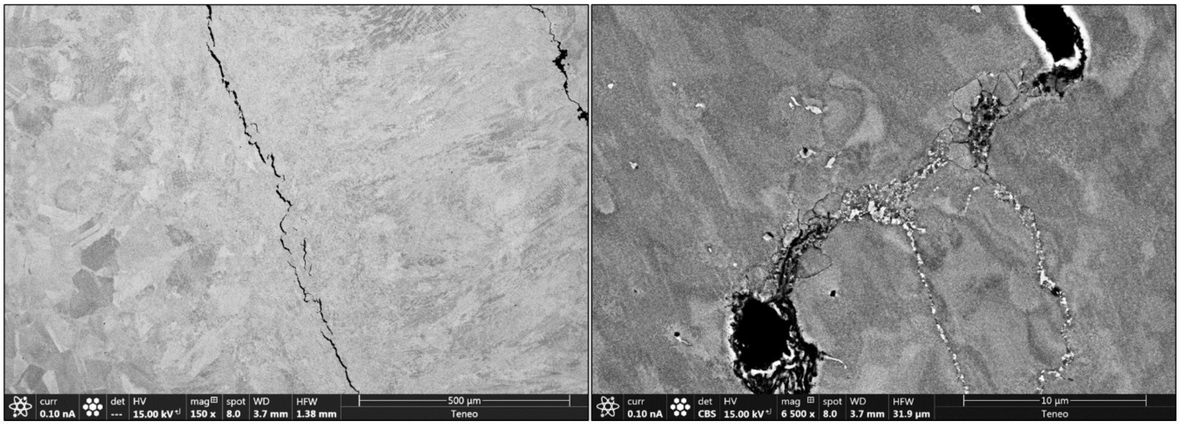

Figure A14: BSE images showing the cracks formed inside the weld metal regions of the sample section A5 in Demonstration Project #2 and the microstructural features formed ahead of the cracks.

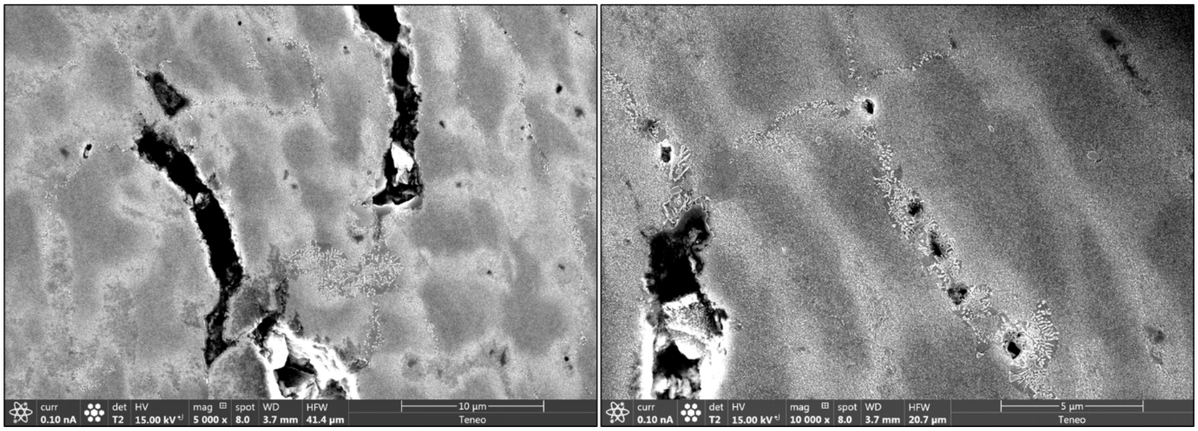

Figure A15: BSE images showing the cracks formed inside the weld metal regions of the sample section A5 in Demonstration Project #2 and the microstructural features formed ahead of the cracks.

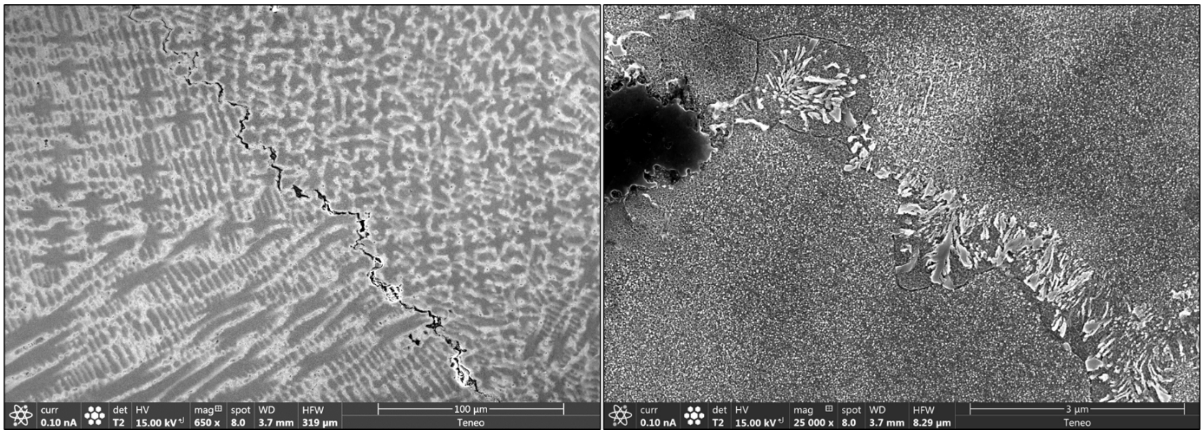

Figure A16: BSE images showing the cracks formed inside the weld metal regions of the sample section A5 in Demonstration Project #2 and the microstructural features formed ahead of the cracks.

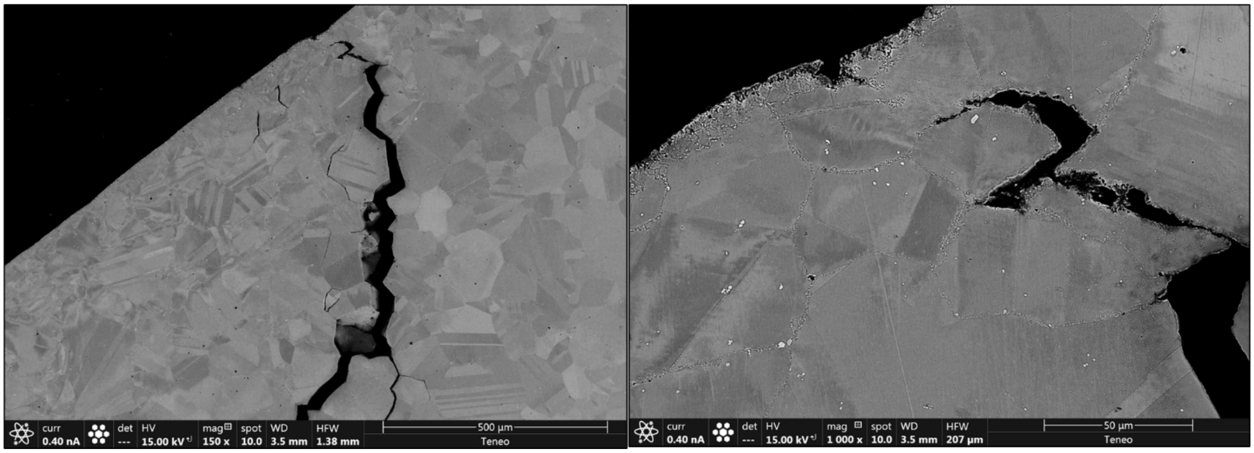

Figure A17: BSE images showing the cracks formed near the OD regions of the tube metal of the sample section A5 in Demonstration Project #2 and the microstructural features formed near the regions of the cracks.